Organic Thin-film Photovoltaics

Dissertation
zur Erlangung des Grades
‘Doktor der Naturwissenschaften’

am Fachbereich Chemie, Pharmazie und Geowissenschaften
der Johannes Gutenberg-Universität in Mainz

Miaoyin Liu

Geboren in Shandong Province / China
Mainz, 2010

Dedicated to my family

The impossible exists only until we find a way to make it possible.

Mike Horn

CONTENTS

Chapter 6 Experimental Part 145

Chapter 7 Conclusion and Outlook 165

Acknowledgement

List of Publications

Curriculum Vitae

Index of Abbreviations

AFM	Atomic force microscope
ASTM	American Society for Testing and Materials
BHJ	Bulk-heterojunction solar cells
CB	Conduction band
CV	Cyclic voltammetry
D/A	Donor/acceptor
DLCs	Discotic liquid crystals
DSSCs	Dye-sensitized solar cells
EA	Electron affinity
EPFL	École Polytechnique Fédérale de Lausanne
EQE	External quantum efficiency
FET	Field-effect transistor
FOC	Ferrocene/ferrocenium
FTO	Fluorine-doped tin oxide
HBC	Hexabenzocoronene
HOMO	Highest-occupied molecular orbital
HTM	Hole-transport material
IP	Ionization potential
IPCE	Incident-light-to-current conversion efficiency
IQE	Internal quantum efficiency
ITO	Indium tin oxide
LEDs	Light emitting diodes
LUMO	Lowest-unoccupied molecular orbital
MPIP	Max-Planck Institute for Polymer Research
MPP	Maximum Power Point
Mw	Weight average molecular weight
OPVs	Organic photovoltaics
P3HT	Poly(3-hexylthiophene)
[70]PCBM	[6,6]-phenyl C70-butyric acid methyl ester

PDI	Perylenediimide
PDI	Polydispersity index
PEDOT: PSS	Poly (3,4-ethylenedioxythiophene):polystyrenesulfonate
PPV	Poly (p-phenylene vinylene)
SEM	Scanning Electron Microscopy
SFM	Scanning force microscopy
Spiro-MeOTAD	2,2’,7,7’-tetrakis(N,N-di-p-methoxyphenylamine)-9,9’-spirobifluorene
STM	Scanning tunneling microscopy

Chapter 1 Motivation and Outline

With the increasing worldwide energy consumption, it is a hot topic that renewable energy sources should be explored and developed to replace the conventional energy sources which have a finite lifetime, such as oil and coal.[1,2] Renewable energy is generated from natural resources such as sunlight, wind, rain, tides, and geothermal heat, which neither run out of support nor have any significant harmful effects on our environment.[2] Among these renewable energy sources, the sunlight is remarkable in the sense that it could provide us the most considerable sum of energy: one hour's sunshine is already more than enough to satisfy worldwide energy needs for an entire year with the largest demand of human beings, which is 14 TW per year.[3]

Over the 20th century, human population quadrupled and energy consumption increase sixteenfold. It is estimated that there will be 8 to 10 billion people on Earth in 2050, with a 14 TW energy gap.[3] Obviously, solar sources will be the best way to offset the gap. As a kind of technology which can convert sunlight directly into electricity without emitting carbon dioxide and can thereby help to combat global warming, solar cells (also called photovoltaics) have gained broad interest both in the academic and the industrial community.[4-8]

1.1 Photovoltaic Effect

The photovoltaic effect was first recognized in 1839 by Becquerel when he shed light onto an AgCl electrode in an electrolyte solution and light-induced voltage was discovered.[9] After about half a century, Fritts created the first device made from Se wafers with around 1% of power conversion efficiency.[10] Since 1946 the modern junction semiconductor solar cells were patented by Ohl,[11] an intensive search for highly efficient photovoltaics has been processed. Especially, in 1954, Chapin, Fuller and Pearson in Bell Laboratories improved the efficiency of a Si cell to 6%.[12]

However, the large energy consumption in semiconductor processing technologies of the silicon-based solar cells, such as high temperature (400-1400°C), high vacuum conditions and numerous lithographic steps[13], is the main disadvantage for the development of inorganic solar cell. Therefore, the search for a new technology which utilizes cheap materials as well as fabrication methods to collect solar energy becomes more and more important. In 1986, the first organic thin-film solar cell with reasonable efficiency (up to 1%) was created and reported by Tang.[14] Since then, great interest has been devoted to the advantages of using organic materials in the solar cell field: various synthetic methods, plastic processing ability and low production cost. Compared to the inorganic solar cells, considerably less effort and production energy are consumed for organic semiconductors because of simpler processing at much lower temperatures (20-200°C).[15] The solar cell market is still dominated by inorganic solar cells which are approaching the theoretically limiting efficiency of 31% for a single cell.[16] Recently, scientists realized that the organic solar cell also have the potential to gain high power efficiency (theoretically as high as that in conventional inorganic semiconductor devices), organic solar cells are now leading the new approach that could result in the most significant cost reduction.[6] Furthermore, due to the advantages of organic compounds, organic solar cells have a broader application space, such as in the field of modern fashion, toys and mobile devices.[6]

1.2 Motivation

To gain high power conversion efficiency by using the organic solar cell technologies, the keystone is the investigation of new materials which could fulfil the multiple parameters for organic photovoltaic cells. Therefore, material scientists are still focused on searching new favorable organic compounds for solar cells. The research demonstrated in this thesis is the investigation of some new materials in the corresponding device architectures for a better understanding of the relationship between molecular structure and device performance. In this thesis, two kinds of materials with self-organization ability have been studied in the bulk-heterojunction solar cells: one series are discotic liquid crystals and the other series are polymers with ribbon structures. As organic sensitizers, a novel perylene dye and an isophorone dye were investigated in the solid-state dye-sensitized solar cells.

1.2.1 Self-organizable Donors for Bulk-heterojunction Solar Cells

In an organic material based solar cell, a photon from light can generate an exciton in an active layer which contains an electron acceptor and an electron donor material. Unlike inorganic solar cells, excitons in the organic solar cells can not be dissociated immediately, but will diffuse to the interface between the donor and the acceptor. Because of this aspect, the ideal structure of a bulk heterojunction solar cell (BHJ) (Figure 1) is the one where two phases of donor and acceptor are interspaced with a short average length scale of 10-20 nm equal to or less than the exciton diffusion length.[17] In this way, an efficient exciton diffusion for charge carrier generation at the donor/acceptor interface can be granted, and a feasible charge carrier transport can be ensured to the most extent. Unfortunately it is difficult to obtain such a well-organized nanostructure due to disorder. A key to nanoscale order is thought to be the self-organization of the photoactive materials.

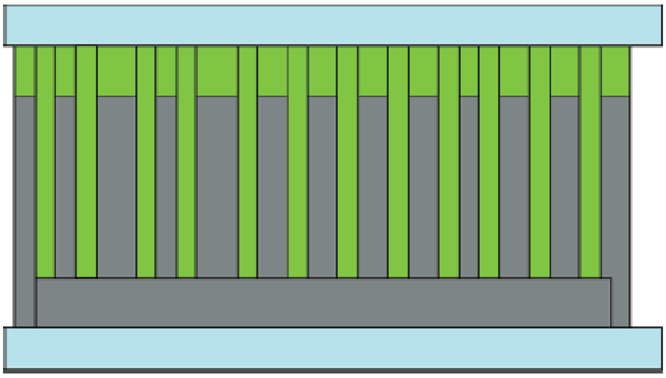

Figure 1. Ideal structure of a bulk-heterojunction solar cell.

1.2.1.1 Discotic Liquid Crystals as Donor Materials

Since discotic liquid crystals (DLCs) are structurally favorable organic charge transport materials due to their tendency to form columnar superstructures, they have been utilized in various electronic devices, such as LEDs,[18] solar cells[19] and FETs[20]. Single crystalline organic materials and doped organic polymers have presented their application in solar cells, however, with the drawback that single crystals are difficult and costly to process. This disadvantage could be overcome with the polymeric discotic liquid crystals because their long-range columnar structure facilitates the process of charge transport.

To investigate the relationship between the supramolecular organization of discotic liquid crystals and their photovoltaic performance, the study on the triangle-shaped discotic graphene molecules with swallow-tailed alkyl substituents was carried out in this thesis.

1.2.1.2 Conjugated Polymers for Polymer-Fullerene Solar Cells

Besides discotic liquid crystals, conjugated polymers have been used as key components for solar cells since 1990s. The conjugated polymers, consisting of chains and rings of carbon atoms in sp^1 and sp^2 hybridization, have a framework of alternating double- or triple- and single-bonds. Since the double bonds contain a σ-bond and a π-bond, and the π-electrons are delocalized over the entire molecule, the conjugated polymers can be regarded as quasi one-dimensional semiconductors.[21] The discovery in 1977 that doped polyacetylene could achieve metallic conductivity by the groups of Heeger, Shirakawa, and MacDiarmid spurred the interest in conjugated polymers as conducting materials. Unlike the case of an inorganic semiconductor in which a built-in field could be generated through the controlled placement of n- and p-tpye dopant atoms, it is difficult to controllably dope most conjugated polymers.[17] As a result of this, conjugated polymers are usually made as pure as is practically possible and can effectively be considered to be intrinsic semiconductors which can be applied in various kinds of semiconductor devices such as LEDs[22], solar cells, and FETs [23].

The conjugated polymer-fullerene bulk heterojunction is currently the best conjugated polymer-based PV cell. The prototypical bulk-heterojunction solar cells based on poly(3-hexylthiophene) (P3HT) and phenyl-C_{61}-butyric acid methyl ester (PCBM) can achieve efficiencies of 4-5%.[24,25] For the P3HT/PCBM system, the self-organization ability of the P3HT is believed to contribute greatly to the improved film morphology and consequently to the high conversion efficiency of such cell. With the consideration that the use of self-organizable polymers is a way to achieve efficient solar cells, a novel conjugated polymer with self-organization ability is described in Chapter 4.

1.2.2 Organic Sensitizers for Dye-sensitized Solar Cells

In the organic solar cell field, there is a special kind of solar cells, dye-sensitized solar cells (DSSCs), which simulate the light harvesting mechanism of plants and are based on inorganic semiconductor materials. Dye-sensitized solar cells were invented by Grätzel in 1991, therefore also named as Grätzel cells.[26] A common DSSC contains a liquid electrolyte to reduce oxidized dye. However, solvents in the electrolyte cause an instability problem because of their evaporation and leakage. Therefore, solid state dye-sensitized solar cells have received growing interest in recent years.[27-29] In these devices, a solid hole transport material has been used to replace liquid electrolyte, and the choice of the sensitizers is very critical.[30] Although ruthenium complexes still hold the record in the DSSCs, metal-free organic dyes have attracted increasing attention because of their low cost, environmentally benign character and generally higher molar absorption coefficients. As organic sensitizers, a novel perylene dye and an isophorone dye will be investigated respectively in the solid-state dye-sensitized solar cells in the sense that 1) they possess either good thermal stability or high absorption coefficient; 2) the absorptions of these two sensitizers complement each other, which makes it possible to build a molecular cocktail solar cell which can cover the whole region of visible light spectrum.

1.3 Outline

Chapter 2 gives an insight into organic thin-film photovoltaics and specified kinds of solar cells studied in this thesis: bulk-heterojunction solar cells and solid-state dye-sensitized solar cells. The basic operation mechanisms in each of these two device architectures are introduced. Regarding the materials investigated in this thesis, this chapter also includes a general introduction into liquid crystalline materials, conjugated polymers and organic sensitizers as well as their corresponding application in solar cells.

Chapter 3 deals with the application of triangle-shaped discotic graphenes for bulk-heterojunction solar cells. The discussion is focused on the relationship between their supramolecular organization and photovoltaic performance. The survey of thermotropic properties demonstrates that the related compounds' self-organization ability plays a significant role for high performance solar cells.

Chapter 4 includes the view how the self-organization ability of a polymer and film morphology influence the device performance. The devices fabricated from this alkyl-free benzo[2,1-b;4,5-b'] dithiophene containing polymer showed a significantly enhanced efficiency upon a short-term annealing, due to the strong self-organization ability of the polymer. The curvature of the monomer unit guarantees an optimum compromise between solubility and aggregation tendency to a quick formation of phase separation from fullerene compounds in the blend. The processing additives such as 1,8-octanedithiol gave an additional driving force for better formation of bicontinuous pathways and further improved the power conversion efficiency.

Chapter 5 concerns the study on two novel metal-free sensitizers for solid-state dye-sensitized solar cells. One organic sensitizer is perylene monoimide with an absorption maximum of 566 nm on the dye-loaded TiO_2 film, which shows an outstanding thermo-, photo-, and chemical stability. The other one is isophorone dye with λ_{max} of 447 nm on the semiconductor surface. The power efficiency of perylene and isophorone dye based solid-state solar cells was 2.2 and 1.9%, respectively. The complementarity of the absorption of these two sensitizers creates an opportunity to build a solar cell with co-sensitizers which can absorb the whole region of visible light.

Chapter 6 is the experimental part, which includes the device preparation methods and solar cell testing facilities, as well as utilized techniques for investigating materials and morphology.

As the conclusion, an overall evaluation on the study carried out in this thesis is presented in Chapter 7. What also included in this part are some suggestions on the molecular design and device architecture for future research.

1.4 References

[1] http://www.meto.gov.uk/climatechange/guide/quick/evidence.html

[2] http://en.wikipedia.org/wiki/Renewable energy

[3] N. Norbrook, G. Mithembu-Salter, *Africa Report*, **2007**, *7*.

[4] D. Y. Goswami, *Advances in Solar Energy: An Annual Review of Research and Development*, **2003**, *7*.

[5] C. Brabec, U. Scherf, V. Dyakonov, Eds., *Organic Photovoltaics: Materials, Device Physics, and Manufacturing Technologies*; Wiley-Vch, **2008**.

[6] V. Petrova-Koch, R. Hezel, A. Goetzberger, Eds., *High-Efficient Low-Cost Photovoltaics; Springer Series in Optical Sciences*, **2009**.

[7] S.-S. Sun, N. S. Sariciftci, Eds., *Organic Photovoltaics: Mechanisms, Materials, and Devices*; Marcel Dekker Inc, **2005**.

[8] A. Smee, *Elements of Electro-Biology London: Longman, Brown, Green, and Longmans.* **1849**.

[9] A. E. Becquerel, *Comptes Rendus* **1839**, *9*, 561 (in French).

[10] http://en.wikipedia.org/wiki/Charles_Fritts.

[11] R. S. Ohl, L. Silver, **1946**, U.S. Patent 2402662.

[12] D. M. Chapin, C. S. Fuller; G. L. Pearson, J. *Appl. Phys.* **1954**, *25*, 676.

[13] H. J. Lewerenz, H. Jungblut, Photovoltaic - Grundlagen und Anwendungen, *Springer*, **1995**.

[14] C. W. Tang, *Appl. Phys. Lett.* **1986**, *48*, 183.

[15] K. Petritsch, *Organic solar cell architectures*, Cambridge and Graz, **2000**.

[16] M. A. Green, *Physica E*, **2002**, *14*, 65.

[17] K. M. Coakley, M. D. McGehee, *Chem. Mater.* **2004**, *16*, 4533.

[18] T. Christ, B. Glüsen, A. J. Greiner, A. Kettner, R. Sander, V. Stümpflen, V. Tsukruk, J. H. Wendorff, *Adv. Mater.* **1997**, *9*, 48.

[19] L. Schmidt-Mende, A. Fechtenkötter, K. Müllen, E. Moons, R. H. Friend, J. D. MacKenzie, *Science,* **2001**, *293*, 1119.

[20] A. M. van de Craats, N. Stutzmann, O. Bunk, M. M. Nielsen, M. Watson, K. Müllen, H. D. Chanzy, H. Sirringhaus, R. H. Friend, *Adv. Mater.* **2003**, *15*, 495.

[21] T. Kietzke, *Advances in OptoElectronics*, **2007**, *Volume 2007*, Article ID 40285.

[22] J. H. Burroughes, D. D. C. Bradley, A. R. Brown, R. N. Marks, K. Mackay, R. H. Friend, P. L. Burns, A. B. Holmes, *Nature*, **1990**, *347*, 539.

[23] M. Zhang, H. N. Tsao, W. Pisula, C. Yang, A. K. Mishra, K. Müllen, *J. Am. Chem. Soc.*, **2007**, *129*, 3472.

[24] M. Reyes-Reyes, K. Kim, D. L. Carroll, *Appl. Phys. Lett.* **2005**, *87*, 083506.

[25] G. Li, V. Shrotriya, J. Huang, Y. Yao, T. Moriarty, K. Emery, Y. Yang, *Nat. Mater.* **2005**, *4*, 864.

[26] B. O'Regan, M.Grätzel, *Nature* **1991**, *353*, 737.

[27] U. Bach, D. Lupo, P. Comte, J. E. Moser, F. Weissortel, J. Salbeck, H. Spreitzer, M. Grätzel, *Nature,* **1998**, *395*, 583.

[28] L. Schmidt-Mende, U. Bach, R. Humphry-Baker, T. Horiuchi, H. Miura, S. Ito, S. Uchida, M. Grätzel, *Adv. Mater.* **2005**, *17*, 813.

[29] H. J. Snaith, A. J. Moule, C. Klein, K. Meerholz, R. H. Friend, M. Grätzel, *Nano Lett.* **2007**, *7*, 3372.

[30] L. Schmidt-Mende, J. E. Kroeze, J. R. Durrant, M. K. Nazeeruddin, M. Grätzel**,** *Nano Lett.* **2005**, *5*, 1315**.**

Chapter 2 Introduction to Organic Thin-film Photovoltaics

Organic photovoltaics (OPVs), when classified by device structures, could be separated into three main kinds: multilayer-junction[1], bulk-heterojunction[2] and dye-sensitized solar cells[3,4]; while by the types of the applied materials in the devices, could be divided into main types: small molecule[5], polymer[6] and hybrid solar cells[7]. Based on the structure and property of the compounds investigated, two kinds of device architectures were involved in this thesis: bulk-heterojunction solar cells and solid-state dye-sensitized solar cells. This chapter describes these two device architectures as well as the basic photovoltaic parameters.

2.1 Photovoltaic Parameters

2.1.1 External Quantum Efficiency (EQE)

The photocurrent action spectrum represents the ratio of the observed photocurrent divided by the incident photon flux as a function of the excitation wavelength, the so-called incident photon to current conversion efficiency (IPCE), also named as external quantum efficiency (EQE).

$$\text{IPCE}(\lambda) = \text{EQE}(\lambda) = \frac{n_{electrons}}{n_{photons}} = \frac{I/e}{P/h\nu} = \frac{I}{P}\times\frac{hc}{e\lambda} = \frac{I}{P}\times\frac{1240}{\lambda(nm)}$$

where I is photocurrent in A/m^2 and P is incident light power in W/m^2.

EQE is measured by recording the photocurrent response while continuously varying the wavelength of the incident light and can determine the efficiency of conversion of photons to electrons. The maximum EQE is named EQE_{max}, which is a key parameter for describing the device. The higher the EQE_{max}, the more efficient the device is. A typical example of a photoaction spectrum is shown in Figure 1.

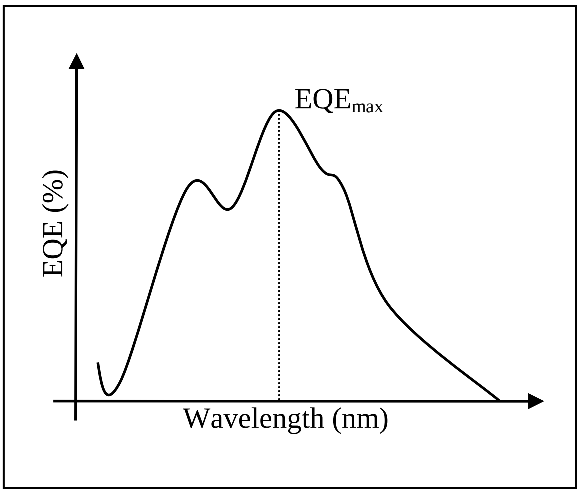

Figure 1. EQE-λ curve measured at monochromatic incident light.

a) In organic bulk-heterojunction solar cells, the internal quantum efficiency (IQE), is the product of four efficiencies in each corresponding charge generation step:

$$\eta_{IQE} = \eta_A \eta_{ED} \eta_{CT} \eta_{CC}$$

where η_A is the absorption efficiency of light within the active region of the solar cell; η_{ED} is the exciton diffusion efficiency to a dissociation site; η_{CT} is the charge transfer efficiency; which is the efficiency for dissociation of an exciton into a free electron and hole pair at that site; η_{CC} is the charge collection efficiency. Taking into consideration the optical losses occurring on coupling light in the device active region, the external quantum efficiency (EQE) is:

$$\eta_{EQE} = (1-R)\,\eta_{IQE}$$

where R is the reflectivity of the substrate-air interface.

b) In dye-sensitized solar cells (DSSCs), the item of IPCE is often used, instead of the term of EQE. In DSSCs, IPCE or EQE, is expressed as a product of three factors:

$$\mathrm{IPCE}(\lambda) = \mathrm{EQE}(\lambda) = \mathrm{LHE}(\lambda)\ \Phi_{inj}\ \Phi_{col}$$

where LHE(λ) is the light-harvesting efficiency of the sensitizer, Φ_{inj} is the charge injection efficiency of the dye into the semiconductor, and Φ_{col} is the charge collection efficiency at the external electrodes.

2.1.2 I-V Curve

The photocurrent action spectrum inspects the photon to electron transfer capability of solar cells. However, to decide whether a solar cell device can be commercialized or not, the most efficient method is to measure the photocurrent and photovoltage under simulated AM 1.5 solar light. A typical solar cell *I-V* curve is exhibited in Figure 2.

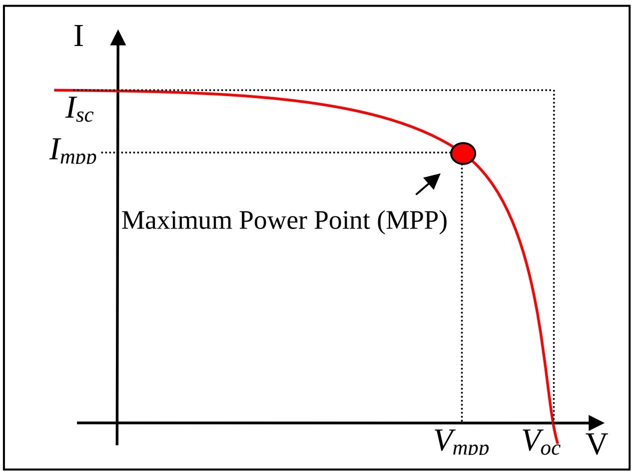

Figure 2. Typical I-V curve of solar cells.

The overall power conversion efficiency, η, is calculated according to the following equation:

$$\eta = \frac{P_{out}}{P_{in}} = FF\frac{V_{oc}I_{sc}}{P_{in}}$$

where P_{out} is the maximum output electrical power (in W/m^2) of the device under illumination, P_{in} (in W/m^2) is the light intensity incident on the device, V_{oc} is the open circuit voltage, and I_{sc} is the short-circuit current in A/m^2.

The parameter FF is known as the fill factor, which is defined as:

$$FF = \frac{V_{mpp}I_{mpp}}{V_{oc}I_{sc}}$$

where V_{mpp} and I_{mpp} are the voltage and current at the maximum power point in the *I*-*V* curve, respectively.

The maximum rectangular area (V_{mpp} × I_{mpp}) under the I-V curve corresponds to the maximal output power of the device. An ideal device would have a rectangular shaped I-V curve and therefore a fill factor FF = 1. The overall efficiency is an important parameter to evaluate the performance of the device, and is the default efficiency value mentioned in the literature.

2.2 Bulk-heterojunction Solar Cells (BHJ)

2.2.1 Concept

In a BHJ cell, the active layer consists of two components forming disordered, mutually penetrating networks of the donor (a *p*-type semiconductor, such as a conjugated polymer) and acceptor (an *n*-type semiconductor, such as a fullerene derivative) phase. In such a bulk heterojunction, the interface is not planar but spatially distributed over the entire volume of the active layer. The concept of BHJ solar cell is to overcome the shortcoming presented in the bilayer heterojunction structure. In the latter type, the limited interfacial area between donor and acceptor results in the low photocurrent, since the layer thickness normally is larger than the exciton diffusion length of 1-15 nm such that only excitons close to the interlayer barrier can be used for charge generation.

A typical bulk-heterojunction solar cell contains ITO coated glass substrate, which is covered by a transparent, conductive polymer, poly(3,4-ethylenedioxythiophene):polystyrenesulfonate (PEDOT: PSS).[8,9] The mixture of conjugated polymer with fullerene can be printed on the top of PEDOT:PSS. By vacuum deposition, a silver or aluminum film as counter electrode covers the active layer (Figure 3).

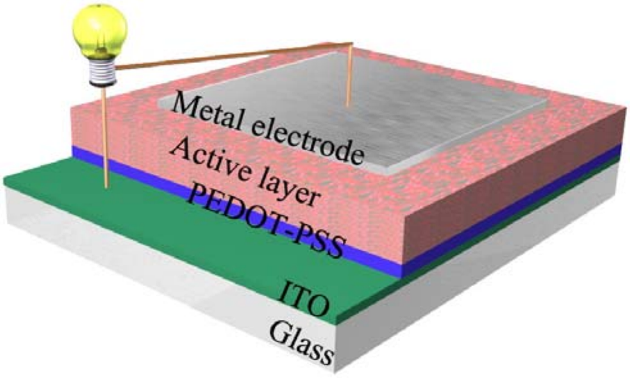

Figure 3. Bulk-heterojunction architecture in polymer solar cells

In the BHJs, the absorption of light leads to strongly bound electron and hole pair, the excitons, in the photoactive materials. The excitons can travel only short distances (typically 1-15 nm)[10-14] by diffusion before they recombine. Alternatively, if an acceptor material (e.g., a fullerene derivative) is within this range, that is to say, if the length scale of the blend is similar to the exciton diffusion length, in the proximity of every generated exciton there is an interface with an acceptor where fast dissociation takes places. Then the exciton can dissociate into free charges. The free charge carriers will move to the corresponding electrodes by following the continuous route of donors or acceptors, provided that continuous pathways exist in each material from the interface to the respective electrodes. The electrons reach the metal electrode and transfer to the electrical load and then transmit to ITO layer (Figure 4). Obviously, if the network in the active layers is bicontinuous,[15] the charge collection efficiency can be quite high. For that reason, the donor and acceptor materials generally should have self-assembling ability to form phase separation, which enhance the continuous path construction for the electron/hole collection to the respective electrodes.

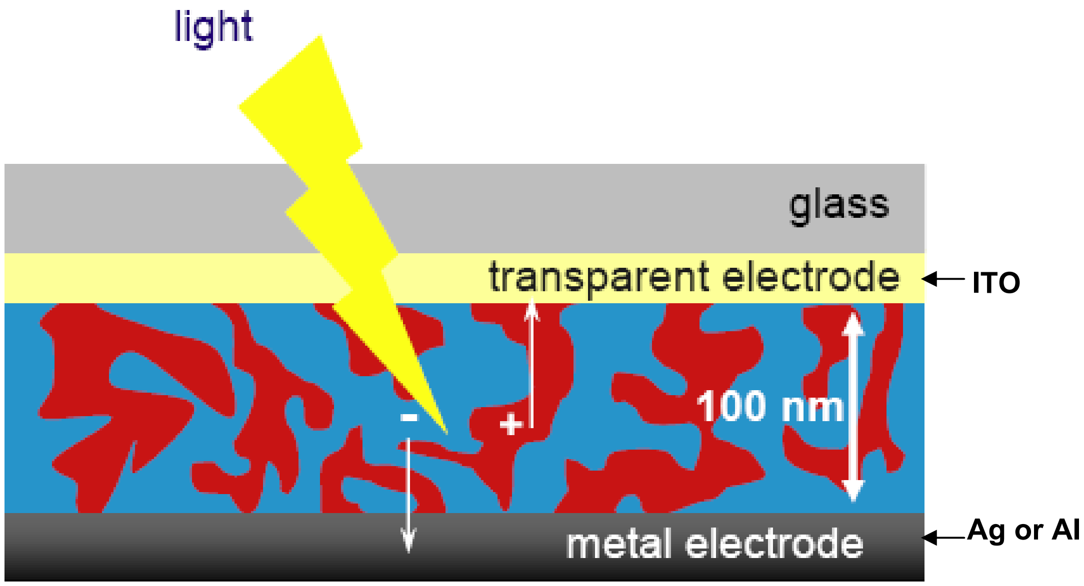

Figure 4. Nanoscopic mixing of donor and acceptor in a bulk-heterojunction solar cell (copied from Rene Janssen, DPI annual meeting)

2.2.2 Fundamental Physical Processes

In a bulk heterojunction solar cell, there are the five fundamental physical processes:

Creation of excitons,

Diffusion of excitons,

Dissocation of charge carriers at the donor/acceptor interface,

Charge transport, and

Extraction of the charge carriers at the electrodes,

which will be discussed in the following sections.

2.2.2.1 Creation of Excitons

Since solar irradiation reaching the earth's surface varies greatly with a lot of factors, the photovoltaic industry, in conjunction with the American Society for Testing and Materials (ASTM) and government research and development laboratories, has developed and defined a standard terrestrial solar spectral irradiance distribution "AM1.5G" for theoretical evaluation of the solar irradiation effects and for simulator design. In the AM 1.5 spectra (Figure 5), solar radiation covers a wide range of wavelengths, with the maximum irradiation at 480 nm and 70% of the photons located in the range of 400-920 nm.

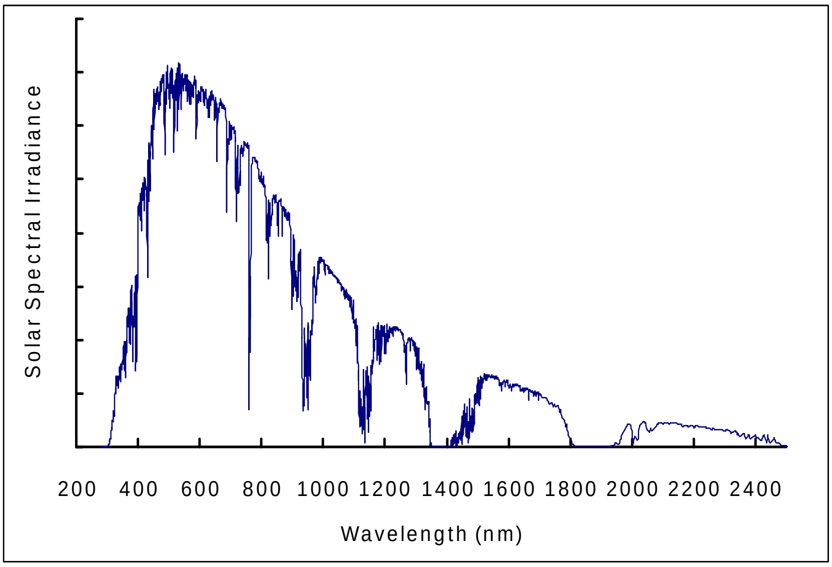

Figure 5. The standard AM 1.5G solar spectrum.

The first prerequisite for an efficient solar cell is the capture of a large fraction of the incoming sun light by the active layer. Most solution processable semiconducting polymers have bandgaps larger than 1.9 eV, indicating that only 30% of the solar photon flux is covered (assuming complete absorption of the solar emission intensity by the material).

Additionally, because most polymers have low charge-carrier mobility, the thickness of the active layer is limited to about 100 nm, which in turn leads to the absorption of only about 60 % of the incident light at the absorption maximum (without considering the loss from the back reflection of the electrode).[16] So, the organic materials with expanded absorption spectra up to 700-800 nm and high charge-carrier mobility are favorable for efficient solar cells.

Upon light absorption in organic materials, the exciton, a Coulomb-correlated electron-hole pair, is generated. When a photon enters a semiconductor, an electron is excited from the valence band into the conduction band. The missing electron in the valence band leaves a hole (of opposite electric charge) behind, to which the electron is attracted by the Coulomb force.[17]

2.2.2.2 Diffusion of Excitons

After the excitons are generated, they need to firstly dissociate to the donor/acceptor interface for the charge separation. Since the exciton dissociation process is confined to the D/A interfacial area, only excitons produced at a distance shorter than their diffusion length have the good possibility to reach the D/A interface where charge carriers are formed. Hence, for polymer-based solar cells, the exciton diffusion length L_D is an important parameter because the exciton diffusion process masters the photoexcitation energy transfer to the D/A interface. Consequently, the maximum thickness of the active layer is limited by the exciton diffusion length, and thus the maximum fraction of the incident light that the cell can absorb is also restricted.

The exciton diffusion length L_D is defined as

$$L_D = \sqrt{D\tau_0}$$

where D is the diffusion constant and τ_0 is the decay time constant. So far two methods have been usually applied to estimate the exciton diffusion length L_D for organic materials. One method is to measure the photoluminescence (PL) quenching in well-defined heterostructures,[18-21] the other is to fit photocurrent spectra with respect to incident wavelength or varying organic layer thickness by utilizing specific models to deduce L_D values.[11, 22-24] The exciton diffusion lengths in various conjugated polymers reported in the literature differ very much, ranging from 5 to 20 nm. [20, 24-26] For example, by measuring the photoluminescence quenching in well-defined heterostructures comprising a self-assembled fullerene monolayer and a thin spin-coated polymer layer of variable thickness, the exciton diffusion length in ladder-type poly (p-phenylene) was inferred to be 14 nm.[20] From the PL quenching of heterojunctions consisting of polythiophene and evaporated C60, an exciton diffusion length of 5 nm was obtained. [21] By measuring the photocurrent, an exciton diffusion length of 7-8 nm was decided for a precursor poly (*p*-phenylene vinylene) (PPV) based on the photovoltaic devices combing C60 and this precursor PPV.[11]

2.2.2.3 Dissociation of Charge Carriers at the Donor/Acceptor Interface

The key process after the exciton diffusion is then the dissociation of photogenerated electron-hole pairs (excitons) into charge carriers.

2.2.2.3.1 Photoinduced Charge Separation Process

One of the main differences between inorganic and organic semiconductors is the magnitude of the exciton binding energy, i.e. the strength of the Coulomb attraction between the electron and hole. In many inorganic semiconductors, the binding energy is smaller than the thermal energy (*kT*) at room temperature and therefore free charges are created under ambient conditions upon excitation,[27] whereas the exciton binding energy in an organic semiconductor exceeds *kT* and consequently the excitons are formed upon excitation instead of free charges.[28]

The method to dissociate bound electron-hole pairs in organic semiconductors then is the so-called donor/acceptor interface. Once an exciton reaches the D/A interface, the electron promoted into the LUMO level of the excited donor can be transferred to the lower-lying LUMO level of the acceptor. If the hole then remains on the HOMO level of the donor, light is converted by this photoinduced electron-transfer process into electrical charges. [29]

This photoinduced charge separation process is also called 'photo-doping', since it is a photoinduced (in contrast to chemical or thermal induced) redox reaction between the donor and acceptor. In an organic bulk-heterojunction solar cell, the photons are absorbed by the donor or the acceptor, or by both. If the donor absorbs most of the incident light, the excitons are generated on the donor moieties. The process of photoexcitation, exciton decay, charge separation and recombination is shown in Scheme 1 and explained step by step as follows:

1. Photoexcitation at donor:

   $D/A + h\nu \rightarrow D^* /A$

   where D* is a donor exciton, *hv* is the absorbed photon energy and can be estimated from absorption or excitation spectra.

2. Donor exciton decay to its ground state:

   $D^* /A \rightarrow D/A + h\nu$

   where *hv* is the emitted photon energy and can be estimated from emission spectra.

3. Charge separation or electron transfer from donor LUMO to acceptor LUMO:

$D^* /A \rightarrow D^+A^-$

4. Charge recombination or electron back transfer from acceptor LUMO to donor HOMO:

$D^+A^- \rightarrow D/A.$

Similarly, if the acceptor absorbs most of the incident light, the excitons are generated on the acceptor moieties. The corresponding process is shown as followed:

5. Photoexcitation at acceptor:

$D/A + hv \rightarrow D /A^*$,

where A^* is an acceptor exciton.

6. Acceptor exciton decay to its ground state:

$D /A^* \rightarrow D/A + hv$

7. Charge separation or electron transfer from donor HOMO to acceptor HOMO:

$D /A^* \rightarrow D^+A^-$.

8. Charge recombination, same as in process 4.

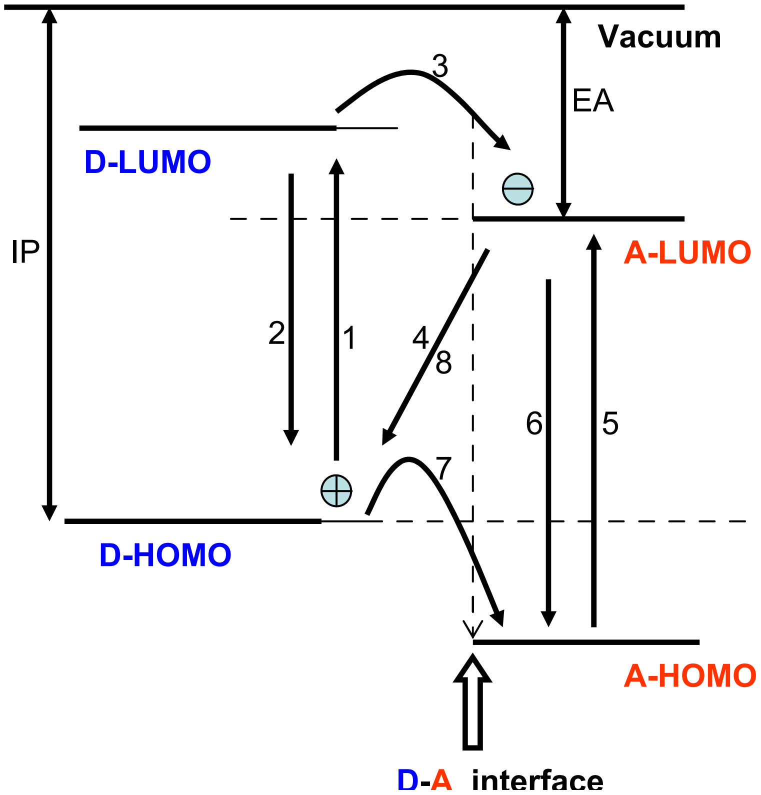

Scheme 1. Photoinduced charge separation and recombination processes in an organic D/A light harvesting system. EA is electron affinity, and IP is ionization potential.

In organic solar cells, charge separation (steps 3 and 7) competes with exciton decay (steps 2 and 6). Exciton quenching parameter (Y_{eq}), defined as the ratio of charge separation rate constant versus exciton decay rate constant, designates the exciton-charge conversion efficiency:

$Y_{eqD} = k_{sD}/ k_{dD}$ for donors,

$Y_{eqA} = k_{sA}/ k_{dA}$ for acceptors,

In the bulk-heterojunction solar cells, the charge separation (steps 3 and 7) competes also with charge recombination (steps 4 and 8). The recombination quenching parameter (Y_{rq}), defined as the ratio of charge separation rate constant versus charge recombination rate constant, is also a critical factor for light harvesting system.

$Y_{rqD} = k_{sD} / k_r$ for donors,

$Y_{rqA} = k_{sA} / k_r$ for acceptors,

It is clear that it is favorable that in efficient solar cell devices both Y_{eq} and Y_{rq} should be large.

2.2.2.3.2 Loss Mechanisms

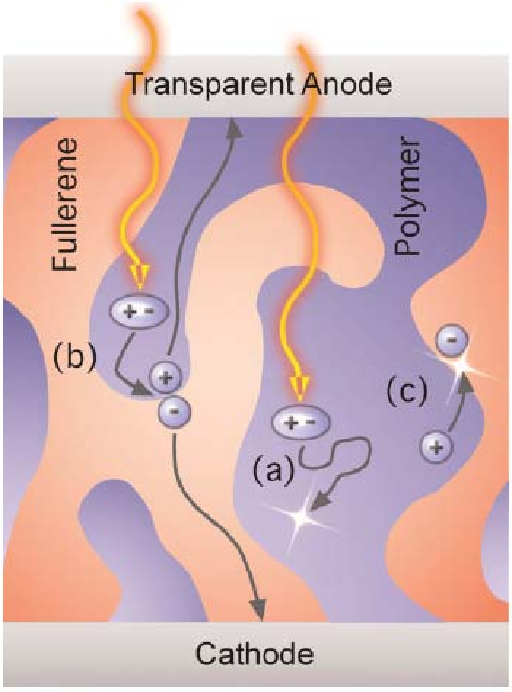

Figure 6. The steps from light absorption to the flow of photocurrent in a polymer solar cell, and some loss mechanisms: (a) photoluminescence due to excitons not reaching the donor–acceptor interface during their lifetime; (b) polaron pair dissociation or geminate recombination of bound electron-hole pairs, respectively; and (c) bimolecular recombination of free charge carriers.[30]

Figure 6 demonstrates the loss mechanisms from the step of light absorption to the flowing photocurrent.[30] Upon light absorption, the excitons are generated. The excitons decay either radiatively (leading to photoluminescence) or nonradiatively through geminate recombination. If the excitons do not reach a D/A interface within their lifetime, they will recombine radiatively (a), sending out photoluminescence. When the excitons reach the D/A interface, an electron transfer to the acceptor molecular yields a polaron pair (b) where the geminate recombination could also happen. (Note: polaron pairs are the intermediate step from an exciton to a pair of free polarons.) It should be noted that, under light illumination, some percentage of absorbed photons creates excitons, while the remaining percentage create spatially-indirect excitons, also referred to as neutral bipolarons (polaron pairs bound by Coulomb attraction). The geminate recombination of the neutral bipolarons is predominantly nonradiative. On the way of the separated charge carriers to their respective electrodes, charges can be trapped, or bimolecular recombination (c) can take place. [30]

2.2.2.3.3 Marcus Theory

When the exciton diffuses towards the D/A interface, it is energetically favorable if the electron is transferred to the acceptor molecule. From classical Marcus electron transfer theory,[31] the electron transfer rate constants can be defined as:

$$K_{ET} = A \exp[- (\lambda_c + \Delta L)^2 / 4\lambda_c K_b T]$$

where λ_c is the reorganization energy which contains contributions from molecular motions, vibrations, solvent effects, etc., and can be estimated from molecular vibrational spectroscopy or from excitation-emission spectroscopy under certain conditions. k_b is the Boltzman constant and T is the temperature. ΔL is the LUMO offset between donor and acceptor, providing the driving force for charge separation.

As the value of V_{OC} is governed by the energetics of the LUMO of the acceptor and the HOMO of the donor, i.e., Δφ ($HOMO_D$-$LUMO_A$) (Figure 7), a higher V_{OC} can be achieved by fine tuning the energy levels, such as increasing the $LUMO_A$ or decreasing the $HOMO_D$. However, the increasing of $LUMO_A$ will reduce K_{ET} and the decreasing of $HOMO_D$ will increase the bandgap of donor material and consequently reduce the light absorption. Hence, a tradeoff between a sufficient electron transfer driving force and a large V_{OC} origin should be carefully controlled for obtaining an efficient solar cell.

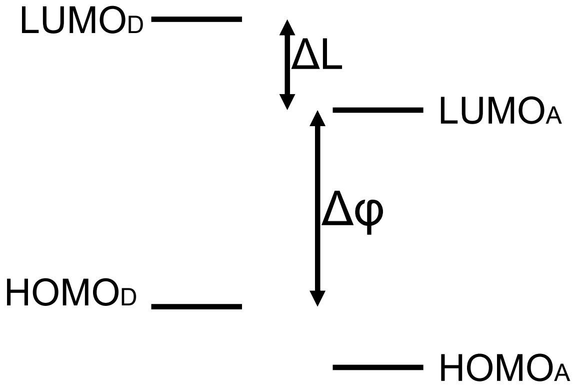

Figure 7.Energy diagram of a donor/acceptor pair.

2.2.2.4 Charge Transport

After photoinduced electron transfer at the D/A interface and subsequent dissociation, the electrons are localized in the acceptor phase whereas the holes remain in the donor phase. Then, the free charge carriers must be transported via percolated pathways towards the electrodes to produce the photocurrent. If donor and acceptor phases are perfectly ‘bicontinuous’ between the two electrodes, and all LUMO and HOMO orbitals are nicely matched, the carriers would be able to diffuse smoothly towards their respective electrodes.

Except for the influence of phase separation and pathways properties, the instinct characteristics of charge carriers, i.e., charge carrier mobility μ, also plays a critical role in determining the fluency and efficiency of charge transport in the device. Charge carrier mobility μ can be determined by three methods. By using pulse radiolysis time-resolved microwave conductivity (PR-TRMC) method it is possible to determine the charge carrier mobility on a nanometer length scale (interface effects caused by electrodes are avoided and electric field effects are minimized, so traps caused by structural defects and impurities are far less disruptive). It is very important to emphasize that the charge carrier mobility determined by this technique provides different information from techniques such as time-of-flight (TOF) or field-effect transistor (FET) experiments. The PR-TRMC technique reveals the intrinsic or local mobility of charge carriers which migrate between several molecules, whereas the mobility in the bulk, which are obtained by the TOF and FET experiments, is usually lower due to a higher degree of disorder and possible trapping sites at grain boundaries. The values obtained through the latter approaches are strongly dependent also on the long-range order of the sample, which can be affected by different processing techniques. The charge carrier mobility revealed by the PR-TRMC technique can be considered as the maximum possible values.[32]

2.2.2.5 Extraction of the Charge Carriers at the Electrodes

In order to extract the photogenerated charge carriers via drift selectively to the respective electrodes, an energetically asymmetric structure is essential for an efficient solar cell. The difference of the electron affinities of the two electrodes induces a built-in electrical field, which causes a preferred direction for the charge transfer.[33]

As transparent electrode, a layer of indium tin oxide (ITO) is used, and the selectivity of this electrode is usually enhanced by depositing a PEDOT:

PSS (poly(3,4-ethylendioxythiophene)-polystyrene-para-sulfonic acid)(Figure 8) layer on top. This PEDOT:PSS layer improves the surface quality of the ITO electrode (reducing the probability of shorts) as well as facilitates the hole injection/extraction.[49a] PEDOT: PSS is generally applied as a dispersion of gelled particles in water. The highly conductive PEDOT:PSS layer can be obtained by spreading the dispersion on the ITO surface usually by spin-coating and driving out the water by heat.

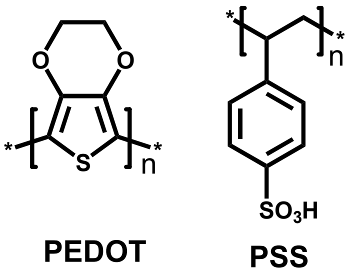

Figure 8. Chemical structure of PEDOT:PSS.

It is believed that for the efficient carrier collection at the electrodes, it is preferable when the acceptor LUMO level is close to the Fermi level of the small work function electrode (metals, such as aluminum) and the donor HOMO level is close to the Fermi level of the large work function electrode. [29]

2.2.3 Molecular and Morphology Requirements for the Photoactive Layer

The efficiency of a bulk-heterojunction solar cell is highly dependent on the nanoscale morphology of donors and acceptors in the photoactive layer. The limited exciton diffusion length in organic semiconductors requires finely phase separated D/A blend. And an effective charge transport also relies on a bicontinuous interpenetrating phase structures.

Table 1 summarizes some morphological requirements for the photoactive layer. For efficient utilizations of incident light, the absorption spectrum of donor materials should better fit the solar spectrum, which indicates lower bandgap polymers can capture more near-infrared (NIR) photons. To absorb as much light as possible, the photoactive layer should be thick enough, i.e. hundreds of nanometers; and inside these layers controlled nanoscale D/A phase separation should be presented to ensure efficient exciton dissociation. For the active layer forming, both thermodynamic and kinetic approaches could be applied to optimize the film morphology. For example, thermodynamically, the ratio between D/A and their solubility influence the morphology of the active layer greatly; kinetically, the method of spin-coating is preferable for forming more homogeneous morphology than the method of film casting does.

Table 1. Molecular and morphology requirements for the photoactive layer of an efficient polymer solar cell

Requirements	**Influenced by**	
	Molecular architecture	**Morphology**
Light absorption	Molecule design to tune bandgap	Film thickness and roughness
Exciton dissociation	Energy match between D/A	a) Large interfacial area b) Small acceptor-donor phases within exciton diffusion length
Charge transport	Molecule with high charge carrier mobility	a) Short and continuous pathways to the electrodes b) Ordered (crystalline) transportation pathways
Processability	Stereoregularity, molecular weight, side chain to improve solubility	Film formation and phase separation

Generally, by choosing appropriate solvents (or mixed solvents), optimized compound composition and correct preparation conditions (such as appropriate spin-coating speed, morphology control via annealing[41]), nanoscale phase separation between D/A constituents can be achieved, and continuous pathways for charge carriers to the electrodes can be provided.

As indicated in Table 1, both molecular design and morphology control should be considered thoroughly to achieve new promising donor materials for the application in bulk-heterojunction solar cells. As a good combination of these two aspects, in this thesis, two series of materials, discotic liquid crystals and self-organizable conjugated polymers, are studied. Below follow some general introductions into these two series of molecules and their application in BHJs.

2.2.3.1 Discotic Liquid Crystals

The discovery of discotic liquid crystals (DLCs) was firstly reported by Chandrasekhar *et al*. in 1977.[34] This is a kind of molecules with a flat, rigid aromatic cores surrounded by flexible chains. They generally have up to six-fold rotational symmetry and three or more peripheral chains.

Typical mesophases formed by disk-like molecules are columnar, wherein the molecules are "stacked" into columns. The main driving force for the columnar self-assembly is the π-π interaction between the aromatic cores.

Discotic liquid crystalline porphyrin complexes were firstly studied by Gregg *et al.* in the aspect of photovoltaic effects.[35] A major breakthrough of using the self-organization ability of discotic liquid crystals in solar cells was reported by Schmidt-Mende *et al*. utilizing a hexabenzocoronene derivative (HBC) as the hole-transporting layer and a perylenediimide as the electron-transporting material to construct a solar cell.[36] The HBC has the highest hole mobility ever reported for a discotic liquid crystal and is unusually stable and remains discotic well below room temperature.[37] The device showed high external quantum efficiency (EQE) of 34% at 490 nm, corresponding to an overall efficiency of 1.95 %. The remarkable result was believed to be coming from the vertical segregation of D/A layers and sufficient interpenetration between D/A. This was regarded as the first step in the direction that combination of molecular design with mesoscopic self-organization could lead to simple routes to efficient and durable organic solar cells. Later on, studies on the photovoltaic performance of this kind of discotic materials have been carried out in our group.[38] In this thesis, a novel series of triangle-shaped discotic graphenes with swallow-tailed alkyl substituents have been investigated regarding the relationship between the supermolecular order and photovoltaic performance.

2.2.3.2 Conjugated Polymers

To date, the best BHJs are fabricated from the conjugated polymer-fullerene blend. The combination of conjugated polymer and fullerene in bulk heterojunction can be dated back to the discovery that the transfer of photoexcited electrons from conjugated polymers to fullerenes is very efficient.[30] Fullerenes (Figure 9) have been found to out-perform all the other electron-accepting materials in photovoltaic devices due to their high electron affinity and superior ability to transport charge.[39] Thus, the attention of the scientists has been drawn mostly to the exploration of new polymers.

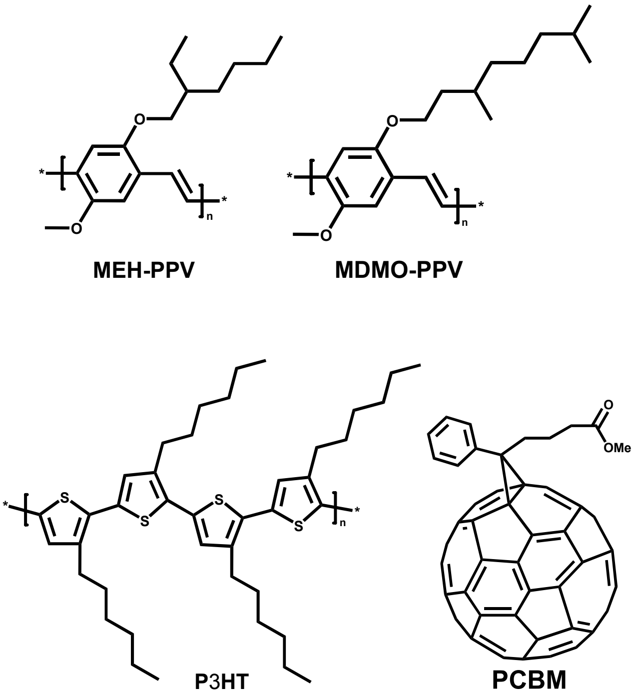

Figure 9. Chemical structures of some commonly used conjugated polymers and acceptor material (PCBM) in organic solar cells

Figure 9 demonstrates the chemical structures of some commonly used conjugated polymers in organic solar cells. Table 2 includes the absorption properties and the photovoltaic performance of some polymers shown in Figure 9 and Figure 10.

Table 2. Absorption properties and photovoltaic performance of conjugated polymers in BHJs.

Polymer	**λ_{max} (nm)**	**Optical bandgap (eV)**	**I_{sc} (mA/cm^2)**	**V_{oc} (V)**	**FF**	**η (%)**	**Acceptor**	***D:A ratio***	***Lit.***
P3HT	550	1.9	11.1	0.60	0.54	4.9	[60]PCBM	1:0.8	*40,41*
MEH-PPV	503	2.3	4.8	0.79	0.44	2.1	[60]PCBM	1:4	*45a*
MDMO-PPV	500	2.3	7.6	0.77	0.51	3.0	[70]PCBM	1:4	*45b*
PTBEHT	860	1.2	3.5	0.56	0.58	1.1	[60]PCBM	1:4	*46*
PCPDTBT	780	1.5	16.2	0.62	0.55	5.5	[70]PCBM	1:2	*43*
PCDTBT	550	1.9	10.6	0.88	0.66	6.1	[70]PCBM	1:4	*44*
PBDTTT	690	1.6	15.6	0.56	0.63	5.6	[70]PCBM	1:1.2	*47a*
PBDTTT-CF	680	1.8	13.4	0.76	0.66	6.8	[70]PCBM	1:1.5	*47b*
PTB7	680	1.8	14.5	0.74	0.69	7.4	[70]PCBM	1:1.5	*47c*

Although the prototypical bulk-heterojunction solar cells based on poly(3-hexylthiophene) (P3HT) and phenyl-C_{61}-butyric acid methyl ester (PCBM) can achieve efficiencies of 4-5%,[40,41] the efficiency of P3HT/PCBM cells is limited by the absorption range of P3HT. P3HT absorbs visible light until about 650 nm, meaning that most of the red portion of the visible spectrum and all infrared photons can not be harvested by the P3HT-based photovoltaic cells. Therefore, the low-bandgap polymers have emerged to solve this problem. In terms of polymer-based photovoltaic systems, any polymer with a bandgap less than that of P3HT (that is, less than 1.9 eV) is often referred to as a low-bandgap polymer.[39] The low-bandgap polymers are commonly synthesized in a donor-acceptor approach, in which the alternating electron donating (benzothiadiazole or analogues) and electron accepting moieties are incorporated along the polymer backbone.[42] Figure 10 shows a few of the successful low-bandgap polymers explored so far. Among them, poly[2,6-(4,4-bis-(2-ethylhexyl)-*4H*-cyclopenta[2,1-b;3,4-b′]dithiophene)-*alt*-4,7-(2,1,3-benzothiadiazole)] (PCPDTBT), with a measured optical bandgap of about 1.45 eV, showed an efficiency of 5.5% by using processing additives to optimize the film morphology.[43] Later on, the cell fabricated from a co-polymer poly[N-9''-hepta-decanyl-2,7-carbazole-alt-5,5-(4´,7´-di-2-thienyl-2´,1´,3´-benzothiadiazole) (PCDTBT) and the fullerene derivative [6,6]-phenyl C_{70}-butyric acid methyl ester ([70]PCBM) was reported to give an overall conversion efficiency of 6.1% under one sun illumination and the internal quantum efficiency approaching 100%.[44] Luping Yu et. al. developed a series of novel low-bandgap polymers containing thieno[3, 4-b]thiophene and benzodithiophene units. The first example was poly[4,8-bis-substituted-benzo[1,2-b:4,5-b´]dithiophene-2,6-diyl-alt-4-substituted-thieno[3,4-b]thiophene-2,6-diyl] (PBDTTT), which presented an efficiency of 5.6% in photovoltaic devices.[47a] The alteration of the HOMO of PBDTTT by adding the electron-withdrawing functional group resulted in a polymer (PBDTTT-CF) with a higher efficiency of 6.77%.[47b] Further structural optimization gave the birth to a new low-bandgap copolymer PTB7 which presented a record efficiency of 7.4% in the field of polymer solar cells.[47c] In the mean time, Solarmer company claimed that U.S. Department of Energy's National Renewable Energy Laboratroy (NREL) certified its plastic solar panel efficiency at 7.9%.[48]

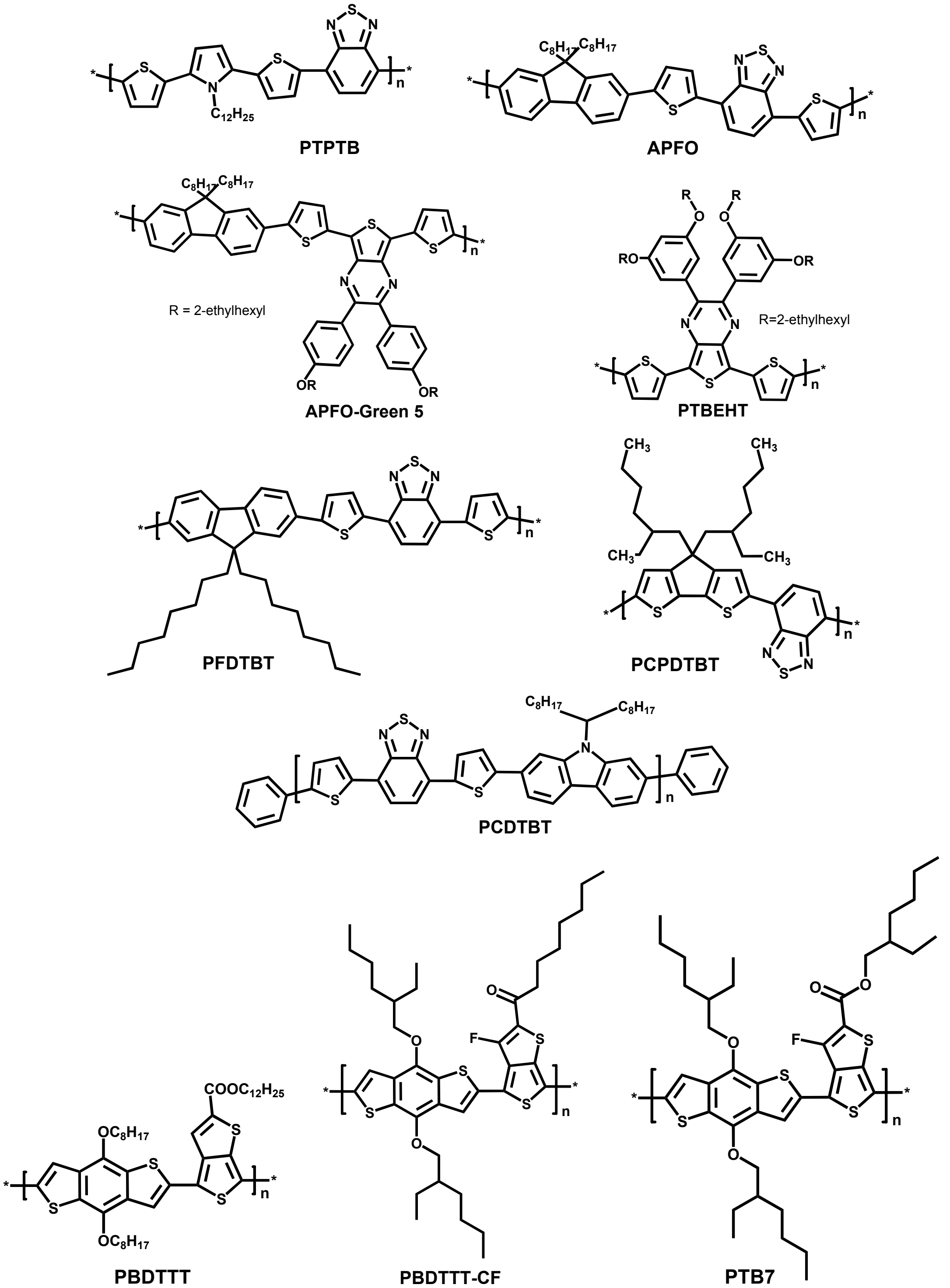

PTPTB **APFO**

APFO-Green 5 **PTBEHT**

PFDTBT **PCPDTBT**

PCDTBT

PBDTTT **PBDTTT-CF** **PTB7**

Figure 10. Chemical structures of low-bandgap polymers used in BHJs.

Despite the impressive progress, there are still many aspects to be considered in exploring new polymers. Many factors need to be taken into account in highly efficient bulk-heterojunction solar cells, especially the properties of the polymers.[39,49] It has been realized that the ideal polymer in BHJ structure should exhibit a broad absorption as well as high absorption coefficients in the solar spectrum to ensure effective light harvesting. The polymers should also possess high hole mobility for charge transport. Further more, the energy levels of polymers should match those of fullerenes, that is, the highest-occupied molecular orbital (HOMO) level of polymers should be low enough to ensure a large open-circuit voltage (Voc) and the lowest unoccupied molecular orbital (LUMO) level offset between polymer and fullerene should be large enough (at least 0.3 eV) for charge separation.[49c] In addition, the morphology of the active layer plays a very important role: the polymers should provide appropriate compatibility with fullerenes to form bicontinuous interpenetrating network on a nanoscale; the domain size in the blend layer is, in the ideal case, twice that of the exciton diffusion length; a large donor/acceptor interface should be formed for favorable exciton dissociation and charge transport.[50]

As mentioned in Chapter 1, for the P3HT/PCBM system, the self-organization ability of the P3HT is believed to contribute greatly to improved film morphology and consequently the high conversion efficiency of the cell. Enormous studies on this system have emphasized the importance of an annealing step for reorganizing the polymer chains to achieve maximum mobility of the charge carriers. The primary consequence of annealing includes an increase in the induced mobility of the charge carriers in the more highly ordered film, an induced red-shift in the absorption onset caused by the better ordering in the polymer backbone and higher degree of intermolecular ordering, and a consequent increase in the absorption coefficient of the ordered polymer.[51] The importance of film morphology was also found by the fact that a slower solvent evaporation process resulted in a more favorable reorganization of P3HT and consequently a higher hole mobility in the device.[52] This indicated that the use of the self-organization ability of polymer and suitable process methods can lead to an optimized phase separation and ordering in the blend which favors the charge generation and charge transport. Based on this respect, in Chapter 4, a new polymer containing benzodithiophene building block, a rigid copolymer utilizing an unsubstituted benzodithiophene moiety to enforce self-organization of the polymer chain, will be introduced in terms of its photovoltaic performance.

2.3 Dye-sensitized Solar Cells (DSSCs)

Dye-sensitized solar cells, also known as Grätzel cells, were invented by Grätzel and O'Regan at École Polytechnique Fédérale de Lausanne (EPFL) in 1991.[3] Up to now, overall conversion efficiency of higher than 11% has been achieved for devices containing liquid electrolytes.[53,71] Their high efficiency and stability make DSSCs become the first organic photovoltaic products in the market.

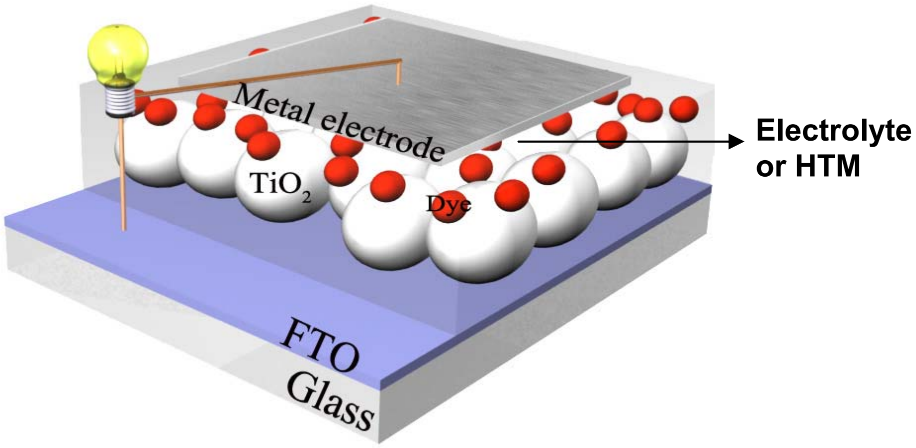

Figure 11. Dye-sensitized solar cell conformation.

A DSSC (Figure 11) contains a fluorine-doped tin oxide (SnO_2:F, FTO) covered glass as anode, a thin wide-bandgap oxide semiconductor, such as TiO_2 film coated on FTO, a single dye layer which is attached to the surface of TiO_2 layer by the dye solution, an electrolyte (liquid-state dye-sensitized solar cell) or hole transport material (HTM) (solid-state dye sensitized solar cell) which fully covers the TiO_2/dye surface and a counter electrode (such as platinum on glass used for electrolyte contained DSSCs, silver or gold electrode for hole transport materials contained solid-state dye-sensitized solar cells.[54]

2.3.1 Liquid-state Dye-Sensitized Solar Cells

The operation mechanism of liquid-state DSSCs is depicted in Scheme 2. In DSSCs, the dye equipped with special anchoring groups is coated on the TiO_2 surface. After irradiation, the dye molecule (S) absorbs a photon, forms an excited state (S*) and leaves an oxidized dye molecule (S^+) on the TiO_2 surface①; the excited dye molecule transfers an electron to the conduction band (CB) of TiO_2 promptly②;

$S^* \rightarrow S^+ + e^-_{CB}$ ①+②

The oxidized dye is subsequently reduced by the electrolyte (the electron donor I-) which transfers an electron to the dye③;

$2S^+ + 3I^- \rightarrow 2S + I_3^-$ ③

The electrolyte consists of an iodide/triiodide (I^-/I_3^-) redox couple which is regenerated by accepting an electron from the counter electrode (platinum sputtered conducting glass)④.

$I_3^- + 2e^- \rightarrow 3I^-$ ④

The injected electron flows through the TiO_2 to the FTO electrode and then through the external load to the counter electrode which completes the circuit. Efficient operation of the DSSCs depends on the control of the interfacial kinetics of electron transfer from the adsorbed sensitizer to the semiconductor electrode and the minimization of the possible recombination pathways which occur at the TiO_2/dye/electrolyte interface. There are two primary interfacial recombination pathways: In the first one, the electrons, which are injected into the TiO_2, may recombine with oxidized dye molecules⑤. This reaction must be intercepted by the regeneration of the dye molecule by electrolyte.[55] The second one is the process that the TiO_2 electrons recombine with the oxidized redox couple⑥. This reaction must be minimized by the full dye coverage of the TiO_2 electrode.

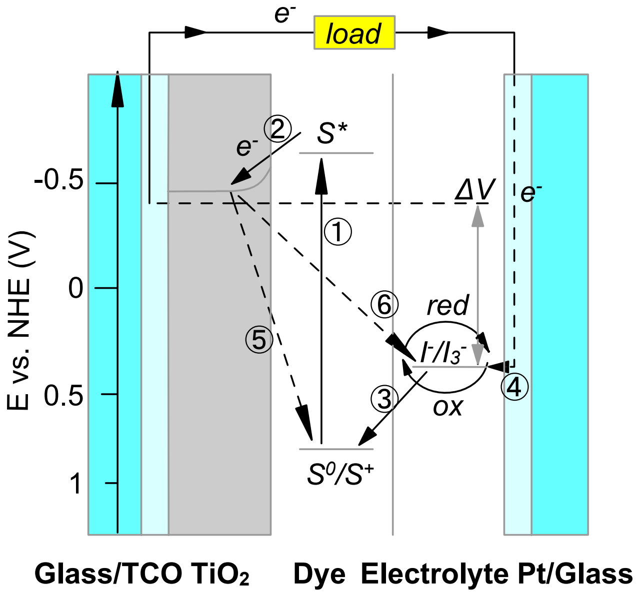

Scheme 2. Schematic representation of the operation mechanism of dye-sensitized solar cells showing photogeneration of the exited state of the sensitizer ①, electron injection into the conduction band of nanoporous TiO_2 ②, regeneration of the dye ground state by electron transfer from the iodide/triiodide redox couple ③, and regeneration of the redox couple by electron injection from the cathode ④.

2.3.2 Solid-state Dye-sensitized Solar Cells

In the liquid-state DSSCs, the problems of solvent evaporation and leakage are unavoidable. To conquer these drawbacks, the iodine-iodide redox couple is replaced by a hole-transport material (HTM) , normally an amorphous material 2,2’,7,7’-tetrakis(N,N-di-*p*-methoxyphenylamine)-9,9’-spirobifluorene (spiro-MeOTAD), in the solid-state dye-sensitized solar cells (Figure 12). One advantage of solid-state devices is the higher Voc obtained than that in liquid electrolyte cells, which stems not only from the more positive redox level of the hole transport material compared to that of electrolyte, but also from the more efficient charge collection through thinner semiconductor film.[56]

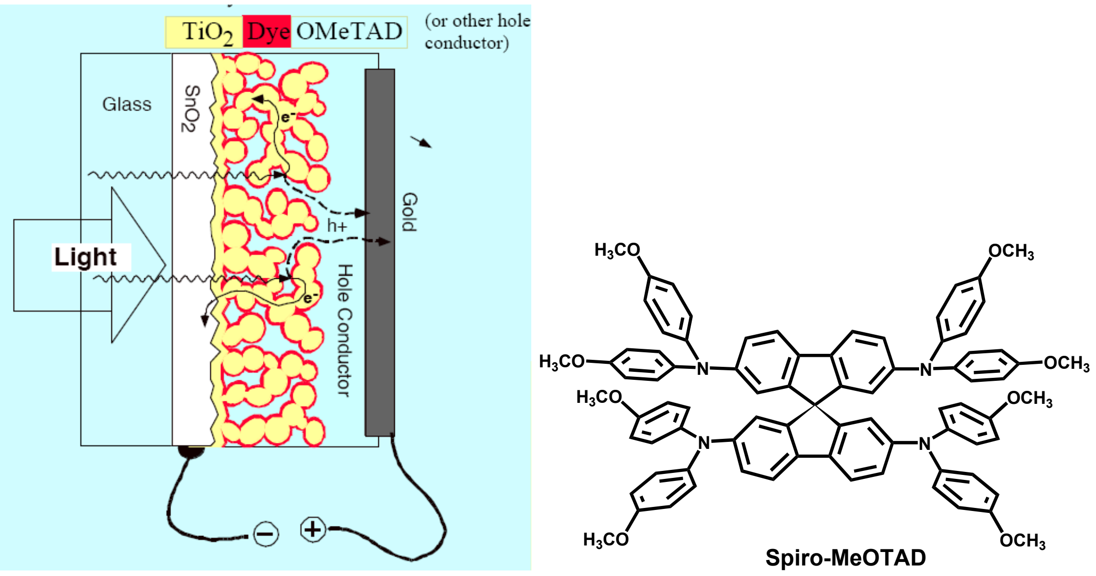

Figure 12. Cross-section image (left) of a solid-state DSSC using spiro-OMeTAD as hole-transport material (right).

However, the overall cell conversion efficiency of solid-state cell is still lower than that observed for the corresponding electrolyte contained cell.[57]

To enhance the efficiency of solid-state devices, the optimization should be carried out in the aspect of all factors, such as TiO_2 films (compact thin TiO_2 film and mesoporous TiO_2 film), sensitizers and hole-transport materials. The fine-tuning of each component and the modification of the interfacial property can only be implemented with a comprehension of all basic elements in the solid-state DSSCs.

2.3.2.1 TiO_2 Films

In a DSC device, the TiO_2 semiconductor functions as the surface for the dye adsorption, the electron acceptor for the excited dye as well as the electron conductor. On top of the FTO glass there are two layers of TiO_2 films with different roles: compact thin TiO_2 underlayer film and mesoporous TiO_2 film.

The compact thin TiO_2 underlayer film not only improves the mechanical adhesion of the mesoporous TiO_2 film on the FTO glass, but also serves as the blocking layer between the hole-transport material and the FTO to retard the recombination of the electrons in FTO with the holes in the hole-transport material. The mesoporous TiO_2 film is used to enhance the interfacial surface area for higher absorption of the light with only a monolayer of adsorbed sensitizer.[58]

The fabrication of this compact thin TiO_2 layer could be implemented by sputtering,[59] spray pyrolysis[60] or sol-gel coating[61]. According to many studies, this layer influences the device efficiency in terms of film thickness. In a thicker compact layer, the series resistance is increased and consequently the fill factor is lowered; due to the blocked electron transport to FTO the photocurrent density will also be decreased. In a thinner film, the amount of pinholes is larger and hence the risk of short circuit between FTO and the hole transport material is higher. By applying the method of spray pyrolysis, a layer thickness of 100-200 nm is found to be appropriate.[62, 58a] However, upon cyclic voltammetry (CV) testing, Zhang *et al.* found that sol-gel derived films in the thickness of 30-40 nm showed the remarkable suppression of the redox peaks, indicating the layer was dense and relatively non-porous. Compared to the 100 nm thick TiO_2 film made by the spray pyrolysis method, a sol-gel made film was more easily processed.[61] Hence, the sol-gel method is applied to make the compact thin TiO_2 films in this thesis.

On top of the blocking compact film, a mesoporous TiO_2 film is layered. To date, nanocrystalline TiO_2 elelctrode is still the predominantly used photoelectrode in DSSCs because of its low-cost, abundant resource, high thermal stability and nontoxicity, [63c,66] although some other oxide semiconductors, such as ZnO[63], SnO_2 [64], Nb_2O_5 [65] have also been investigated. Among these oxide semiconductors, nanocrystalline TiO_2 is shown to be the best electrode for DSSCs. It is found that for a 10 μm thick nanocrystalline semiconductor film, the interfacial surface area can be significantly enhanced by over 1000-fold. Thus the monolayer of adsorbed sensitizer can absorb a large amount of visible light, whereas the dye monolayer adsorbed on a flat interface only gives little light absorption.

The mesoporous film is prepared by doctor-blading a paste containing nanometer-size TiO_2 particles. One facile way is to use the commercially available TiO_2 colloidal paste with different particle sizes. Except this, TiO_2 paste can also be made from commercial TiO_2 powder (P25, from Degussa).[67a] Another choice is preparing the paste by colloidal synthesis developed by Grätzel's group.[67b]

2.3.2.2 Sensitizers

For years, great efforts have been made in the optimization of the sensitizers for DSSCs. One large group contains the transition-metal complexes, such as dyes based on Ru^{II}. Another range of sensitizers are organic molecules.

There are several basic requirements for the sensitizers used in DSSCs: 1) based on thermodynamical grounds, the optimal sensitizer for the DSSC should absorb all photons below a threshold wavelength of around 920 nm, corresponding to a semiconductor bandgap of 1.4 eV. At this threshold, the solar to electric power conversion efficiency of a single-junction device can reach its maximum conversion efficiency of 33%. This means in practice that the absorption coefficient of the dye should be high over the whole spectrum up to around 920 nm so that a minimum amount of dye can be used to absorb most of the light; 2) the sensitizer should be bound strongly to the TiO_2 to ensure the efficient electron injection into the TiO_2 conduction band, so there must be an anchoring group in the molecules, typically carboxylic or phosphonic acid groups; 3) the LUMO level of the sensitizer must be high enough for favorable charge injection into the TiO_2, and the HOMO level must be sufficiently low such that the oxidized sensitizer is regenerated rapidly by the electron donation from the electrolyte or HTM[58a,68,69]; 4) for outdoor high-power applications, the sensitizer should be stable enough to survive at least 15 years of exposure to natural sunlight.

2.3.2.2.1 Ruthenium Complexes

The structures of typical Ru complex sensitizers for DSSCs developed by Grätzel' group are shown in Figure 13. In the early development period of DSSCs, the red dyes **N3** [chemical name: cis-bis(isothiocyanato)-bis(2,2'-bipyridyl-4,4' dicarboxylato)ruthenium(II)] has brought a remarkable progress in this research field owing to its outstanding solar-to-electric energy conversion efficiency of 10%.[70] Its partially deprotonated form **N719** [chemical name: bis(tetrabutylammonium) cis-bis(isothiocyanato)bis(2,2'-bipyridyl-4,4'-dicarboxylato)ruthenium(II)] showed an overall conversion efficiency of 11.18% under one sun light illumination.[71] When applied in the solid state cells, **N719** showed an efficiency of 2.56% under one sunlight illumination[57], and an enhanced performance of 3.2% by using the silver complex of the sensitizer[72].

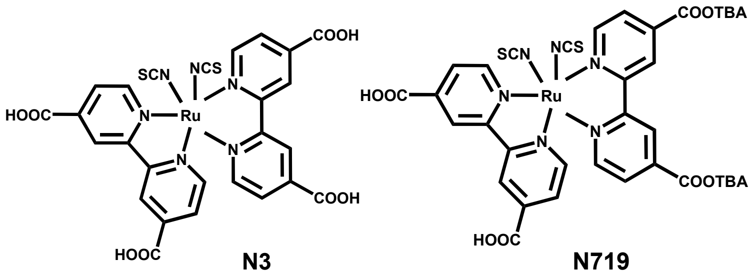

Figure 13. Structures of typical Ru complex sensitizers. TBA is tetrabutylammonium cation, $(C_4H_9)_4N^+$.

Since the main downside of solid-state DSSCs is the fast interfacial electron-hole recombination, many efforts have been made to suppress the charge recombination by applying amphiphilic dyes with hydrophobic spacers and using ion-coordination structures.[58a,68] Amphiphilic ruthenium dyes with hydrophobic spacers showed their advantages in solid-state dye-sensitized solar cells in terms of retarding the electron recombination between hole transport material (HTM) and TiO_2 and improving the interaction between the sensitizer and HTM.[73] By replacing the hydrophobic alkyl chains in dye **Z907** with the ion-coordinating triethylene oxide methyl ether groups, the sensitizer **K51** showed higher voltages than those cells containing its analogue **Z907** (Figure 14).[74] Further modification by adding heptyl groups to the ethylene oxide chains to increase the hydrophobic property in the molecule led to another ion-coordinating analogue **K68** which showed enhanced device efficiency compared to that of **Z907**-containing devices.[75]

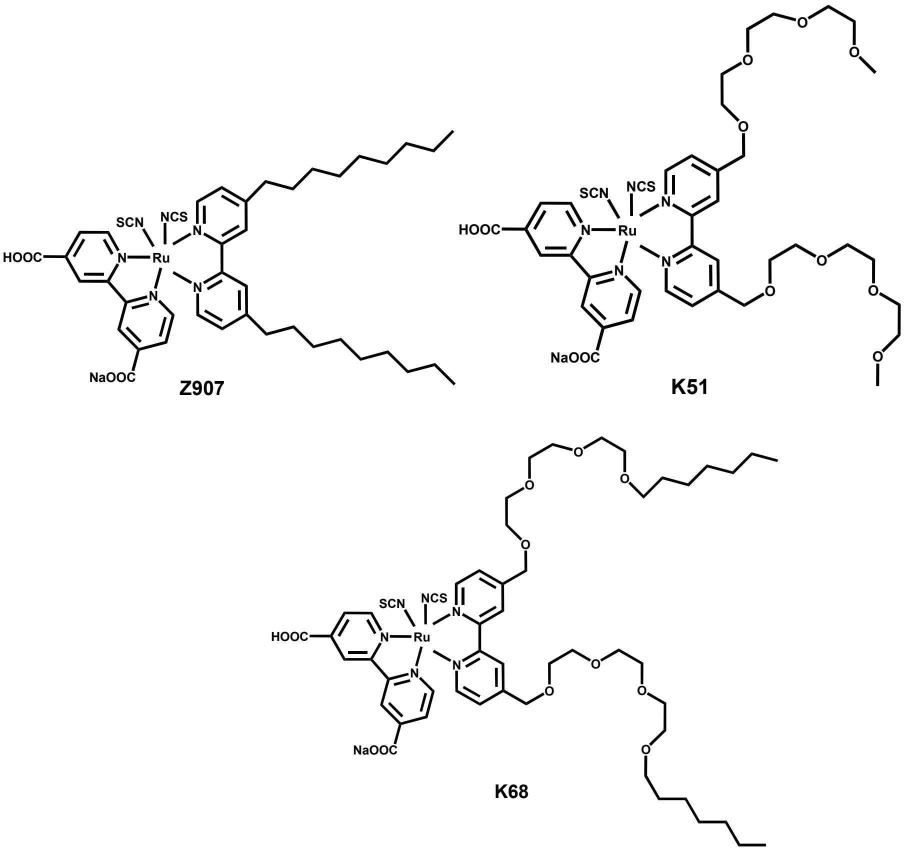

Figure 14. Structures of dyes **Z907**, **K51** and **K68**.

The concept of ‘antenna’ has been also introduced into the sensitizer family. Two donor-antenna dyes, Ru-TPA-NCS and Ru-TPD-NCS (Figure 15), showed high molar absorption coefficients due to the extended delocalization of π-electrons in the donor antenna ligands.[76a,b] The augmented absorption coefficient by increasing the conjugation length of the ancillary ligand is attributed to the following effect: the energy levels of the metal center can be raised by the incorporation of donor anntena onto bipyridine ligands, therefore, the band resulting from metal-to-ligand charge transfer (MLCT) is red-shifted.[76c] Upon light illumination, the electrons on the metal center are transferred to the anchoring ligand more efficiently. This accounts for the enhanced molar absorption coefficient in the sensitizer with an extended π-conjugation system and consequently the high photocurrent density in the cell, since the absorption coefficient of metal-complex sensitizers is due to metal-to-ligand charge transfer (MLCT) absorption.[76d]

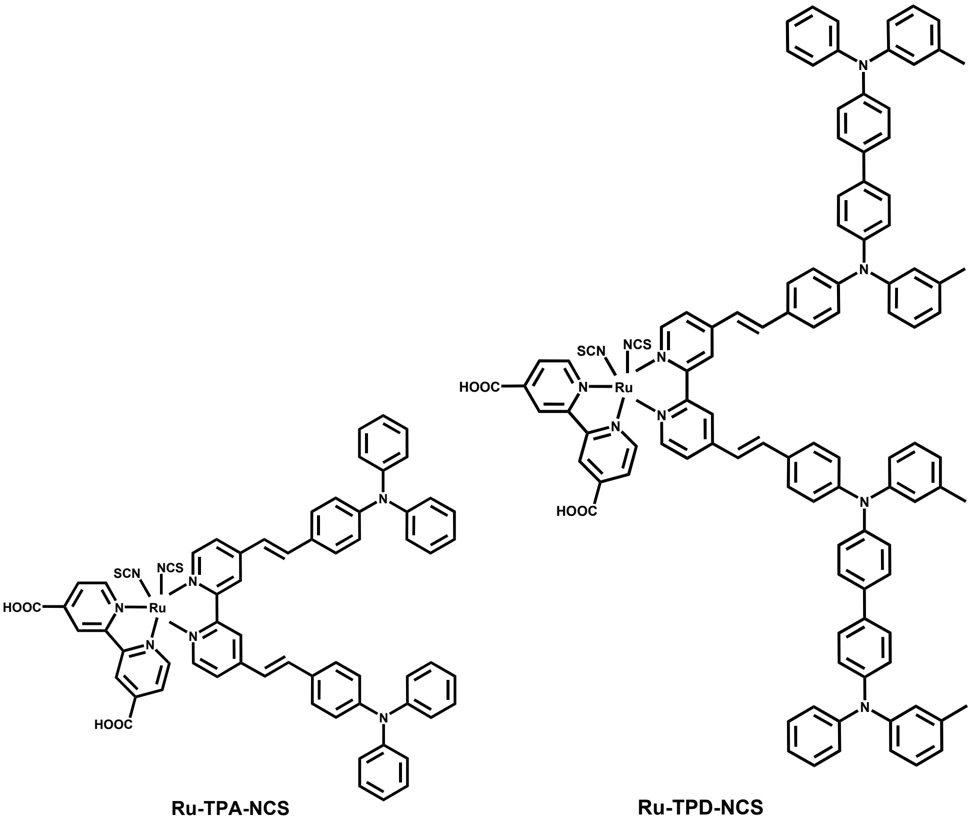

Ru-TPA-NCS **Ru-TPD-NCS**

Figure 15. Structures of Ru-TPA-NCS and Ru-TPD-NCS.

During the last 15 years, a lot of ruthenium dyes have been intensively studied in DSSCs. Table 3 shows some above mentioned ruthenium complexes with their spectral properties and photovoltaic performance in solid-state DSSCs.

Table 3. Absorption properties and solid-state device photovoltaic performance of different ruthenium complexes.

Dye	λ_{max} (nm)	ε (10^4 mol^{-1} cm^{-1})	I_{sc} (mA/cm^2)	V_{oc} (mV)	FF	η	*Lit.*
N719	535	1.36	4.6	931	0.71	3.2%	*72*
Z907	526	1.22	6.9	745	0.60	3.2%	*77*
K51	530	1.23	6.8	875	0.65	3.8%	*77*
K68	528	1.14	7.4	830	0.65	4.0%	*75*
Ru-TPA-NCS	526	2.45	4.4	767	0.34	1.5%	*76*
Ru-TPD-NCS	540	2.66	9.6	757	0.35	3.4%	*76*

2.3.2.2.2 Organic Sensitizers

Up to date, ruthenium complexes for DSSCs are still being investigated extensively. However, due to the drawbacks of metal complexes, like low absorption coefficients, high cost and environmental contamination, metal-free organic dyes have attracted increasing attention as sensitizers for DSSCs. In the liquid-state devices, the conversion efficiency of organic dye based DSSCs is now comparable to that of ruthenium dyes based DSSCs.

The main disadvantage of the organic sensitizers is their stability, which is generally lower than that of metal complexes, because of side reactions such as formation of excited triplet states and unstable radicals.[68] However, organic sensitizers also have several advantages: a wide variety of available natural dyes, high absorption coefficients, low cost and saving of limited metal resources. Their high molar absorption coefficients make organic sensitizers ideal absorbers for solid-state cells which prefers thin film; another advantage is the enhanced open-circuit voltage in these organic sensitizer-contained cells compared to that in the ruthenium complexes-sensitized cells.[58a,68] This is not only due to the redox level of the hole conductor, which is more positive than the respective I^-/I_3^- couple used in the liquid cells, but also because of the thinner TiO_2 film which helps to decrease the dark current.[68]

Up to now, many organic dyes such as perylenes[78], hemicyanines[79], coumarins[80], indolines[81], porphyrins[82], squaraines[56], phthalocyanines[83], and donor-accepter substituted oligothiophenes[84], have been investigated as sensitizers. Figure 16 shows the chemical structures of some organic sensitizers.

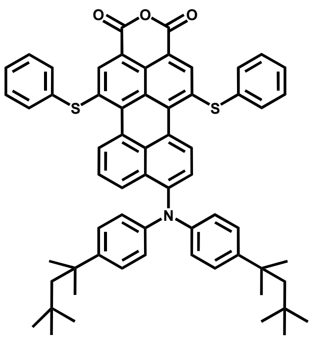

1

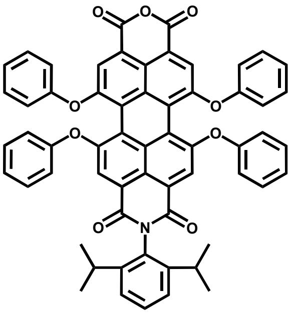

2

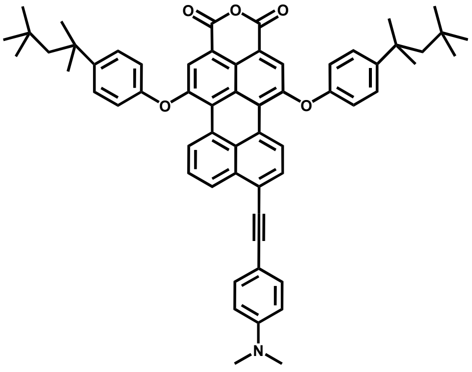

3

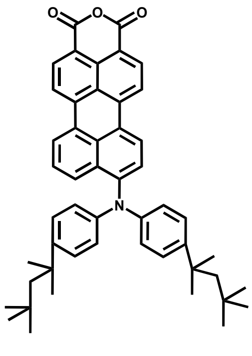

4

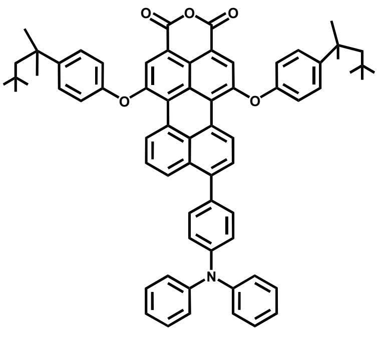

5

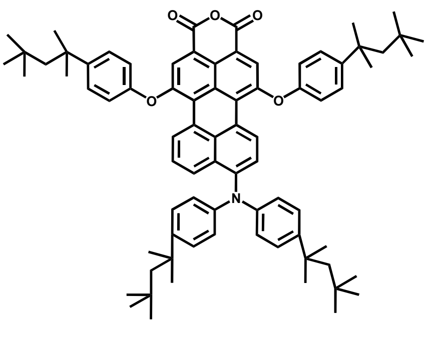

6

Monoanhydride perylenes 1-6

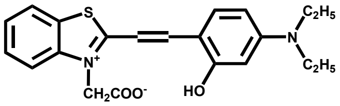

Hemicyanine

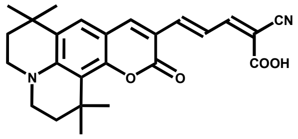

Coumarin

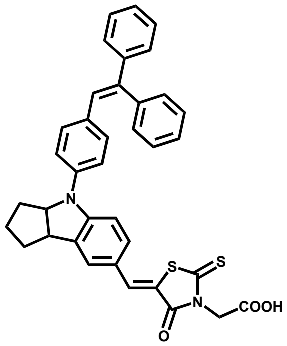

Indoline D102

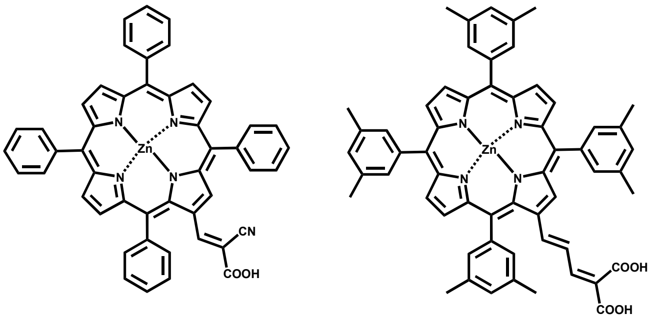

Porphyrins

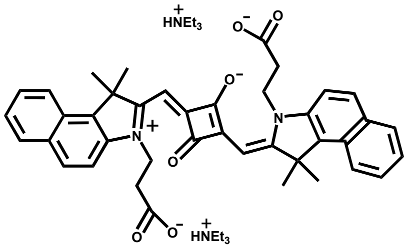

Squaraine B1

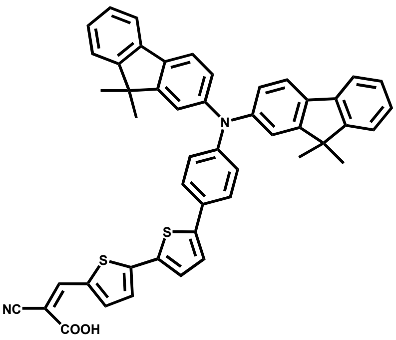

Oligothiophene JK2

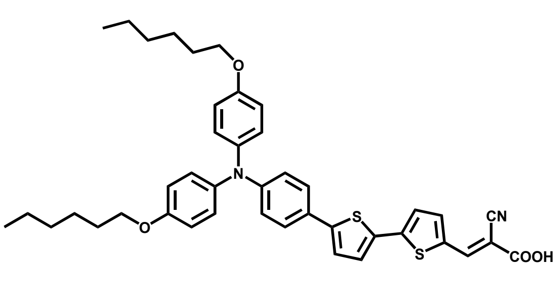

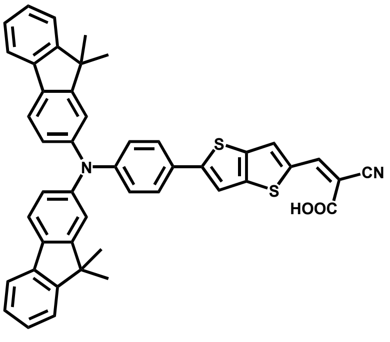

D21L6 **C201**

Figure 16. Structures of some organic sensitizers

Table 4 shows some of the examples of organic dyes with their absorption properties and photovoltaic performance in solid-state DSSCs. An indoline dye **D102** exhibited an overall conversion efficiency of 4.1% due to its extremely high molar absorption coefficient (55,800 L mol^{-1} cm^{-1} at 491 nm, four times stronger than that of ruthenium dye **N3**) which facilitates the realization of both the thinner TiO_2 film and the efficient absorption of incoming light.[81c] For a sufficient light absorption, the overlap of sensitizer's absorption spectrum with that of solar irradiation should be as large as possible. A green Zn-porphyrin dye, with a maximum of absorption at 618 nm in the red range of solar irradiation spectrum, has exhibited an overall conversion efficiency of 3%.[82] An organic sensitizer **D21L6** containing two thiophene moieties presented an efficiency of 4.4% in the solid-state cells.[68] A D-π-A sensitizer **C201** employing a bridging unit of fused thiophene dimer was reported to reach 4.8% conversion efficiency in a solid-state cell. [85]

Table 4. Absorption properties and solid-state device photovoltaic performance of different organic sensitizers.

Dye	λ_{max} (nm)	ε (10^4mol^{-1}cm^{-1})	I_{sc} (mA/cm^2)	V_{oc} (mV)	FF	η	*Lit.*
Perylene 1	620	2.3	2.8	838	0.75	1.8 %	*78b*
Zn-1	620	1.2	5.0	731	0.66	2.4 %	*82*
Zn-2	618	1.3	5.9	790	0.65	3.0 %	*82*
D102	491	5.6	7.7	866	0.61	4.1%	*81c*
Squaraine B1	679	20	4.2	681	0.53	1.5 %	56
D21L6	458	3.7	9.6	798	0.57	4.4 %	68
C201	514	4.1	9.1	860	0.61	4.8 %	85

As metal-free dyes, perylene derivatives have also been widely applied in various optical devices owing to their outstanding chemical, thermal and photochemical stability and non-toxicity.[78] In our group, many perylene sensitizers have been designed, synthesized and applied in the DSSCs. Recently, our group reported a highly efficient novel perylene sensitizer, which yielded 87% IPCE (incident photon to current conversion efficiency) and 6.8% power conversion efficiency in liquid cells and 1.8% power conversion efficiency in solid-state cells under standard illumination conditions.[78b] The application of a new perylene sensitizer in dye-sensitized solar cells will be discussed in details in Chapter 5.

2.3.2.3 Hole-transport Materials (HTM)

The hole-transport material in a SSD device should fulfill several requirements: electrochemically, the redox potential of the HTM must be more negative than that of the oxidized sensitizer to provide a driving force for the dye regeneration; photochemically, the HTM should not have significant light absorption in the visible range, to avoid internal filter effects; morphologically, the HTM should have effective penetration into the semiconductor pores, therefore, a material with high glass transition temperature and low molecular weight is preferable; in the aspect of charge transport, the HTM should have a certain level of conductivity and hole mobility.

Up to now, the most successful hole-transporting material used in the solid-state dye-sensitized solar cells is spiro-OMeTAD due to its respectable hole mobility of 10^{-4} cm^2 V^{-1} s^{-1}, amorphous nature, high solubility and small size.[86] The purpose of the spiro linkage is to raise the glass transition temperature, T_g, from near 60ºC for trimethoxyphenyl amine, to 120 ºC. This keeps the material in the amorphous state over the likely operating temperatures of the cell, since the existence of crystallization will retard the effective pore-filling. The small size of the spiro-OMeTAD and its good solubility in organic solvents is favourable for the effective penetration of the hole-transport material into the pores of the nanoporous TiO_2 film.[87]

The efforts to find alternative HTM have been put on some other spiro-linked triphenyldiamine materials with higher hole mobility[88] and non-spiro-linked triaylamine HTMs with better elelctronic properties[89]. However, the experimental results showed that there was no clear correlation between hole mobility and device performance. Nonetheless, it was found that pore filling and the control of interfacial energetic should be critical for the optimization of HTMs. These two aspects are the directions for further optimization of the HTMs.

The optimal hole conductor matrix has been found out to be a solution of spiro-MeOTAD (0.15M) in chlorobenzene, containing $Li(CF_3SO_2)_2N$ (30mM), 4-*tert*-butylpyridine (tBP) (0.11M) and $N(PhBr)_3SbCl_6$ (0.4mM).[90] Related studies showed that a suitable amount of tBP and lithium salt in the hole-transport solution is required for the best photovoltaic performance.

Normally, devices without tBP show very bad performance, indicating that tBP is very important for the device function. However, overfull amount of tBP had a bad influence on the device performance. If the charge transport in the hole conductor cannot keep up with the charge generation, this will lead to the build-up of an electric field at the interface which facilitates the interfacial charge recombination.[90] Normally, the introduction of tBP results in a drastic enhancement in Voc, which is due to its blocking effect on the recombination. The presence of tBP also assists the dissolution of the lithium salt in the spiro-MeOTAD.[90]

The beneficial effect of lithium salt $Li(CF_3SO_2)_2N$ is attributed to its high mobility in organic media and its capability to intercalate into the TiO_2 network.[90]

2.3.2.4 Counter Electrode

The counter electrode should have a high conductivity and match with the work function of HTM. Metals with high work function, such as gold and platinum, can function as counter electrode in the DSSCs. The controllable and reproducible property of thermal evaporation or sputtering technique can be applied for the fabrication of metal electrodes. In this thesis, gold electrodes were used due to the simple processing and high reproducibility.

2.4 References

[1] P. Peumans, S. Uchida, S. R. Forrest, *Nature,* **2003**, *425*, 158.

[2] G.Yu, J.Gao, J. C.Hummelen, F.Wudl, A. J.Heeger, *Science,* **1995**, *270*, 1789.

[3] B. O'Regan, M.Grätzel, *Nature,* **1991**, *353*, 737.

[4] U. Bach, D.Lupo, P.Comte, J. E.Moser, F.Weissortel, J. Salbeck, H. Spreitzer, M.Grätzel, *Nature,* **1998**, *395*, 583.

[5] M. Riede, T. Müller, W. Tress, R. Schüppel, K. Leo, *Nanotechnology*, **2008**, *19*, 424001.

[6] M. R. Lee, R. D. Eckert, K. Forberich, G. Dennler, C. J. Brabec, R. A. Gaudiana, *Science,* **2009**, *324*, 232.

[7] P. A. van Hal, M. M. Wienk, J. M. Kroon, W. J. H. Verhees, L. H. Slooff, W. J. H. van Gennip, P. Jonkheijm, R. A. J. Janssen, *Adv. Mater.* **2003**, *15*, 118.

[8] Y. Cao, G. Yu, C. Zhang, R. Menon, A. J. Heeger, *Synth. Met.* **1997**, *87*, 171.

[9] G. Heywang, F. Jonas, *Adv. Mater.* (Weinheim, Ger.) **1992**, *4*, 116.

[10] V. Choong, Y. Park, Y. Gao, T. Wehrmeister, K. Mullen, B. R. Hsieh, C. W. Tang, *Appl. Phys. Lett.* **1996**, *69*, 1492.

[11] J. J. M. Halls, K. Pichler, R. H. Friend, S. C. Moratti, A. B. Holmes, *Appl. Phys. Lett.* **1996**, *68*, 3120.

[12] J. J. M. Halls, R. H. Friend, *Synth. Met.* **1997**, *85*, 1307.

[13] X. Yang, J. Loos, S. C. Veenstra, W. J. H. Verhees, M. M. Wienk, J. M. Kroon, M. A. J. Michels, R. A. J. Janssen, *Nano Lett.* **2005**, *5*, 579.

[14] D. E. Markov, C. Tanase, P. W. M. Blom, J. Wildeman, *Phys. Rev. B,* **2005**, *72*, 045217.

[15] L. E. Scriven, *Nature*, **1976**, *263*, 123.

[16] P. W. M. Blom, V. D. Mihailetchi, L. J. A. Koster, D. E. Markov, Adv. Mater. **2007**, *19*, 1551.

[17] http://en.wikipedia.org/wiki/Exciton.

[18] P. Peumans, A. Yakimov, S.R. Forrest, *J. Appl. Phys.* **2003**, *93*, 3693.

[19] D. E. Markov, E. Armsterdem, P. W. M. Blom, A. B. Sival, J. C. Hummelen, *J. Phys. Chem. A,* **2005**, *109*, 5266.

[20] A. Haugeneder, M. Neges, C. Kallinger, W. Spirkl, U. Lemmer, J. Feldmann, U. Scherf, E. Harth, A. Gügel, K. Müllen, *Phys. Rev. B,* **1999***, 59,* 15346.

[21] M. Theander, A. Yartsev, D. Zigmantas, V. Sundstrom, W. Mammo, M. R. Andersson, O. Inganäs, *Phys. Rev. B,* **2000**, *61*, 12957.

[22] V. Bulovic, S. R. Forrest, *Chem. Phys.* **1996**, *210*, 13.

[23] L.-G. Yang, H.-Z. Chen, M. Wang, *Thin Solid Films,* **2008**, *516*, 7701.

[24] L. A. A. Pettersson, L. S. Roman, O. Inganäs, *J. Appl. Phys.* **1999**, *86*, 487.

[25] T. Stubinger, W. Brutting, *J. Appl. Phys.* **2001**, *90*, 3632.

[26] T. J. Savenije, J. M. Warman, A. Goossens, *Chem. Phys. Lett.* **1998**, *287*, 148

[27] R. H. Bube, *Photoelectronic Properties of Semiconductors*, Cambridge University Press, Cambridge, **1992**.

[28] M. Pope, C. E. Swenberg, *Electronic Process in Organic Crystals and Polymers*, Oxford University Press, Oxford, **1999**.

[29] S.-S. Sun, N. S. Sariciftci, *Organic Photovoltaics Mechanisms, Materials, and Devices*, CRC Press, **2005**.

[30] (a) C. Brabec, U. Scherf, and V. Dyakonov, *Organic Photovoltaics*, Wiley VCH, Weinheim, Germany, **2008**; (b) C. Deibel, *Phys. Status Solidi A*, **2009**, *12*, 2731.

[31] (a) D. M. Adams, L. Brus, C. E. D. Chidsey, S. Creager, C. Creutz, C. R. Kagan, P. V. Kamat, M. Lieberman, S. Lindsay, R. A. Marcus, R. M. Metzger, M. E. Michel-Beyerle, J. R. Miller, M. D. Newton, D. R. Rolison, O. Sankey, K .S. Schanze, J. Yardley, X. Zhu, J. Phys. Chem. B, 2003, 107, 6668; (b) H. Sumi, R. A. Marcus, J. Chem. Phys. 1986, 84, 4894.

[32] J. Li, Ph.D thesis, MPIP(Germany), 2006.

[33] http://www.physik.uni-wuerzburg.de/EP6/research-oe.html

[34] S. Chandrasekhar, B. K. Sadashiva, K. A. Suresh, Pramana 1977, 9, 471.

[35] B. A. Gregg, M. A. Fox and A. J. Bard, *J. Phys. Chem.* **1990**, *94*, 1586.

[36] L. Schmidt-Mende, A. Fechtenkotter, K. Müllen, E. Moons, R. H. Friend, J. D. Mackenzie, *Science*, **2001**, *293*, 1119.

[37] A. M. van de Craats, J. M. Warman, A. Fechtenkötter, J. D. Brand, M. A. Harbison, K. Müllen, *Adv. Mater.* **1999**, *11*, 1469.

[38] J. Li, M. Kastler, W. Pisula, J. W. F. Fobertson, D. Wasserfallen, A. C. Grimsdale, J. Wu, K. Müllen, *Adv. Funct. Mater.* **2007**, *17*, 2528.

[39] B. C. Thompson, J. M. Frechet, *Angew. Chem. Int. Ed.* **2008**, *47*, 58.

[40] M. Reyes-Reyes, K. Kim, D. L. Carroll, *Appl. Phys. Lett.* **2005**, *87*, 083506.

[41] G. Li, V. Shrotriya, J. Huang, Y. Yao, T. Moriarty, K. Emery, Y. Yang, *Nat. Mater.* **2005**, *4*, 864.

[42] H. A. M. van Mullekom, J. A. J. M. Vekemans, E. E. Havinga, E. W. Meijer, *Mater. Sci. Eng. R,* **2001**, *32*, 1.

[43] J. Peet, J. Y. Kim, N. E. Coates, W. L. Ma, D. Moses, A. J. Heeger, G. C. Bazan, *Nat. Mater.* **2007***, 6,* 497.

[44] S.-H. Park, A. Roy, S. Beaupre, S. Cho, N. Coates, J-S. Moon, D. Moses, M. Leclerc, K. Lee, A. J. Heeger, *Nature Photonics*, **2009**, *3*, 297.

[45] (a) E. C. Chang, C.-I. Chao, R.-H. Lee, *J. Appl. Polym. Sci.* **2006**, *101*, 1919; (b) M. M. Wienk, J. M. Kroon, W. J. H. Verhees, J. Knol, J. C. Hummelen, P. A. Van Hal, R. A. Janssen, *Angew. Chem. Int. Ed.* **2003**, *42*, 3371.

[46] M. M. Wienk, M. G. R. Turbiez, M. P. Struijk, M. Fonrodona, R. A. J. Janssen, *Appl. Phys. Lett.* **2006**, *88*, 153511.

[47] (a) Y. Liang, Y. Wu, D. Feng, S.-T. Tsai, S.-J. Son, G. Li, L. Yu, *J. Am. Chem. Soc.* **2009**, *131*, 56; (b) H.-Y. Chen, J. Hou, S. Zhang, Y. Liang, G. Yang, Y. Yang, L. Yu, Y. Wu, G. Li, *Nature Photonics*, **2009**, *3*, 649; (c) Y. Liang, Z. Xu, J. Xia, S.-T. Tsai, Y. Wu, G. Li, C. Ray, L.Yu, *Adv. Mater.* **2010**, published online.

[48]http://www.renewableenergyworld.com/rea/news/article/2009/12/solarmer-achieves-7-9-nrel-certified-plastic-solar-cell-efficiency

[49] (a) S. Gnes, H. Neugebauer, N. S. Sariciftci, *Chem. Rev.* **2007**, *107*, 1324; (b) G. Li, V. Shrotriya, Y. Yao, J. S.Huang, Y. Yang, *J. Mater. Chem.* **2007**, *17*, 3126; (c) M. Scharber, D. Mühlbacher, M. Koppe, P. Denk, C. Waldauf, A. J. Heeger, C. Brabec, *Adv. Mater*. **2006**, *18*, 789.

[50] (a) X. N. Yang, J. Loos, *Macromolecules* **2007**, *40*, 1353; (b) G. Li, Y. Yao, H. C. Yang, V. Shrotriya, G. W. Yang, Y. Yang, *Adv. Funct. Mater.* **2007**, *17*, 1636; (c) W. Ma, A. Gopinathan, A. J. Heeger, *Adv. Mater.* **2007**, *19*, 3656.

[51] (a) V. D. Mihailetchi, H. Xie, B. de Boer, L. J. A. Koster, P.W. M. Blom, *Adv. Funct. Mater.* **2006**, *16*, 699; (b) T. Erb, U. Zhokhavets, G. Gobsch, S. Raleva, B. Stuhn, P. Schilinsky, C. Waldauf, C. J. Brabec, *Adv. Funct. Mater.* **2005**, *15*, 1193.

[52] V. D. Mihailetchi, H. Xie, B. de Boer, L. M. Popescu, L. J. A. Koster, *Appl. Phys. Lett.* **2006**, *89*, 012107.

[53] F. Cao, Y. Wang, D. Shi, J. Zhang, M. Wang, X. Jing, R. Humphry-Baker, P. Wang, S. M. Zakeeruddin, M. Grätzel, *J. Am. Chem. Soc.* **2008**, *130*, 10720.

[54] (a) A. Hagfeldt, M. Graetzel, *Chem. Rev.* **1995**, *95*, 49; (b) M. Gratzel, *MRS Bull.* **2005**, *30*, 23.

[55] (a) F. Fabregat-Santiago, J. Bisquert, G. Garcia-Belmonte, G. Boschloo, A. Hagfeldt, *Sol. Energy Mater. Sol. Cells,* **2005**, *87*, 117; (b) J. Nissfolk, K. Fredin, A. Hagfeldt, G. Boschloo, J. Phys. Chem. B, 2006, 110, 22950.

[56] A. Burke, L. Schmidt-Mende, S. Ito, M. Grätzel, *Chem. Commun.* **2007**, 234.

[57] J. Kruger, R. Plass, L. Cevey, M. Piccirelli, M. Grätzel, U. Bach, *Appl. Phys. Lett.* **2001**, 79, 2085.

[58] (a) J-H. Yum, P. Chen, M. Grätzel, M. K. Nazeeruddin, *ChemSusChem,* **2008**, *1*, 699; (b) U. Bach, PhD thesis, EPFL (Switzerland), **2000.**

[59] B. Peng, G. Jungmann, C. Jäger, D. Haarer, H-W. Schmidt, M. Thelakkat, *Coord. Chem. Rev.* **2004**, *248*, 1479.

[60] L. Kavan, M. Grätzel, *Electrochim. Acta* **1995**, *40*, 643.

[61] (a) C. D. Grant, A. M. Schwartzberg, G. P. Smestad, J. Kowalik, L. M. Tolbert, J. Z. Zhang, Synth. Met. **2003**, *132*, 197; (b) S. Mahshid, M. Askari, M. S. Ghamsari, *J. Mater. Processing Tech.* **2007**, *189*, 296.

[62] C. S. Karthikezan, M. Thelakkat, *Inorg. Chim. Acta* **2008**, *361*, 635.

[63] (a) C. Y. Jiang, X. W. Sun, G. Q. Lo, D. L. Kwong, *Appl. Phys. Lett.* **2007**, *90*, 263501; (b) Q. Zhang, C. S. Dandeneau, X. Zhou, G. Cao, *Adv. Mater.* **2009**, *21*, 4087; (c) M.Quintana, T. Edvinsson, A. Hagfeldt, G. Boschloo, *J. Phys. Chem. C*, **2007**, *111*, 1035.

[64] (a) F. Fungo, L. Otero, E.N. Durantini, J.J. Silber, L.E. Sereno, *J. Phys. Chem. B* **2000**, *104,* 7644; (b) S. Chappel, A. Zaban, *Sol. Energy Mater. Sol. Cells,* **2002**, *71*, 141.

[65] F. Lenzmann, J. Krueger, S. Burnside, K. Brooks, M. Gratzel, D. Gal, S. Ruhle, D. Cahen, *J. Phys. Chem. B*, **2001**, *105*, 6347.

[66] X. Chen, S. S. Mao, *Chem. Rev.* **2007**, *107*, 2891.

[67] (a) Z. Zhang, P. Chen, T. N. Murakami, S. M. Zakeeruddin, M. Grätzel, *Adv. Func. Mater.* **2008**, *18*, 341 ; (b) C. J. Barbe, F. Arendse, P. Comte, M. Jirousek, F. Lenzmann, V. Shklover, M. Grätzel, *J. Am. Ceram. Soc.* **1997**, *80*, 3157.

[68] J.-H. Yum, D. P. Hagberg, S.-J. Moon, K. M. Karlsson, T. Marinado, L. Sun, A. Hagfeldt, M. K. Nazeeruddin, M. Grätzel, *Angew. Chem.* **2009**, *121*, 1604.

[69] N. Robertson, *Angew. Chem. Int. Ed.* **2006**, *45*, 2338.

[70] M. K. Nazeeruddin, A. Kay, I. Rodicio, R. Humphry-Baker, E. Müller, P. Liska, N. Vlachopoulos, M. Grätzel, *J. Am. Chem. Soc.* **1993**, *115*, 6382.

[71] M. K. Nazeeruddin, F. De Angelis, S. Fantacci, A. Selloni, G. Viscardi, P. Liska, S. Ito, B. Takeru, M. Grätzel, *J. Am. Chem. Soc.* **2005**, *127*, 16835.

[72] J. Krüger, R. Plass, M. Grätzel, H.-J. Matthieu, *Appl. Phys. Lett.* **2002**, *81*, 367.

[73] L. Schmidt-Mende, S. M. Zakeeruddin, M. Grätzel, *Appl. Phys. Lett.* **2005**, 86, 013504.

[74] D. Kuang, C. Klein, H. J. Snaith, J. Moser, R. Humphry-Baker, P. Comte, S. M. Zakeeruddin, M. Grätzel, *Nano Lett.* **2006**, *6*, 769.

[75] D. Kuang, C. Klein, H. J. Snaith, R. Humphry-Baker, S. M. Zakeerudin, M. Grätzel, *Inorg. Chim. Acta*, **2008**, *361*, 699.

[76] (a) C. S. Karthikeyan, K. Peter, H. Wietasch, M. Thelakkat, *Sol. Energy Mater. Sol. Cells,* **2007**, *91*, 432; (b) C. S. Karthikeyan, H. Wietasch, M. Thelakkat, *Adv. Mater.* **2007**, *19*, 1091; (c) C.-Y. Chen, S.-J. Wu, C.-G. Wu, J.-G. Chen, K.-C. Ho, *Angew. Chem.* **2006**, *118*, 5954; (d) K. Hara, T. Sato, R. Katoh, A. Furube, Y. Ohga, A. Shinpo, S. Suga, K. Sayama, H. Sugihara, H. Arakawa, *J. Phys. Chem. B*, **2003**, *107*, 597.

[77] H. J. Snaith, S. M. Zakeeruddin, L. Schmidt-Mende, C. Klein, M. Grätzel, *Angew. Chem. Int. Ed.* **2005**, *44*, 6413.

[78] (a) T. Edvinsson, C. Li, N. Pschirer, J. Schoeneboom, F. Eickemeyer, R. Sens, G. Boschloo, A. Herrmann, K. Müllen, A. Hagfeldt, *J. Phys. Chem. C,* **2007**, *111*, 15137; (b) C. Li, J-H. Yum, S-J. Moon, A. Herrmann, F. Eickemeyer, N. G. Pschirer, P. Erk, J. Schöneboom, K. Müllen, M. Grätzel, M. K. Nazeeruddin, *ChemSusChem*, **2008**, *1*, 615; (c) C. Li, Ph.D thesis, Germany, **2008**; (d) T. Dentani, K. Funabiki, J.-Y. Jin, T. Yoshida, H. Minoura, M. Matsui, *Dyes & Pigments,* **2007**, *72*, 303; (e) S. Ferrere, B. A. Gregg, *New J. Chem.* **2002**, *26*, 1155; (f)Y. Shibano, T. Umeyama, Y. Matano, H. Imahori, *Org. lett.* **2007**, *9*, 1971; (g) S. Wang, Y. Li, C. Du, Z. Shi, S. Xiao, D. Zhu, E. Gao, S. Cai, *Synth. Met.* **2002**, *128*, 299; (h) C. Zafer, M. Kus, G. Turkmen, H. Dincalp, S. Demic, B. Kuban, Y. Teoman, S. Icli, *Sol. Energy Mater. Sol. Cells,* **2007**, *91*, 427.

[79] (a) Y.-S. Chen, C. Li, Z.-H. Zeng, W.-B. Wang, X.-S. Wang, B.-W. Zhang, *J. Mater. Chem.* **2005**, *15*, 1654; (b) E. Stathatos, P. Lianos, A. Laschewsky, O. Ouari, P. Van Cleuvenbergen, *Chem. Mater.* **2001**, *13*, 3888; (c) Q.-H. Yao, F.-S. Meng, F.-Y. Li, H. Tian, C.-H. Huang, *J. Mater. Chem.* **2003**, *13*, 1048.

[80] (a) Z.-S. Wang, Y. Cui, K. Hara, Y. Dan-oh, C. Kasada, A. Shinpo, *Adv. Mater.* **2007**, *19*, 1138; (b) K. Hara, K. Sayama, H. Arakawa, Y. Ohga, A. Shinpo, S. Suga, *Chem. Commun.* **2001**, 569.

[81] (a) T. Horiuchi, H. Miura, K. Sumioka, S. Uchida, *J. Am. Chem. Soc.* **2004**, *126*, 12218; (b) T. Horiuchi, H. Miura, S. Uchida, *Chem. Commun.* **2003**, 3036; (c) Schmidt-Mende, U. Bach, R. Humphry-Baker, T. Horiuchi, H. Miura, S. Ito, S. Uchida, M. Grätzel, *Adv. Mater.* **2005**, *17*, 813.

[82] L. Schmidt-Mende, W. M. Campbell, Q. Wang, K. W. Jolley, D. L. Officer. M. K. Nazeeruddin, M. Grätzel, *ChemPhysChem,* **2005**, *6*, 1253.

[83] Y. Reddy, L. Giribabu, C. Lyness, H. J. Snaith, C. Vijaykumar, M. Chandrasekharam, M. Lakshmikantam, J.-H. Yum, K. Kalyanasundaram, M. Grätzel, M. K. Nazeeruddin, *Angew. Chem.* **2007**, *119*, 377; *Angew. Chem. Int. Ed.* **2007**, *46*, 373.

[84] (a) S. Kim, J. K. Lee, S. O. Kang, J. Ko, J. H. Yum, S. Fantacci, F. De Angelis, D. Di Censo, M. K. Nazeeruddin, M. Grätzel, *J. Am. Chem. Soc.* **2006**, *128*, 16701; (b) J.-H. Yum, S.-R. Jang, P. Walter, T. Geiger, F. Nueesch, S. Kim, J. Ko, M. Grätzel, M. K. Nazeeruddin, *Chem. Commun.* **2007**, 4680.

[85] M. Wang, M. Xu, D. Shi, R. Li, F. Gao, H. Zhang, Z. Yi, R. Humphry-Baker, P. Wang, S. M. Zakeeruddin, M. Grätzel, *Adv. Mater.* **2008**, *20*, 4460.

[86] D. Poplavskyy, J. Nelson, *J. Appl. Phys.* **2003**, *93*, 341.

[87] H. J. Snaith, L. Schmidt-Mende, *Adv. Mater.* **2007**,1*9*, 3187.

[88] N. Rossier-Iten, Ph.D thesis, EPFL (Switzerland), **2000**.

[89] J. E. Kroeze, N. Hirata, L. Schmidt-Mende, C. Orizu, S. D. Ogier, K. Carr, M. Grätzel, J. R. Durrant, *Adv. Funct. Mater.* **2006**, *16*, 1832.

[90] J. Krüger, Ph.D Thesis, EPFL (Switzerland), **2003.**

Chapter 3 Supramolecular Organization and Photovoltaics of the Triangle-shaped Discotic Graphenes

As already mentioned in Chapter 2, the donor and acceptor materials generally should have self-organizable ability to form phase separation, which enhances the continuous path construction for the electron/hole collection to the respective electrodes. The supramolecular assemblies of disc-shaped molecules lead to the formation of discotic liquid crystals that offers very high charge carrier mobility in columnar mesophases, which makes these molecules favorable for application in field-effect transistors (FETs),[1] photovoltaic cells,[2] and molecular electronic devices.[3] In this chapter, the main focus will be located on the supramolecular organization and photovoltaics of the triangle-shaped discotic graphene molecule with swallow-tailed alkyl substituents.

3.1 Introduction

Alkyl substituted polycyclic aromatic hydrocarbons (PAHs) as molecularly defined nanographenes with columnar superstructures formed by π-stacking[4] exhibit the highest local charge-carrier mobilities for discotics. It is expected that larger aromatic cores will lead to discotic liquid crystals with enhanced columnar stability and supramolecular order and thus to materials with improved charge-carrier transport due to the more extended π-orbital overlap.

However, the increased π-orbital overlap is typically accompanied by a drastic limitation in processibility from both solution and vacuum.[5]

The introduction of alkyl substituents, possessing a pronounced steric demand, is an effective tool to enhance the solubility which is also crucial for the purification and device fabrication.[6] Additionally, the variation of alkyl side chains (linear versus branched) allows a precise control over the thermotropic properties of the material.[6]

The formation of the liquid crystalline state represents a significant advantage for the implementation of discotic graphenes into electronic devices. For instance, upon annealing at elevated temperatures, self-assembly occurs improving (macro)molecular packing and diminishing the number of local defects and macroscopic grain boundaries which impede the charge carrier transport through the organic semiconductor.[7] Monodomains of low weight liquid crystals prevent film shrinkage and ensure in this way an enhanced operation of solution processed, but thermally treated FET devices.[8] On the other hand, there are only very few examples for large discotics which possess a liquid crystalline state over a broad temperature range including ambient conditions.[9]

In order to elucidate the influence of the molecular design on the self-organization behavior and further to understand the relationship between the bulk organization and device performance after thermal processing, bulk heterojunction photovoltaic cells provide meaningful test experiments.[10] For example, the efficiency of photovoltaic devices, which were fabricated from a blend of hexa-peri-hexabenzocoronene (HBC) as donor and N,N´-bis(1-ethylpropyl)-3,4,9,10-perylenetetracarboxydiimide (PDI) as acceptor, displayed a strong dependence on the peripheral architecture of HBC, supramolecular order and morphology.[2]

Herein, the attention was focused on the triangle-shaped discotic graphenes with three swallow-tailed alkyl substituents (benzo[o]bistriphenyleno[2,1,12,11-efghi:2´,1´,12´, 11´-uvabc] ovalene, **3**),[11] because of their triangle-shaped benzenoid graphene unit with the same number of carbons as fullerene C_{60} and their large D_{3h} symmetric disc-shaped core. Furthermore, their straightforward synthesis and functionalization on the periphery with branched alkyl chains allow efficient solution purification and facile device fabrication, while the p-conjugated chromophore with a relatively low number of ‘‘diluting’’ bulky substituents results in close molecular stacking and high mesophase stability over an extremely broad temperature range.

3.2 Synthesis of Triangle-shaped Discotic Graphenes

The synthesis of **3** was done by Dr. Xinliang Feng. The synthetic approach was based on the building block (1,3,5-tris[2´-(4´´-(4´´´-iodophenyl))-phenyl]benzene, Scheme 1), which allowed further functionalization via metal-catalyzed coupling reactions[11-13], followed by the oxidative cyclodehydrogenation reactions to afford the final triangle-shaped discotic graphenes **3a** and **3b** in high yields.

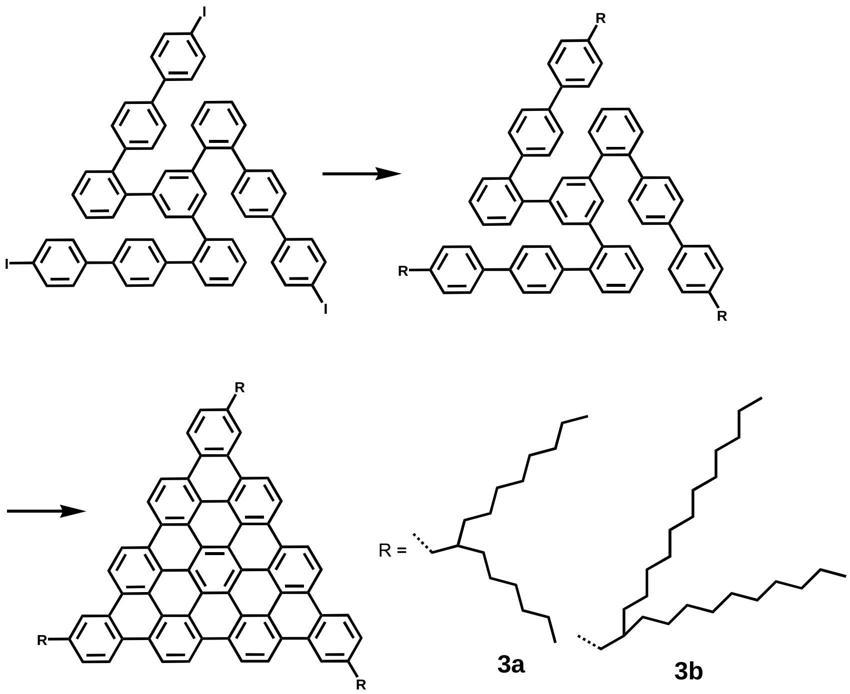

Scheme 1. Synthesis of triangle-shaped discotic graphenes **3**.

3.3 Optical Properties

As shown in Figure 1, the UV-vis spectrum of **3b** in $CHCl_3$ exhibited three types of bands (α, β, p, λmax = 391 nm, ε = 1.48 x 10^5 M^{-1} cm^{-1}) which are typical for aromatic hydrocarbons,[14] and was comparable to the solid state UV-vis spectrum of the parent insoluble compound.[11]

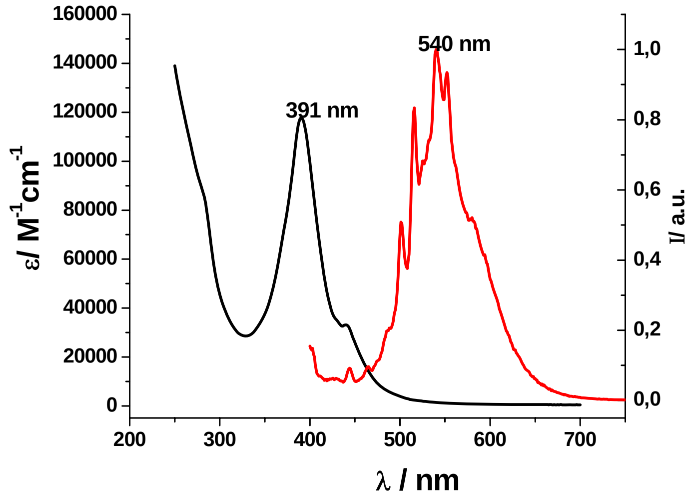

Figure 1. UV-vis absorption (solid line, 1.0 x 10^{-6} M) and fluorescence (dashed line, 1.0 x 10^{-7} M) spectra of **3b** in $CHCl_3$.

As expected, a spin-coated thin film of **3a** revealed a higher absorbance than **3b** at the same film thickness due to higher chromophore concentrations in **3a** (Figure 2). Chromophore concentration is an important parameter for light harvesting in the photovoltaic device.[2b]

The p-band (455 nm) and α-band (not clearly resolvable) for both **3a** and **3b** were bathochromically shifted in the solid state with respect to solution spectra indicating high sensitivity of the p-band and α-band toward aggregation. After annealing the thin films at 120 °C for one hour, the UV-vis spectrum of **3a** did not show apparent differences to the initial spectra (Figure 2). In contrast, the peak intensity for **3b** was markedly enhanced after the same thermal treatment and the corresponding p-band and α-band were further broadened (Figure 2). The intensity increase was attributed to an improved long-range order after annealing.[7d] This annealing effect was only observed for **3b**.

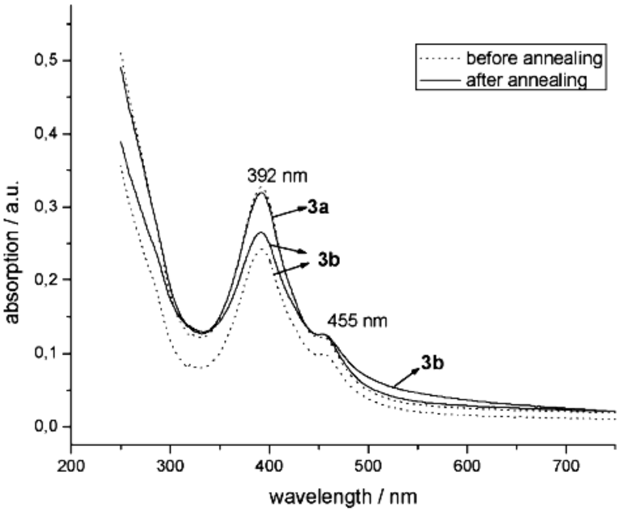

Figure 2. UV-vis absorption spectra of **3a** and **3b** in thin films (thickness of (100±10) nm) before (dotted line) and after annealing at 120 °C (solid line)

3.4 Energy Levels

The design of bulk heterojunction photovoltaic devices requires a consideration of the potential electronic levels of both donor and acceptor components. Cyclic voltammetry (CV) was carried out to obtain the electronic levels of compounds **3a** and **3b** in the solid state. Quasi-reversible oxidation peaks were observed in positive scans (Figure 3). For **3a**, a highest occupied molecular orbital (HOMO) level of -5.1 eV was calculated from the onset values of the oxidation peak (E^{onset}_{ox} = 0.3V versus Fc/Fc$^+$), while **3b** showed the HOMO level at -5.2 eV. With the optical bandgap of 2.3 eV (onset of the p-band in solid state UV-vis spectra), the lowest unoccupied molecular orbitals (LUMOs) of -2.8 eV for **3a** and -2.9 eV for **3b** have been calculated. The determined levels suggested that **3a** and **3b** are suitable donor materials for PDI used in this study which exhibited HOMO and LUMO electronic levels at -5.8 eV and -3.8 eV, respectively.

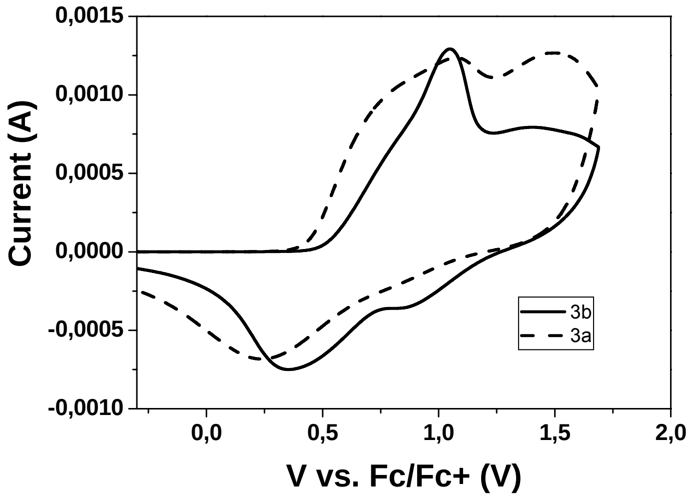

Figure 3. Cyclic voltammetry curve of **3a** and **3b** tested on ITO glass.

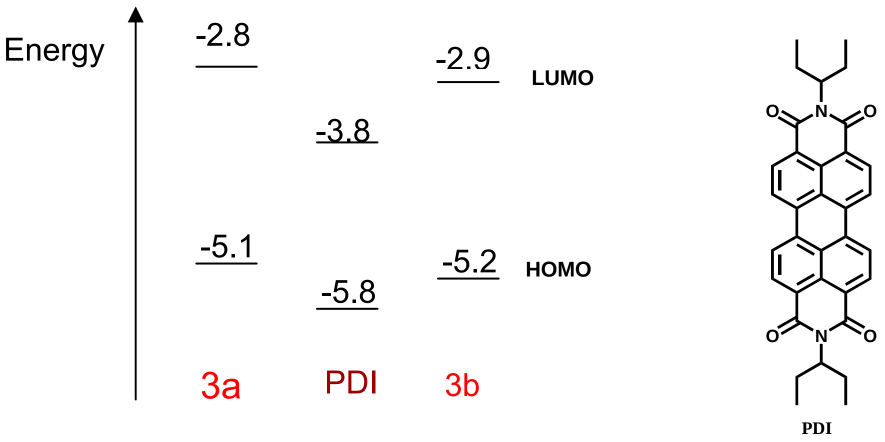

Figure 4. Energy level diagram of PDI and 3a/3b (left); chemical structure of PDI (right).

3.5 Thermotropic Properties

It has been reported that besides the optical properties and electronic levels, the self-organization and molecular packing of the compounds play a key role for the photovoltaic efficiency.[15-18] Therefore, a particular focus was put on the thermotropic properties of both compounds **3a** and **3b**.

The thermal behavior was investigated by using differential scanning calorimetry (DSC) which revealed a phase transition for **3b** at 24 °C (7.4 J g^{-1} during 2nd heating cycle, 45 °C during 1st heating). Compound **3a** did not show any phase transition in the investigated temperature range. Two-dimensional wideangle X-ray scattering (2D-WAXS) measurements on extruded samples[19] gave an insight into the supramolecular organization. Before annealing the scattering patterns of both compounds **3a** and **3b** indicated a characteristic discotic liquid crystalline phase (Figure 5).[4]

Thereby, the molecules were arranged in columnar structures with their disc planes perpendicular to the stacking axis possessing a π-stacking distance *d* of 0.35 nm for both cases, as characterized by the meridional wide-angle reflections (schematic illustration in Figure 5c). The well-aligned columns were organized in a lateral 2D hexagonal array, with an interchain distance a_{hex} = 2.77 nm for **3a** and a_{hex} = 3.49 nm for **3b**. While **3a** did not display any change of the supramolecular arrangement upon thermal treatment (Figure 6), whereby different annealing temperatures have been investigated, compound **3b** exposed a significantly enhanced degree of order, as suggested by much more distinct reflections in the pattern during annealing at 120 °C and after cooling back the sample below the phase transition even to -70 °C (Figure 5a). Especially the wide-angle meridional reflections became more intense and sharp (see comparison of the azimuthal integration, Figure 5b) demonstrating a significant improvement of the intracolumnar packing. The unit cell parameter decreased to a_{hex} = 3.22 nm.

Apparently, annealing above the phase transition observed for **3b** played an important role for the self-organization procedure. In general, self-organization causes two effects: it reduces macroscopic domain boundaries and promotes the formation of a monodomain; the local arrangement of molecules is enhanced. However, compound **3a** did not reveal such behavior due to the absence of a high temperature state with distinct molecular dynamics. Therefore, the improved supramolecular order of **3b** can be explained in terms of longer branched side chains which led to higher molecular dynamics at temperatures above the phase transition and allowed for a reorganization of the molecules into a more favorable packing, which was crucial for the device performance as later discussed.[6b]

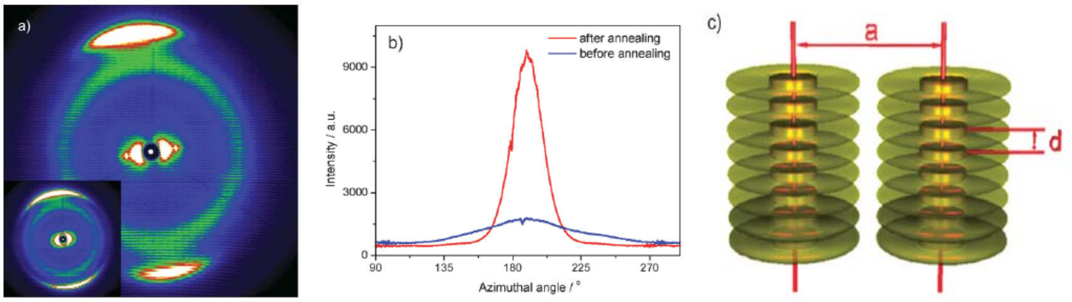

Figure 5. a) 2D-WAXS pattern of **3b** after annealing (inset shows before annealing), b) azimuthal integration of the meridional reflection related to the π-stacking, c) schematic illustration of the columnar organization of **3**.

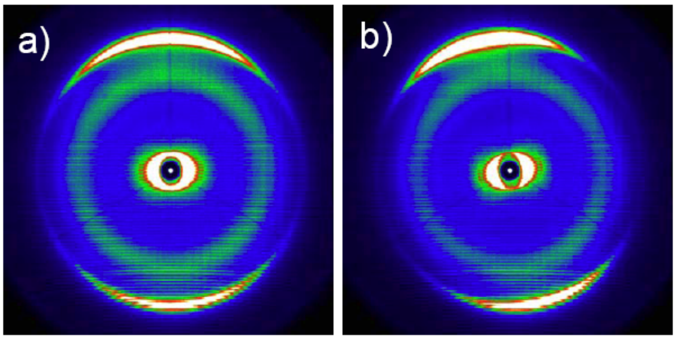

Figure 6. 2D-WAXS pattern of **3a** recorded at 30°C a) before and b) after annealing. Different annealing tempretures have been investigated, but no effect on the order could be observed.

It has to be pointed out that both phases of **3b** have been assigned as liquid crystalline differing only in molecular dynamics. Finally, it should be noted that both compounds did not have an isotropic phase up to 500 °C indicating an extreme liquid crystalline stability. Up to now, such thermal mesophase stability has been only observed for systems with improved helical arrangement in plastic phases.[9] In the present case, the exceptionally broad temperature range of the liquid crystalline phase of both compounds can be related for better packing of molecules and their unique triangle shape of the aromatic core.

3.6 Photovoltaic Device

The influence of the thermotropic behavior of **3a** and **3b** on device properties was further investigated on bulk heterojunction photovoltaics.

The photovoltaic devices consisted of indium tin oxide (ITO)/(**3**+PDI)/Ag. The chloroform solution of **3**/PDI (15mg/mL, ratios of 2:8, 4:6, 5:5, and 6:4) was spin-coated onto ITO substrates which were pre-treated with acetone and isopropyl alcohol in an ultrasonic bath. Before the measurement, the samples were annealed at 120 °C for 1h under a nitrogen atmosphere in order to self-organize the thin films. The highest device efficiency was observed for blends with the ratio of **3**:PDI = 4:6. Interestingly, the same ratio was determined for the best photovoltaics based on discotic HBCs and PDI.[2b]

It is remarkable that the highest external quantum efficiency (EQE) of 19% was achieved at 490nm for the blend containing **3b**, while **3a** showed a lower EQE of 14% (Figure 7a). The difference in performance was attributed to the improved intracolumnar packing of **3b** upon annealing favoring the charge-carrier transport and exciton diffusion length which are both key parameters for device efficiency.[2] This assumption was confirmed in a higher short-circuit current for **3b** which was extracted from the current–voltage (I–V) curve (Figure 7b).

The higher device efficiency of **3b** in comparison to **3a** is quite impressive since **3b** possessed poorer light harvesting (Figure 2) due to a lower chromophore concentration (defined as the ratio of carbon atoms between aromatic core and alkyl side chains). This differs from the phenomenon previously observed in a series of HBCs varying in the length of the attached alkyl side chains from 2-ethyl-hexyl of HBC-$C_{6,2}$, and 2-hexyl-decyl of HBC-$C_{10,6}$, to 2-decyl-tetradecyl of HBC-$C_{14,10}$, where the absorption in a 100 nm thick film decreased from 1.4, to 0.8 to 0.5 and the device efficiency decreased with increasing length of the alkyl substituents in the HBCs.[2b]

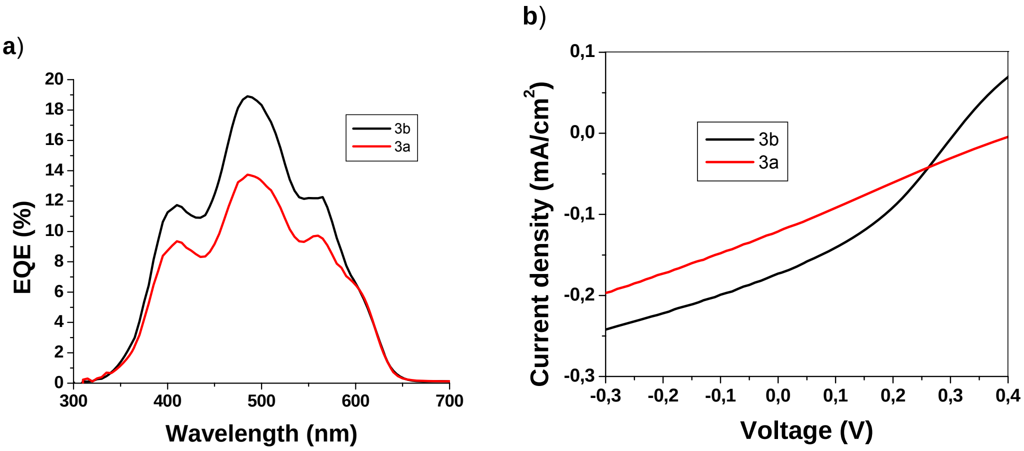

Figure 7. a) EQE plots for ITO/**3b** (black line) and **3a** (red line):PDI (4:6)/Ag device; b) I–V characteristics of 3-based cells under one sun illumination.

3.7 Morphology View

It is well known that the bulk heterojunction morphology is important for the photovoltaic performance.[10] The inspection of the thin layers in the devices consisting of blends of **3a** and **3b**, respectively, and PDI by scanning electron microscopy (SEM) revealed similar top view images. Cross-sectional SEM images, imaged with the substrates tilted 15° to the incident electron beam, were also taken to investigate the internal bulk morphologies of the thin films (Figure 8).

In both cases a ‘homogeneous’ bicontinuous phase was derived from the SEM images across the thickness with cylindrical PDI crystals evenly dispersed within the liquid crystalline matrix of **3a** and **3b**, respectively, from bottom to top of the film. The mixed phase thus resulted in an intimate contact between the donor and the acceptor on a molecular level, which offered a large D/A interface for charge separation. The morphology displayed in both images in Figure 8 is considered to be favorable for the charge transport of holes and electrons in the corresponding separated continuous percolation pathways.

Since films of **3b**:PDI and **3a**:PDI revealed identical mesoscopic morphologies, the performance dissimilarity between **3a** and **3b** in the photovoltaic device can be attributed mainly to the annealing effect for **3b** and the different degree of local order after thermal treatment.

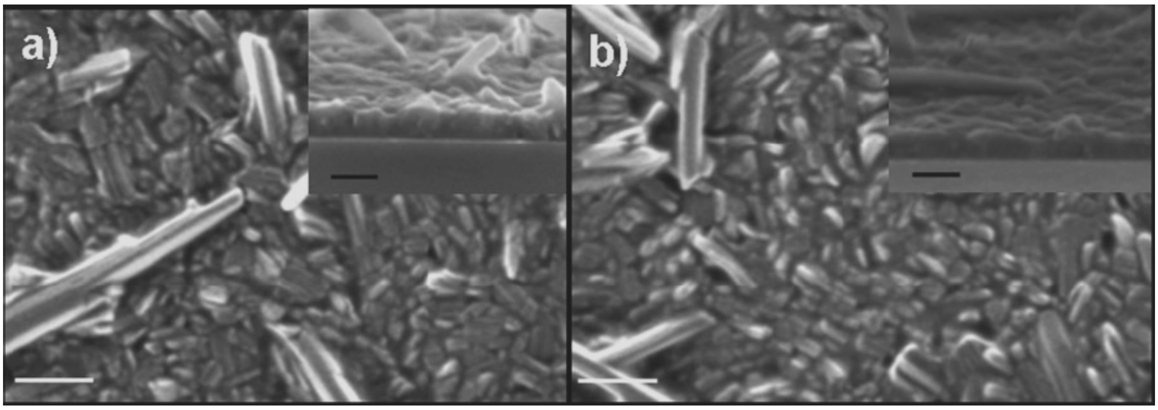

Figure 8. SEM images: top view images (scale bar for 100 nm) and cross-section view (inset, scale bar for 500 nm) of a) **3b**:PDI and b) **3a**:PDI (both in a ratio of 4:6). All films were annealed at 120 °C for 1 h.

3.8 Comparison with the Swallow-tailed HBC Analogues

It has to be stressed that both **3a** and **3b** exhibited a better photovoltaic performance in comparison to the swallow-tailed HBC analogues.

Figure 9 presents the EQE normalized by the chromophore concentration for the previously reported HBCs and compounds **3a** and **3b**.

Interestingly, despite the differences of the HBC derivatives in the thermotropic properties, light harvesting and morphology, the normalized EQE is equal for the three materials. However, this is not the case for **3a** and **3b**. Compound **3a** gave a slightly lower value than the swallow-tailed HBCs, whereby the highest normalized EQE was determined for **3b**. This comparison indicates again the great impact of the self-organization process on the photovoltaic device which was only observed for **3b**.

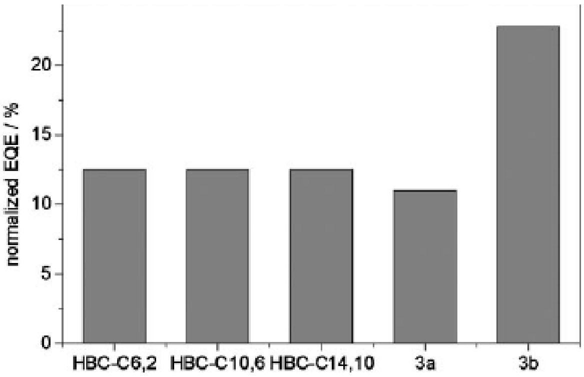

Figure 9. Normalized EQE by the chromophore density for previously reported swallow-tailed HBCs[2b] and compounds **3**. The chromophore density was determined by the ratio between the number of carbon atoms of the aromatic core and the side chains.

3.9 Conclusion

The novel triangle-shaped discotics with swallow alkyl tails (benzo[o]bistriphenyleno[2,1,12,11-efghi:2´,1´,12´, 11´-uvabc] ovalene, **3**), which consist of a high D_{3h} symmetric extended graphene corona, allowed a facile purification, control over the thermotropic properties and finally solution fabrication into efficient photovoltaic devices. Their extremely broad liquid crystalline range resulted from the large aromatic cores permitted self-organization at low processing temperatures.

After the thermal treatment, the supramolecular order in the molecule **3b** with longer branched side chains was improved, while the molecule **3a** with shorter substituents showed no annealing effect, which resulted in the corresponding higher EQE of 19% at 490 nm for the longer branched molecule **3b**. Hence, the higher device efficiency of graphene molecule **3b** with longer alkyl chains is attributed to the improved intracolumnar packing in the molecule upon annealing favoring the charge-carrier transport.

In conclusion, the control over thermotropic properties by molecular design and the substitution pattern of liquid crystalline semiconductors capable to monodomain formation opens an effective route towards optimized organic electronics.

3.10 References

[1] (a) A. M. van de Craats, N. Stutzmann, O. Bunk, M. M. Nielsen, M. Watson, K. Müllen, H. D. Chanzy, H. Sirringhaus, R. H. Friend, *Adv. Mater.* **2003**, *15*, 495; (b) W. Pisula, A. Menon, M. Stepputat, I. Lieberwirth, U. Kolb, A. Tracz, H. Sirringhaus, T. Pakula, K. Müllen, *Adv. Mater.* **2005**, *17*, 684; (c) S. Xiao, J. Tang, T. Beetz, X. Guo, N. Tremblay, T. Siegrist, Y. Zhu, M. Steigerwald, C. Nuckolls, *J. Am. Chem. Soc.* **2006**, *128*, 10700.

[2] (a) L. Schmidt-Mende, A. Fechtenkötter, K. Müllen, E. Moons, R. H. Freind, J. D. MacKenzie, *Science* **2001**, *293*, 1119; (b) J. Li, M. Kastler, W. Pisula, J. W. F. Fobertson, D. Wasserfallen, A. C. Grimsdale, J. Wu, K. Müllen, *Adv. Funct. Mater.* **2007**, *17*, 2528.

[3] F. Jäckel, M. D. Watson, K. Müllen, J. P. Rabe, *Phys. Rev. Lett.* **2004**, *92*, 188303.

[4] (a) J. Wu, W. Pisula, K. Müllen, *Chem. Rev.* **2007**, *107*, 718; (b) S. Laschat, A. Baro, N. Steinke, F. Giesselmann, C. Hagele, G. Scalia, R. Judele, E. Kapatsina, S. Sauer, A. Schreivogel, M. Tosoni, *Angew. Chem. Int. Ed.* **2007**, *46*, 4832; (c) S. Sergeyev, W. Pisula, Y. H. Geerts, *Chem. Soc. Rev.* **2007**, *36*, 1902.

[5] (a) A. R. Murphy, J. M. J. Frechet, *Chem. Rev.* **2007**, *107*, 1066; (b) S. Gunes, H. Neugebauer, N. S. Sariciftci, *Chem. Rev.* **2007**, *107*, 1324.

[6] (a) W. Pisula, M. Kastler, D. Wasserfallen, T. Pakula, K. Müllen, *J. Am. Chem. Soc.* **2004**, *126*, 8074; (b) W. Pisula, M. Kastler, D. Wasserfallen, M. Mondeshki, J. Piris, I. Schnell, K.Müllen, *Chem. Mater.* **2006**, *18*, 3634.

[7] (a) I. Mcculloch, M. Heeney, C. Bailey, K. Genevicius, I. Macdonald, M. Shkunov, D. Sparrowe, S. Tierney, R. Wagner, W. Zhang, M. L. Chabinyc, R. J. Kline, M. D. Mcgehee, M. F. Toney, *Nat. Mater.* **2006**, *5*, 328; (b) B. S. Ong, Y. Wu, P. Liu, S. Gardner, *J. Am. Chem. Soc.* **2004**, *126*, 3378; (c) J. C. Maunoury, J. R. Howse, M. L. Turner, *Adv. Mater.* **2007**, *19*, 805; (d) K. H. Kim, Z. Chi, M. J. Cho, J. I. Jin, M. Y. Cho, S. J. Kim, J. S. Joo, D. H. Choi, *Chem. Mater.* **2007**, *19*, 4925.

[8] (a) M. Funahashi, F. Zhang, N. Tamaoki, *Adv. Mater.* **2007**, *19*, 353; (b) K. Oikawa, H. Monobe, K. Nakayama, T. Kimoto, K. Tsuchiya, B. Heinrich, D. Guillon, Y. Shimizu, M. Yokoyama, *Adv. Mater.* **2007**, *19*, 1864; (c) A. J. J. M. van Breemen, P. T. Herwig, C. H. T. Chlon, J. Sweelssen, H. F. M. Schoo, S. Setayesh, W. M. Hardeman, C. A. Martin, D. M. de Leeuw, J. J. P. Valeton, C. W. M. Bastiaansen, D. J. Broer, A. R. Popa-Merticaru, S. C. J.Meskers, *J. Am. Chem. Soc.* **2006**, *128*, 2336.

[9] Only the plastic crystalline phase was observed over a broad temperature range. Examples see: (a) W. Pisula, Z. Tomovic, M. D.Watson, K. Müllen, J. Kussmann, C. Ochsenfeld, T. Metzroth, J. Gauss, *J. Phys. Chem. B.* **2007**, *111*, 7481; (b) X. Feng, W. Pisula, K. Müllen, *J. Am. Chem. Soc.* **2007**, *129*, 14116; (c) X. Feng,W. Pisula, L. Zhi, M. Takase, K. Müllen, *Angew. Chem.* **2008**, *120*, 1727; *Angew. Chem. Int. Ed.* **2007**, *47*, 1703.

[10] (a) X. Yang, J. Loos, *Macromolecules* **2007**, *40*, 1353; (b) T. Kietzke, R. Y. C. Shin, D. A. M. Egbe, Z. K. Chen, A. Sellinger, *Macromolecules* **2007**, *40*, 4424.

[11] X. Feng, J. Wu, M. Ai, W. Pisula, L. Zhi, J. P. Rabe, K. Müllen, *Angew. Chem.* **2007**, *119*, 3093; *Angew. Chem. Int. Ed.* **2007**, *46*, 3033.

[12] (a) X. Feng, J. Wu, V. Enkelmann, K. Müllen, *Org. Lett.* **2006**, *8*, 1145; (b) X. Feng, W. Pisula, M. Ai, S. Gröper, J. P. Rabe, K. Müllen, *Chem. Mater.* **2008**, *20*, 1191.

[13] S. Huo, *Org. Lett.* **2003**, *5*, 423.

[14] The intensity of the α-band is too low to be detected. However, the β-band at 391nm and the p-band as the shoulder at 440 nm are clearly resolved and show a significant bathochromic shift with respect to the hexa-peri-hexabenzocoronenes (the β-band at 360 nm).

[15] J. Peet, J. Y. Kim, N. E. Coates, W. L. Ma, D. Moses, A. J. Heeger, G. C. Bazan, *Nat. Mater.* **2007**, *6*, 497.

[16] B. C. Thompson, J. M. J. Frechet, *Angew. Chem. Int. Ed.* **2008**, *47*, 58.

[17] M. T. Lloyd, J. E. Anthony, G. G.Malliaras, *Mater. Today* **2007**, *10*, 34.

[18] C. J. Brabec, N. S. Sariciftci, J. C. Hummelen, *Adv. Funct. Mater.* **2001**, *11*, 15.

[19] W. Pisula, Z. Tomovic, C. Simpson, M. Kastler, T. Pakula, K. Müllen, *Chem. Mater.* **2005**, *17*, 4296.

Chapter 4 A Self-organizable Polymer for Photovoltaic Applications

4.1 Introduction

Within all the organic materials, conjugate polymers have been the most important candidates since 1990s after the first bulk-heterojunction polymer solar cells was published by Heeger *et al*.[1] To date, they are still leading the development of the solid-state thin-film organic solar cells with the highest power conversion efficiency up to 7%.[2] Even an efficiency of 7.9% was reported by Solarmer Energy Inc. in the end of 2009.[3]

With kaleidoscopic chemical building blocks, various conjugated polymers can be synthesized. In order to fulfill the requirements of an efficient photovoltaic device, a polymer should have 1) a broad optical absorption ranging into the NIR region for efficient light-harvesting, 2) suitable redox energies allow the polymers to have high enough electron injection driving force to an acceptor material, 3) a self-organization ability which facilitates efficient exciton diffusion and charge transport.

Among all these parameters, the most important factor is the optical absorption property which determines the photon absorption efficiency of the devices. The amount of incoming photons from the sun across the UV, visible and IR regions is about 4%, 51% and 45%[4], respectively. However, typical organic solar cells absorb only a fraction of the visible portion of the solar spectrum. In fact, even the best organic solar cells can absorb and convert only about 1/3 of the total available light utilizing primarily the visible portion of the spectrum. Therefore, the investigation of new polymers which can absorb both visible and near-infrared light becomes more and more important. To realize it, synthesizing donor-acceptor copolymers is the most convenient and efficient pathways. Now, nearly all the best polymers for solar cells contain donor and acceptor moieties. [2]

Besides a broad absorption, a good polymer should also have suitable energy levels. Buckminster-fullerene has been proven to be a desirable n-type material in solar cells. Most of fullerenes compounds have relatively low-lying lowest unoccupied molecular orbital (LUMO) energy level which is thermodynamically favorable to accept electrons from an excited p-type material, e.g. polymers. Moreover, the triply degenerate orbitals from LUMO of fullerene enable it to be reduced easily by up to six electrons, showing its unique stabilization of negative charges.[5] Regarding these intrinsic properties of fullerenes, obviously, for an efficient solar cell, the HOMO and the LUMO energies of polymers should be more positive than those of acceptors in order to guarantee the ready charge transfer.

Besides broad absorption and suitable energies, for an efficient solar cell, a conjugated polymer should also be able to self-organize, which means that it can form a bicontinuous interpenetrating network together with fullerenes in blend films. This highly folded donor-acceptor interface provides excitons with a shorter distance to travel from the exciton generation site to the dissociation point, which increase the charge generation.

Compared to the other two parameters (absorption and energy levels), the self-assembling property of polymers to form ideal morphology in films is the most difficult impact factor to understand. It is critical to design a polymer to realize bicontinuous phase in devices. Therefore, in this thesis, the characterization of a benzo[2,1-b;3,4-b']dithiophene containing conjugated polymer (PBTT) (Figure 2) was demonstrated, with regard to its photovoltaic performance. X-ray diffraction (XRD) measurements revealed that the thermal treatment resulted in an increased crystallinity within the PBTT:[70]PCBM network and subsequent spatial rearrangement in the film. Upon stepwise annealing process, the PBTT-based bulk-heterojunction solar cells showed promising overall conversion efficiency under one sun light illumination, which suggest that the use of self-organizable materials is an efficient approach for high-performance photovoltaic applications.

4.2 Benzodithiophene Building Block

It is known that, the hexyl substituents in P3HT endow the molecule with good solubility. Moreover, the regioregular placement of the alkyl substituents in P3HT minimizes the steric interaction and consequently leads to the ordered lamellar packing and the strong π overlap both in intra- and interchain delocalization.[6] Due to the fact that only one aromatic substitution point available with P3HT, the fused benzodithiophene core has been considered as a building block in semiconducting polymers, in order to maintain the electronic and photonic benefits of the regioregular P3HT, but still allow control of the molecular orbital levels for the polymer.[6,7] With the symmetric nature of benzodithiophene core, it is easy to realize the regioregularity for its polymers by introducing other moiety in even numbers into its monomers. The central benzene core in the fused benzodithiophene core allows the incorporation of functional units (such as solublizing groups), while also maintaining planarity of the two thiophene units. With substituents attached on the central benzene ring (Figure 1), some benzodithiophene-contained polymers have appeared to be good semiconducting donors for organic thin-film transisitors[7,8a] and solar cells[2].

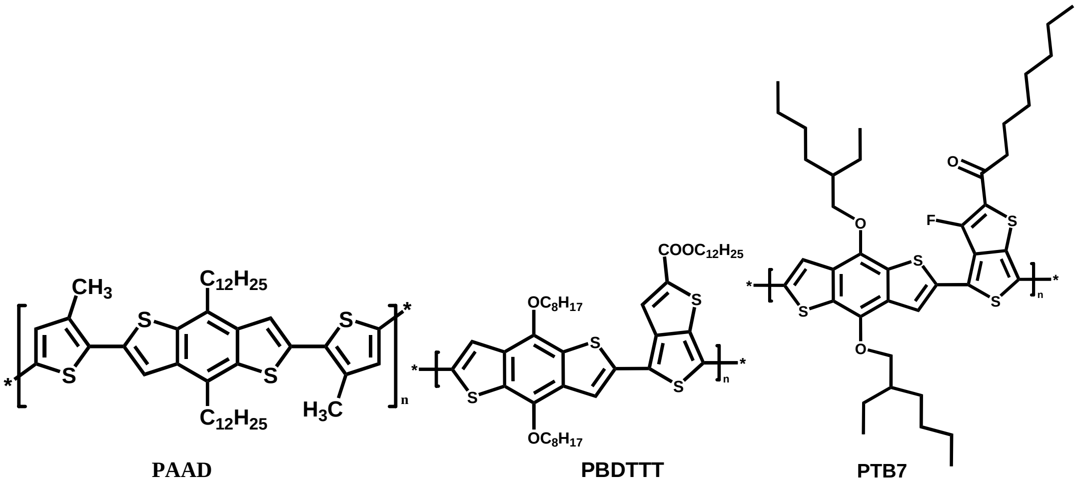

PAAD **PBDTTT** **PTB7**

Figure 1. Structures of some benzodithiophene-contained polymers with substituents attached on the central benzene ring

The introduction of aliphatic groups in the central benzene motif of benzodithiophene can largely improve the solubility of the resulting polymers, however, it weakens the polymer chain-chain interaction. In this chapter, a novel conjugated polymer poly[2,7-(benzo[2,1-b;3,4- b']dithiophene)-*alt*-2,2'-(3,3'-didodecyl-5,5'-bithiophenyl)] (PBTT) (Figure 2), which is a rigid copolymer utilizing an unsubstituted benzodithiophene moiety to enforce self-organization of the polymer chain, will be introduced. Herein, for the first time, to maintain the inter polymer chains interaction, the substituent-free benzodithiophene based copolymer is used as p-type semiconductor for solar cell applications. In this structure, the benzodithiophene moiety affords a free volume for the two side chains (dodecyl) on the thiophenes units, which potentially increases the π-π stacking between polymer backbones. Thus, this polymer demonstrates high charge-carrier mobility of up to 0.5 $cm^2V^{-1}s^{-1}$ on plastic substrates.[8b]

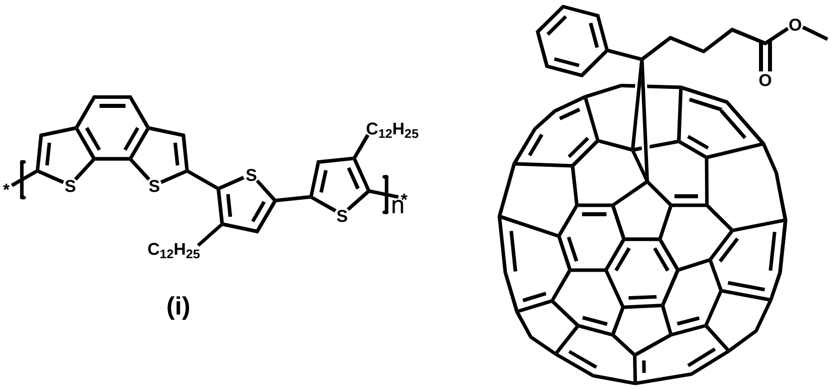

(i)

(ii)

Figure 2. Structures of i) poly[2,7-(benzo[2,1-b;3,4-b']dithiophene)-alt-2,2'-(3,3'-didodecyl-5,5'-bithiophenyl)] (PBTT), ii) [6,6]-phenyl-C_{71}-butyric acid methyl ester ([70]PCBM).

4.3 Synthesis of PBTT

The PBTT polymer, synthesized by Dr. Ralph Rieger, has a number average molecular weight Mn of 27,000 g/mol, a weight average molecular weight Mw of 49,000 g/mol, and polydispersity (PDI) of 1.6. Scheme 1 shows the synthetic route:

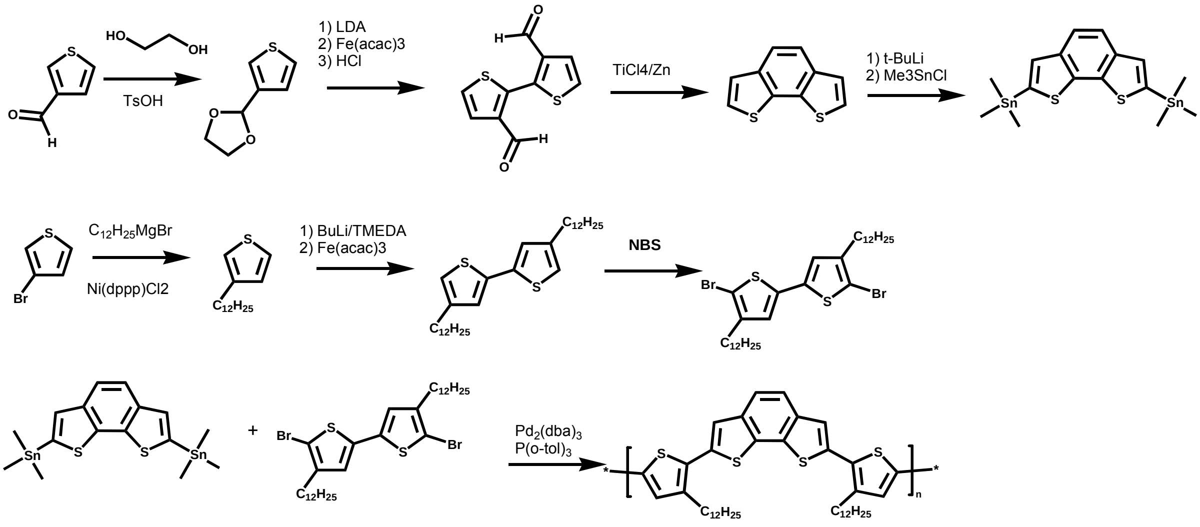

Scheme 1. Synthesis of poly[2,7-(benzo[2,1-b;3,4-b']dithiophene)-alt-2,2'-(3,3'-didodecyl-5,5'-bithiophenyl)] (PBTT)

As described in Scheme 1, the polymer PBTT was synthesized under the Stille coupling condition. The reaction was processed in dichlorobenzene under argon for three days, followed by product purification through precipitation in methanol for several times. For highly efficient organic thin-film photovoltaic cells, the purity of organic material is an essential factor, because the impurities in organic materials act as trapping sites of generated carriers.[9]

Compared with those alkyl substituted benzodithiphene containing polymers, an increased solubility with comparable packing tendency is expected when the alkyl chains are moved from the benzodithiophene unit to the dithiophene moiety. The solubility of PBTT in dichlorobenzene is significantly higher (> 20 mg mL^{-1}), which renders PBTT an extraordinary film-forming property.

4.4 Optical Properties

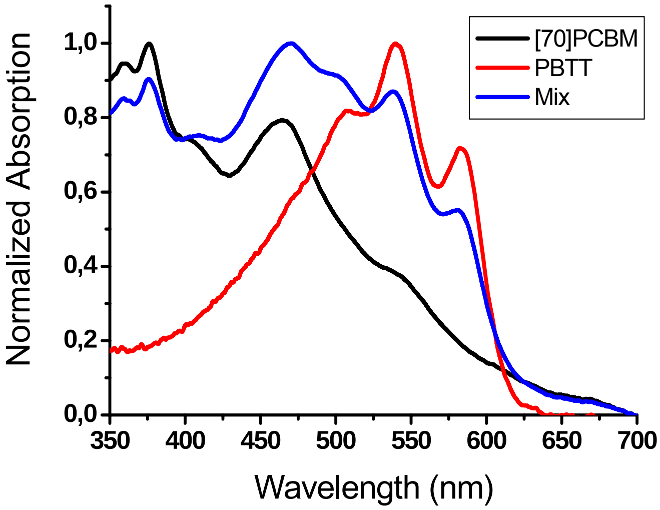

Figure 3. Absorption spectra of the dichlorobenzene solution of [70]PCBM (black line), PBTT (red line), their 2:1 mixture (blue line).

As shown in Figure 3, a maximum absorption of PBTT in a dichlorobenzene solution occurs at 540 nm. The absorption of the solution mixture of PBTT and [6,6]-phenyl-C_{71}-butyric acid methyl ester ([70]PCBM) overlaps with nearly the whole visible region from 350 to 650 nm, which renders the blend as a good light absorber for highly efficient photovoltaic devices.

4.5 Energy Level Matching

The potential applicability of PBTT as a donor material in solar cells was confirmed by determining the frontier molecular orbital energy levels by cyclic voltammetry (CV) measurements. A thin film on an ITO substrate was tested in a three-electrode system, which included an indium tin oxide (ITO) glass, a silver quasi-reference electrode (AgQRE, calibrated against the Fc/Fc+ redox couple) and a Pt counter electrode. A highest occupied molecular orbital (HOMO) level of -5.2 eV was calculated from the onset values of the oxidation peak (E^{onset}_{ox} = 0.4V versus Fc/Fc^{+}) (Figure 4). The HOMO energy level of PBTT is lower than that of polythiophenes (e.g. -5.1 eV for P3HT) [10], which implies an improved air stability under operation due to the reduced ionization potential of PBTT. With the optical bandgap of 2.0 eV evaluated from the onset of the absorption spectrum, the lowest unoccupied molecular orbital (LUMO) level was estimated to be -3.2 eV. Therefore, [60]PCBM with an experimentally determined LUMO level of -4.1 eV and a HOMO level of -6.1 eV, or [70]PCBM with a LUMO level of -4.3 eV and a HOMO level of -6.1 eV, was chosen as acceptor. In the PBTT/[70]PCBM pair, a 0.9 eV offset of HOMO levels and a 1.1 eV LUMO level difference support an efficient hole migration from [70]PCBM excited states to PBTT as well as a favorable electron transfer from PBTT to [70]PCBM. [60]PCBM meets the energy level requirement when matched with PBTT as well.

As it is known that the V_{OC} value can be estimated from the LUMO level of PCBM and the HOMO level of the polymer. Empirically, the V_{OC} of the devices can be calculated by the following equation:

$$V_{OC} \approx \left|E_{HOMO}^{Polymer}\right| - \left|E_{LUMO}^{PCBM}\right| - 0.3V$$

where the constant 0.3 V represents the lost energy during the photoinduced charge-generation process. Based on this, the open-circuit voltage of PBTT:[70]PCBM containing solar cells can be estimated to be around 0.6 V. The experimental value of V_{OC} in PBTT-based cells is consistent with this theoretical one, indicating a good donor-acceptor interface in the devices.

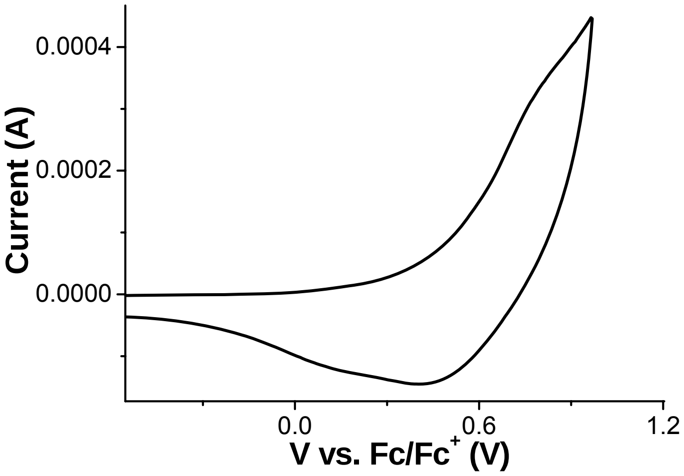

Figure 4. Cyclic voltammetry curve of PBTT tested on ITO glass.

4.6 X-ray Diffraction (XRD) Measurements on the Film Morphology

In bulk heterojunction solar cells, the overall conversion efficiency is strongly related to the interpenetrating nano-scale network morphology of the polymer and fullerene blend.[11] In addition to other parameters, such as choice of solvents, D:A ratio, casting methods, and solution concentrations, the chosen thermal annealing procedure has a significant influence on the film morphology.

Here, the annealing effect was monitored by X-ray diffraction (XRD) measurements through which the related lattice constant d can be calculated using Bragg's law as shown in the following equation:

$$2d \sin\theta = n\lambda \qquad (1)$$

where $\lambda = 0.154$ nm is the wavelength of incident beam, n is the interference order, 2θ is the angle between incident and scattered X-ray wave vectors, and d is the spacing between the planes in the atomic lattice.

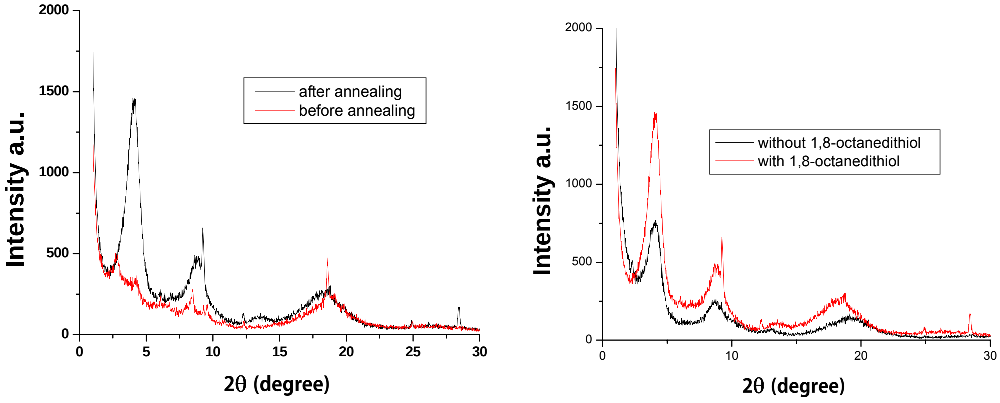

a) b)

Figure 5. a) Film X-ray pictures of film cast on silicon wafer from *o*-dichlorobenzene solution of PBTT:[70]PCBM (1:2) with 1,8-octanedithiol: at room temperature (red); annealed at 120 °C for 14 min (black). b) Film X-ray pictures of films cast on silicon wafer from *o*-dichlorobenzene solution of PBTT:[70]PCBM (1:2) with (red) or without (black)1,8-octanedithiol, both films were annealed at 120 °C for 14 min.

Figure 5 displays the XRD results of the PBTT:[70]PCBM (1:2) blend film before and after heating. An increase in the crystallinity of PBTT can be clearly seen in the XRD spectra. The annealed sample shows an increased intensity in the peak at $2\theta = 4.14$ degrees which corresponds to the lamellar spacing between polymer chains. According to (1), d = 2.07 nm was calculated. In the case of the untreated sample, only very weak diffraction peaks were recorded. This result indicates that a spatial rearrangement of the polymer chains leads to a stronger inter-chain interaction upon heat treatment. The increased crystallinity within the network and subsequent spatial rearrangement in the film indicates that the thermal annealing process should have a dramatic influence on the photovoltaic performance by facilitating charge transport to the electrodes.[11b]

4.7 Solar Cell Device Fabrication and Performance

4.7.1 Morphology Control

It is clear that there are immense factors, intrinsically and extrinsically, affecting the morphology of the active layer.[12] Intrinsically, it concerns properties that are inherent to the polymer and the fullerene as well as the fundamental interaction parameters between the donor and acceptor materials. Extrinsically, it includes all the external influences associated with device fabrication, such as solvent choice, solution concentration of the D/A blend, deposition technique, solvent evaporation rate, as well as thermal annealing and solvent annealing.

4.7.1.1 D/A Ratio

The photovoltaic cells were fabricated in the structure of ITO/PEDOT-PSS/active layer/Ag. The patterned ITO substrates were first cleaned with acetone and isopropyl alcohol in an ultrasonic bath, followed by a cleaning treatment for 10 min with oxygen plasma. Subsequently, a conducting layer of PEDOT:PSS (Clevios P) was spin-cast (5000 rpm) with thickness about 40 nm from aqueous solution. The substrates were dried at 150 °C for 10min in air, and then moved into a glove-box for spin-casting of the photoactive layer. In the case that the D/A ratio is 1:2, the dichlorobenzene solution comprising PBTT (8 mg/mL) and [70]PCBM (16 mg/mL), with 1,8-octanedithiol (24 mg/mL) as the processing additive to control the film morphology of bulk-heterojunction materials in bulk-heterojunction solar cells, was then spin-cast at 700rpm on top of the PEDOT:PSS layer. The 1,8-octanedithiol does not react with either the polymer PBTT or the fullerene [70]PCBM, it functions as processing additive. More details about processing additives will be included in the following section 4.7.1.2. A silver layer (ca. 100 nm) was subsequently evaporated through a mask onto the surface to form the cathode.

The active layers were fabricated from the dichlorobenzene solutions of PBTT and [70]PCBM blend in different weight ratios of 1:1, 1:2 and 1:3, with or without 1,8-octanedithiol (24 mg/mL) as the processing additive.[13] The best performance was obtained from the devices in a D:A ratio of 1:2 with 1,8-octanedithiol included (Table 1). Since the devices show efficiency improvement at higher fullerene ratio (1:2) in comparison to the optimum ratio near 1:1 in some systems like P3HT:PCBM, it is likely that in this system [70]PCBM intercalates between the side chains of PBTT.[14]

Table 1. Photovoltaic performance of devices in different D:A ratios with or without 1,8-octanedithiol

D:A[a]	**Isc (mA/cm^2)**[b]	**Voc (V)**[b]	**FF**[b]	**Efficiency (%)**[b]
1:1	4.25	0.41	0.30	0.54
1:1 + 1,8-octanedithiol	5.60	0.45	0.31	0.81
1:2	5.05	0.66	0.40	1.39
1:2 + 1,8-octanedithiol	8.53	0.67	0.46	2.68
1:3	5.86	0.59	0.36	1.27
1:3 + 1,8-octanedithiol	7.61	0.68	0.43	2.27

[a] D:A equals to PBTT:[70]PCBM in weight ratio, [b] the devices were tested under AM1.5 solar simulator.

Figure 6 shows the UV-vis absorption spectra of blend of polymer/[70]PCBM in different ratios in dichlorobenzene solution. Among them, D/A ratio of 1:2 showed to have the broader absorption spectrum coverage compared to those of 1:1 and 1:3 blends, which fits well with the observation that the D/A ratio of 1:2 gave the best photovoltaic performance.

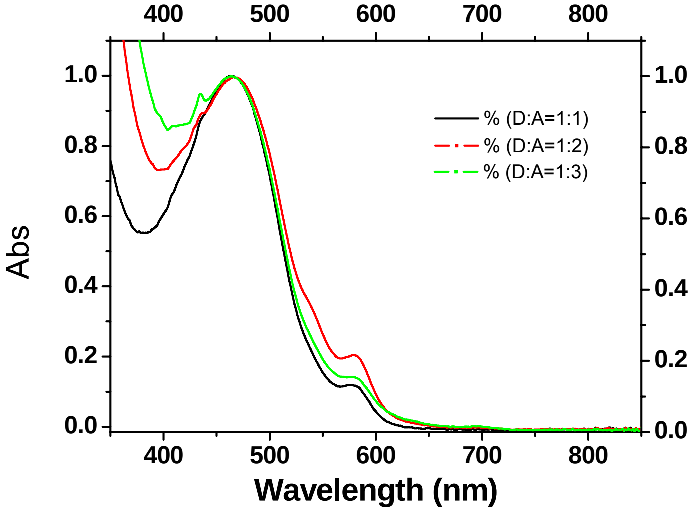

Figure 6. UV-vis absorption spectra of blend of polymer: [70]PCBM in different ratios in dichlorobenzene solution

4.7.1.2 Processing Additive

The processing additives have been believed to be able to improve the cell performance through altering the bulk-heterojunction morphology.[13] There are two criteria for processing additives introduced to control the morphology of BHJ materials for use in solar cells: (i) selective (differential) solubility of the fullerene component and (ii) higher boiling point than the host solvent.[13]

Due to the selective dissolution effect of the processing additive of fullerene, PCBM is readily dissolved in the additive, whereas the polymer is not soluble in it. Thus, it is believed that during the process of liquid-liquid phase separation and drying there are three separate phases formed: a fullerene-processing additive phase, a polymer aggregate phase, and a polymer-fullerene phase.[13] Furthermore, because of the higher boiling point of the processing additive than that of the host solvent (dichlorobenzene), the PCBM is inclined to remain in solution (during the drying process) longer than the polymer. This facilitates the control over the phase separation and the resulting blend morphology.[13]

In the PBTT/[70]PCBM cells, two processing additives were tried, namely, 1,8-octanedithiol and 1,8-dibromooctane. The additive of 1,8-octanedithiol improved the cell performance in all aspects of Isc, Voc and ff, leading to an efficiency increase from 1.39% to 2.68%, while 1,8-dibromooctane decreased the cell efficiency to 0.81% (Table 2 and Figure 7) .

Table 2. Photovoltaic performances of the BHJ polymer solar cells comprised of polybenzodithiophene /[70]PCBM fabricated with various processing additives

Additives	**Isc (mA/cm^2)**	**Voc (V)**	**FF**	**Efficiency (%)**
1,8-octanedithiol	8.53	0.67	0.46	2.68
none	5.05	0.66	0.40	1.39
1,8-diiodooctane	5.60	0.45	0.31	0.81

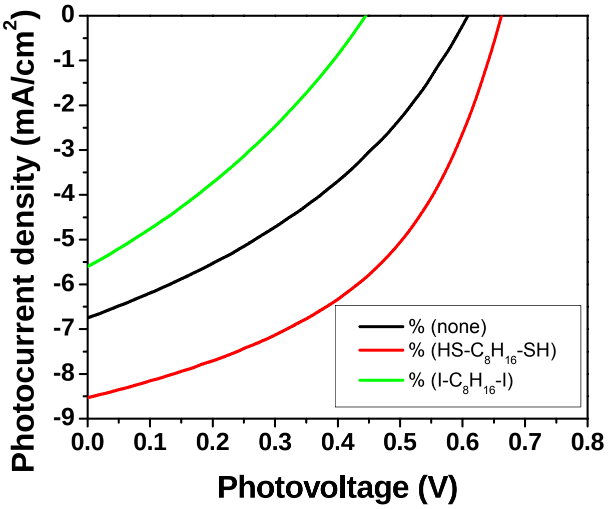

Figure 7. Current-voltage characteristics of polybenzodithiophene / [70]PCBM composite films with various additives: (a) 1,8-octanedithiol (red), (b) none (black), (c) 1,8-diiodooctane (green)

The AFM topography (Figure 8) shows that the additive 1,8-octanedithiol provides the film with a better phase separation and a fine domain size, while 1,8-diiodooctane causes a much too large domain size with a negative effect. From their morphology difference of these three PBTT-based solar cells (without additives, with 1,8-octanedithiol and with 1,8-diiodooctane), their various photovoltaic performance can be expected. Obviously, using additives is an alternative method to control phase-separation of donor/acceptor layers in the solar cell devices. And in case of PBTT-based solar cells, the thiol additive gave the best results.

Compared with the iodide additives, the thiol compounds have similar molecular structure. However, in the solid form, there is hydrogen-bonding between individual thiol groups, and the main cohesive force between the highly polarisable divalent sulphur centers is van der Waals interaction. Additionally, due to the large electronegativity difference between sulfur and iodide, thiols have a higher dipole moment compared to the corresponding iodide compound. Therefore, with the help of a higher dipole and affinity with sulfur atoms, 1,8-octanedithiol can help PBTT to better self-organize and separate in the D/A blend.

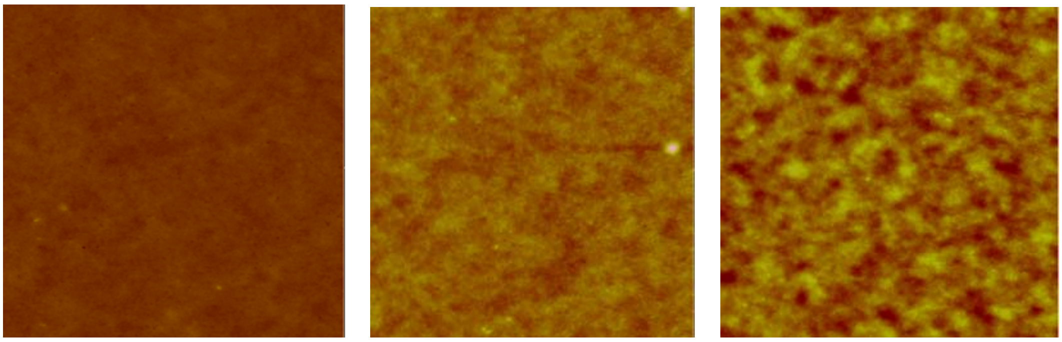

Figure 8. AFM topography of films cast from polybenzodithiophene / [70]PCBM (a) without additives, (b) with 1,8-octanedithiol and (c) with 1,8-diiodooctane

The trial of using other addtives, such as 2’2-thiodiethanethiol and 1,4,7-trithiacyclononane, resulted in the decrease of the cell efficiency.

The impact of processing additives can also be observed in the XRD data of PBTT:[70]PCBM (1:2) films with or without processing additive, where increased intensity in the sample with 1,8-octanedithiol included is shown (Figure 6b).

4.7.1.3 Annealing Effect

Thermal annealing, first reported by Padinger *et al.*[15], is the most commonly used technique to optimize the morphology of the blend film. The function of the heating (up to a temperature higher than the glass temperature T_g of polymer), for example, in P3HT/PCBM system, is believed to allow the polymer chains to reorganize and the fullerene molecules to freely diffuse into the composite and reorder in a more thermodynamically favorable way.[16a] The annealing temperature, annealing time and annealing process have to be carefully controlled to obtain the optimum effect.

At the very beginning, it was found that the pre-annealing (thermo-treatment of the device before the top electrode evaporation) did not improve the cell performance. But then, the post-annealing (thermo-treatment of the device after the top electrode evaporation) was tried and found to be an effective way to improve the overall efficiency. A so-called confinement effect accounts for this difference in performance and tends to reduce the length scale and the degree of phase segregation.[16b]

The post-deposition annealing process was carried out on the same sample every two minutes in a stepwise fashion, resulting in a dramatically enhanced device performance with an increase in the open-circuit voltage (V_{OC}), short-circuit current (I_{SC}) and fill factor (FF) as well as a twofold increase in power-conversion efficiency to 2.68% (Figure 9). After two minutes of annealing at 120 °C, an increase in the V_{OC} from 0.46 V to 0.68 V was observed, which believably indicates the improvement of the donor/acceptor interface dipole moment.[17] An enhancement in the values of the I_{SC} and the FF, 6.94 to 7.61 mA/cm^2 and 0.31 to 0.43, respectively, was also noted. Considering the fact that the improvement comes from the device upon heating process, the improved Isc and FF is obviously due to the film morphology tuning which favors the exciton generation, diffusion and dissociation.[11b] Furthermore, the increased Voc, Isc and FF resulted in a power-conversion efficiency boosted from 1.0% to 2.3%. Among the reported polymer-fullerene solar cells, it is striking that a short annealing time of 2 minutes can improve the cell efficiency so much. Further step by step annealing every two minutes resulted in a gradually enhanced I_{SC} but not a significant change in V_{OC} and FF. These data correspond to a slowly increased overall efficiency with the highest value of 2.7% after a total thermal treatment period of 14 minutes, with a short-circuit current I_{SC} of 8.53 mA/cm^2, open-circuit voltage V_{OC} of 0.67 V and a fill factor FF of 0.46. In addition, it should be noted that the experimentally obtained V_{OC} value of

0.68 V fits well with the expected theoretical value which is in the range of 0.6-0.7 V.[18] Continued thermal treatment after this fourteen-minute period resulted in a trend toward slightly decreasing I_{SC} and FF values, while the V_{OC} value remain unchanged; thus, the same trend in overall efficiency is observed. It is likely a result of phase segregation in a larger than optimal length scale.[12]

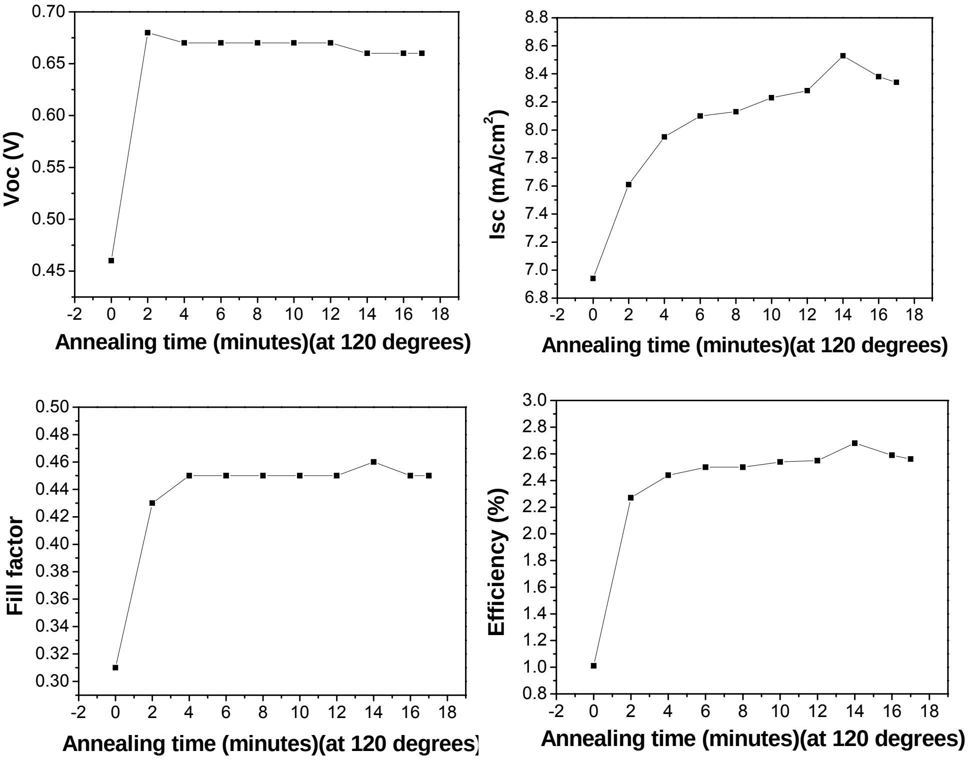

Figure 9. Effect of annealing on PBTT/[70]PCBM (with 1,8-octanedithiol) cell performance

It should be noted that at the beginning of our study on PBTT-based solar cells, [60]PCBM was chosen as the acceptor due to its similar electronic properties to [70]PCBM[19]. The PBTT/[60]PCBM cells (with 1,8-octanedithiol) with D/A ratio of 1:2, showed in the similar way as that of PBTT/[70]PCBM (with 1,8-octanedithiol) an efficiency improvement after a stepwise annealing process (Figure 10). However, the PBTT/[60]PCBM cells gave an overall efficiency of 1.2%, with a short-circuit current of only 4.7 mA/cm^2, around half of those in the PBTT/[70]PCBM cells. The main reason for the efficiency difference is most likely due to the higher absorption coefficients of [70]PCBM in the visible region.[20]

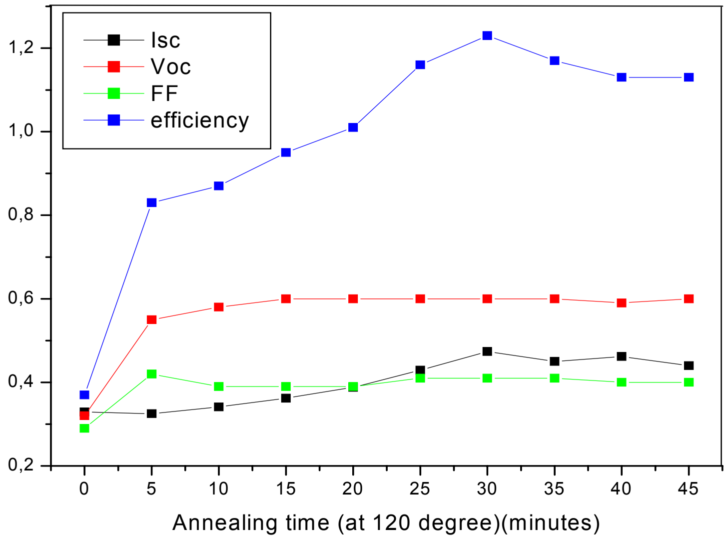

Figure 10. Effect of annealing time on Polymer/[60]PCBM photovoltaic performance

4.7.1.3.1 Annealing Effect in the Aspect of AFM Topography

In order to elucidate the observation that the annealing process improved the device performance in these cells, we first investigated the AFM topography of films cast from PBTT/[70]PCBM before and after the thermal treatment (Figure 11). In good agreement with the XRD results, a finer domain size and better phase-segregated bulk-heterojunction morphology are formed in the blend film (b) due to PBTT's enhanced aggregation properties. The morphology in film (b) is believed to be favorable for the charge transport of holes and electrons in the corresponding separated continuous percolation pathways.[21]

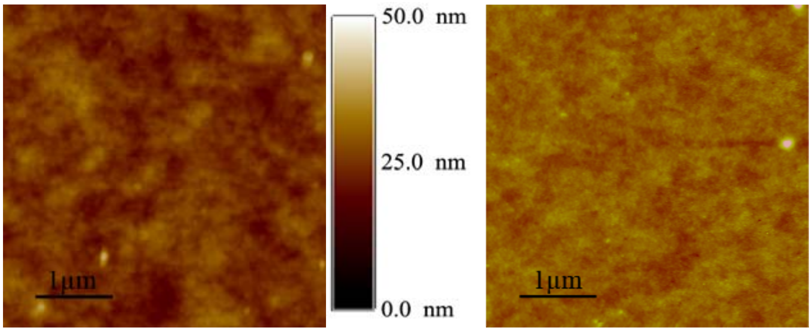

a) b)

Figure 11. AFM topography of films cast from PBTT / [70]PCBM (with 1,8-octanedithiol) a) as cast, b) annealed

4.7.1.3.2 Annealing Effect in the Aspect of Shunt Resistance

Another approach to investigate the reasons for the enhanced efficiency after thermal treatment of these devices is to observe the change of shunt resistance or series resistance in the device upon heating.[22]

Generally, a model (Figure 12), which is electrically equivalent and based on discrete electrical components, is used to understand the electronic behavior of a solar cell.[23] To mimic the situation in a practical solar cell, normally a shunt resistance (R_{SH}) and a series resistance (R_S) component are added to the model. The shunt resistance R_{SH} is due to the recombination of charge carriers near the dissociation site (e.g. D/A interface), while the series resistance R_S considers conductivity (i.e. mobility of the specific charge carrier in the respective transport medium).

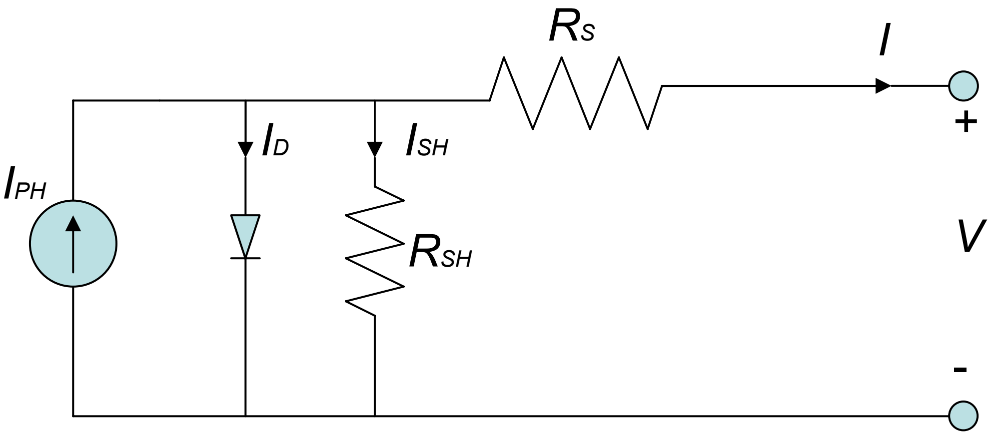

Figure 12. The equivalent circuit of a solar cell. The circuit consists of the following ideal components: A current source I_{PH} that considers the light-generated current, a diode that accounts for the nonlinear voltage dependence and a shunt as well as a series resistor. The current arrows point into the direction the holes flow – according to the standard in electronics. The current I is negative if V > Voc and it flows “into” the device – otherwise it is positive.

From the equivalent circuit it is evident that the current produced by the solar cell (I) is equal to that produced by the current source (I_{PH}), minus that which flows through the diode (I_D), minus that which flows through the shunt resistor (I_{SH}):

$$I = I_{PH} - I_D - I_{SH} \tag{2}$$

where I is the output current, I_{PH} is the photogenerated current, I_D is the diode current and I_{SH} is the shunt current.

Since
$$V_j = V + I R_S \tag{3}$$

where V_j is the voltage across both diode and resistor R_{SH}, V is the voltage across the output terminals, I is the output current and R_S is the series resistance.

By the Shockley diode equation,

$$I_D = I_0\left\{\exp\left[\frac{qV_j}{nkT}\right]-1\right\} = I_0\left\{\exp\left[\frac{q(V+IRs)}{nkT}\right]-1\right\} \qquad (4)$$

where I_0 is the dark current, q is the electron charge, n is the diode ideality factor, k is Boltzmann's constant and T is the absolute temperature.

By Ohm' Law, $$I_{SH} = \frac{V_j}{R_{SH}} \qquad (5)$$

So, the current density/voltage characteristics can be described by the following equation:

$$I = I_{PH} - I_D - I_{SH} = I_{PH} - I_0\left\{\exp\left[\frac{q(V+IRs)}{nkT}\right]-1\right\} - \frac{V+IRs}{R_{SH}} \qquad (6)$$

Define $I = 0$,

$$I_{PH} = I_0\left\{\exp\left[\frac{qV}{nkT}\right]-1\right\} - \frac{V}{R_{SH}} \qquad (7)$$

Therefore, when V is close to 0 V, the value of R_{SH} can be roughly derived by taking the inverse slope around 0 V, e.g. $R_{SH} \approx (\frac{V_{when \approx 0}}{I})$ (Figure 13). Here, the current source generates current I_{PH} upon light irradiation. I_{PH} thus should correspond to the number of dissociated excitons as well as the number of free electron/hole pairs immediately after generation and before any recombination happen. According to this, the shunt resistor R_{SH} could be due to recombination of charge carriers near to the dissociation site (e.g. D/A interface).

Using the construction of equivalent circuit of a solar cell in Figure 12 and Kirchoff's laws for current knots and voltage loops, the following relation can be formulated:

$$(I_{PH} - I_D - I)R_{SH} = I_{SH}R_{SH} = V + IR_S \qquad (8)$$

Therefore, $R_S = \frac{V - I_{SH} R_{SH}}{I}$ (9)

Obviously, if $R_{SH} \approx \infty\,\Omega$, then I_{SH} should be close to 0 A, then R_S can be estimated from the (inverse) slope at a positive voltage > Voc where the I-V curves becomes linear and I ≈ 0 A, e.g. $R_S \approx (\frac{V}{I_{when \approx 0}})$ (Figure 13). The series resistor R_S considers conductivity i.e. mobility of the specific charge carrier in the respective transport medium.

So that, in a current-voltage curve of a solar cell, the R_{SH} and R_S are defined by the slopes of the I-V curve at $I = 0$ and at $V = 0$, respectively (Figure 13).[24]

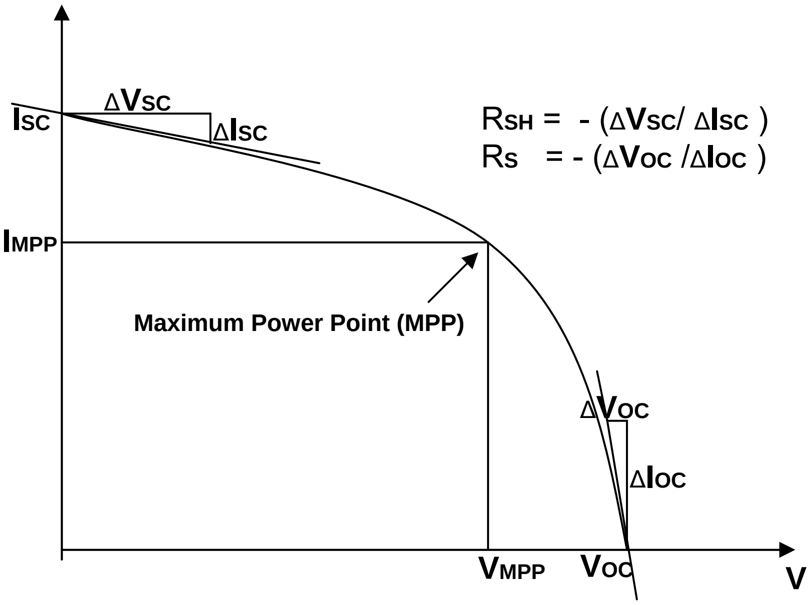

Figure 13. R_{SH} and R_S in the I-V curve of a solar cell

Based on the I-V curves before and after the thermal treatment (Figure 14), we determined that the shunt resistance increases from an initial value of R_{SH} = 94 Ω cm^2 to R_{SH} = 288 Ω cm^2 after annealing at 120 °C, while R_S was observed to be similar before and after annealing.

According to the equation 6, when $R_{SH} \approx \infty\ \Omega$ and $R_S \approx 0\ \Omega$, the IV characteristic of the diode is equal to the IV characteristic of the entire cell and I is close to I_{PH}. Therefore, in an efficient cell, series resistance is expected to be as small and shunt resistance to be as large as possible. As shunt resistances are believed to be related to leakage current in the solar cells[25], the higher shunt resistance observed for the annealed cells suggests lower leakage current than in the case of the non-annealed cells. In an ideal system, a reduction in recombination rate should have resulted in a decrease in leakage current and, hence, an increase in shunt resistance. This augmented shunt resistance most likely indicates less recombination of charge carriers near the donor/acceptor interface in the bulk heterojunction films after thermal annealing and hence an increased power conversion efficiency of the devices.

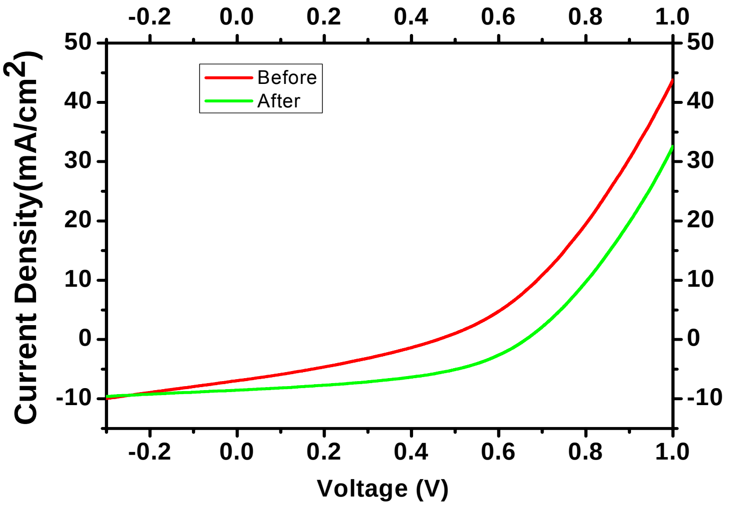

Figure 14. The I-V curves of PBTT / [70]PCBM (with 1,8-octanedithiol) cells before and after annealing.

4.7.2 PBTT / [70]PCBM Cell Performance

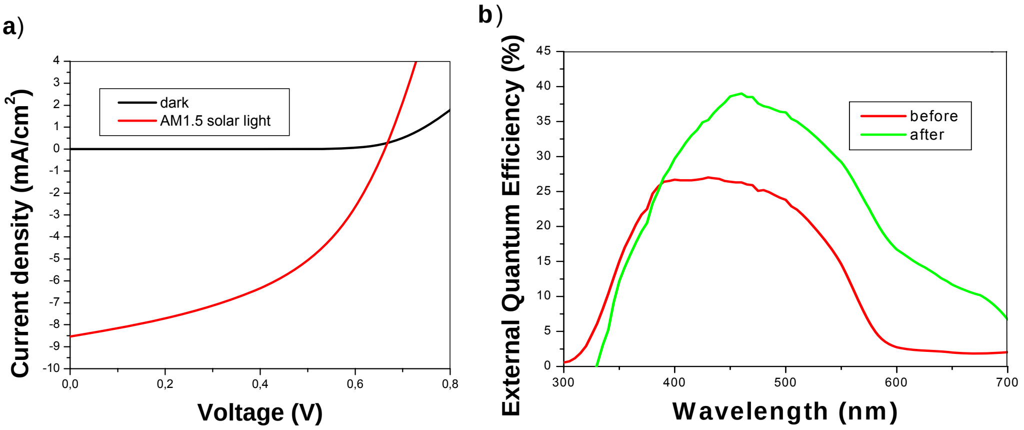

Figure 15. (a) Current density- voltage curve of photovoltaic devices of ITO/PEDOT-PSS/ PBTT / [70]PCBM (1 : 2) with 1,8-octanedithiol /Ag under AM1.5 simulated solar illumination of 1000 W/m^2; (b) External quantum efficiency-wavelength curves of cells before/after annealing.

As shown in Figure 15a, upon stepwise annealing, the PBTT/[70]PCBM cells gave an efficiency of 2.68% under AM1.5 simulated solar illumination of 1000 W/m^2, with a short-circuit current I_{SC} of 8.53 mA/cm^2, an open-circuit voltage V_{OC} of 0.67 V and a fill factor FF of 0.46. Notably, a large increase in terms of External Quantum Efficiency (EQE) for a broad spectral range was achieved upon annealing (Figure 15b). The significant improvement of the EQE value from 27% to 39% indicates an augmented conversion of harvested photons into harvested charges across the composite absorption spectrum. This enhanced EQE is attributed to two aspects: an improvement in the charge transport property and an increased absorption in the active layer, which is induced by the spatial rearrangement of the polymer chains.[22]

4.7.3 PDI as Acceptor

Perylenediimide (PDI)(structure see Chapter 3), with a LUMO level of -3.8 eV and a HOMO level of -5.8 eV, was also tried as acceptor under the consideration of its matched energy level with PBTT. Since the LUMO level of PBTT is -3.2 eV and its HOMO level is located at -5.2 eV, energetically, the 0.6 eV offset of HOMO levels and the 0.6 eV LUMO level difference in the PBTT/PDI pair support the hole migration from PDI excited states to PBTT as well as a favorable electron transfer from PBTT to PDI.

The successful application of PDI as an acceptor was reported when it was matched with a polycarbazole in a BHJ cell in which the absorption of the D/A blend presented a better spectral overlap with the solar irradiation than that of the blend of polycarbazole with the acceptor PCBM did.[26a] Thus, it was expected that PDI's better light absorption ability in the visible region compared to fullerene derivatives could make the cells more efficient.

The devices were fabricated from the dichlorobenzene solutions of PBTT and PDI blended in different ratios of 1:1, 1:2 and 2:1 with top electrode of 100nm Ag. However, during the spin-coating procedure, it was found that the film forming was not good and the film appeared to be highly ragged even seen by the naked eye. Neither the alteration of the active layer film thickness nor the modification of dissolving the D/A blend could improve the film property after the spin-coating. The unfavorable film forming behavior of PBTT/PDI blend is probably due to that PBTT could not suppress the strong aggregation as well as crystallization of PDI. And many PDI clusters were formed in the film. However, only the PDI molecules which are in contact with PBTT can have a charge transfer because of the existence of a complementary electron donor phase. And the existence of the poor contacts between the ITO substrates and PBTT/PDI films in the inhomogeneous film will possibly result in an increase of series resistance. Moreover, the uneven distribution of the two components will enhance the chance of recombination in the cells.[26b]

With these aspects, an efficiency of only 0.03% was obtained in PBTT/PDI based solar cells.

4.8 PBTT Compared to P3HT

4.8.1 Regarding Structure and Energy Levels

Generally, the regioregular polythiophenes are stable to oxygen in the dark, but susceptible to oxidative doping and photobleaching in air.[8] In PBTT, the structure motif of a 2,5 connected thiophene, which is found, for example, in the well-known poly-3-hexylthiophene (P3HT), is modified by a benzo annellation. The extended π system, furthermore, helps in forming highly ordered films which are needed to transport charge-carriers efficiently. Calculated the energy bandgap via cyclic voltammetry and absorption spectra of P3HT and PBTT, it can be found that P3HT and PBTT have similar HOMO/LUMO energy levels. P3HT has a HOMO level of -5.1 eV and a LUMO level of -3.5 eV, with a bandgap of 1.6 eV.[10] While the HOMO and LUMO levels of PBTT are -5.2 eV and -3.2 eV, respectively, with a bandgap of 2.0 eV. Due to the relatively narrow and hypsochromically shifted absorption band of PBTT comparing to that of P3HT, PBTT becomes a better candidate for tandem solar cells. In a tandem solar cell, PBTT based device can be the bottom cell, which only absorb the light in the short wavelength and high energy region. In this way, the NIR photon losing can be minimized. If the top cell can mainly harvest light in the long wavelength and low energy region, the resulted tandem cell can thus overlap the solar spectrum as much as possible and produce high photovoltaic performance.

4.8.2 Regarding Primary Variables of Polymers

The primary variables of polymers, such as molecular weight, regioregularity and polydispersity, are of critical importance for the solar cell performance.[12]

The P3HT used for comparison in this thesis is the most commonly used one, the electronic grade P3HT produced by Rieke Metals, with a regioregularity (defined as the percentage of head-to-tail linkages in the polymer) value of 90-93% and a molecular weight M_n of about 25,500 g/mol, with a polydispersity of approximately 2.

The PBTT polymer has a number average molecular weight M_n of 27,000 g/mol, a weight average molecular weight M_w of 49,000 g/mol, and polydispersity of 1.6. The easy production and low polydispersity of polymer PBTT endow the PBTT-based device with relatively higher reproducibility.

4.8.3 Regarding Aggregation

The molecular ordering, as some experiments indicated, has a direct effect on the electronic properties in these materials.[12] Both regioregular alkylsubstituted polythiophenes and PBTT have a layered structure, in which laterally packed main chains are separated by the side chains as schematically shown in Figure 16. Based on the 2D-WAXS experimental data, in PBTT, the lateral distance between polymer chains is 1.88 nm and the π-distance is 0.37 nm; while in the case of polythiophene (P3HT), the lateral distance between polymer chains and the π-distance are 1.68 nm and 0.385 nm (0.77/2 nm), respectively[27].

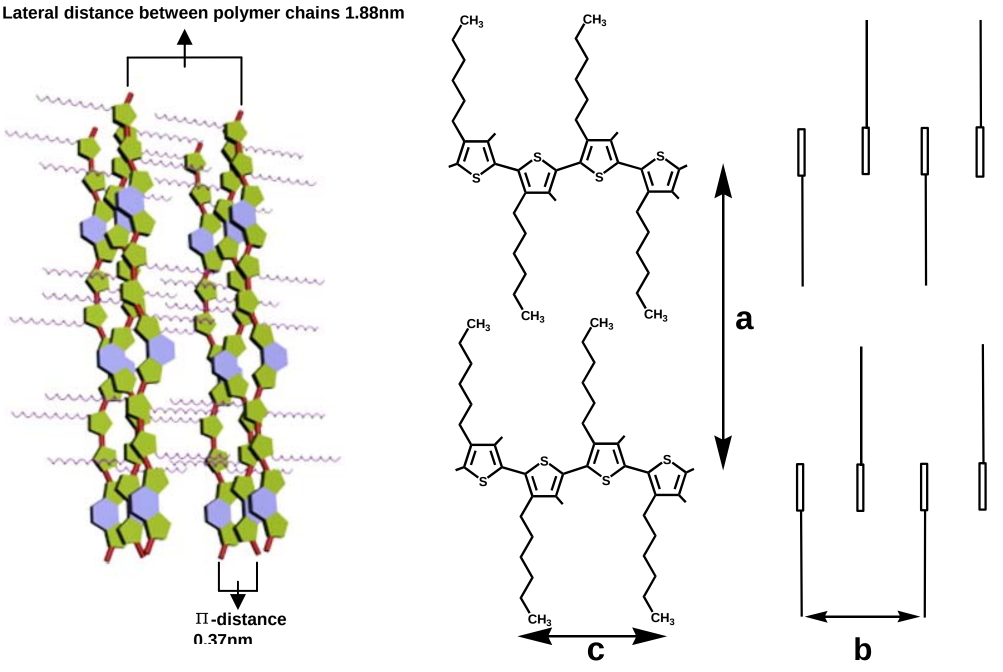

(a) (b)

Figure 16. (a) Schematic illustration of the arrangement of PBTT, based on 2D-WAXS experiments; (b) schematic illustration of the layered structure of regioregular P3HT with the definitions of the lattice parameters a, b, and c for the crystalline state (a = 1.68 nm, b = 0.77 nm, c = 0.77 nm)[27]

Due to the shorter π-π distance which results in higher order of the polymer, PBTT has better OFET properties than P3HT.[9] Under the same device fabrication and measurement process, PBTT showed a charge-carrier mobility of 0.13 $cm^2V^{-1}s^{-1}$, however, P3HT exhibited mobility of only around 0.01 $cm^2V^{-1}s^{-1}$.[9] Considering the charge-carrier mobility is one of the important factors for good charge transport in solar cells, compared with PBTT, the better photovoltaic performance of P3HT is thus likely due to the shorter interchain distance. Since the lateral distance is determined by the length and number of attached alkyl side chains, therefore, further photovoltaic improvement of benzodithiophene-thiophene based polymers should be addressed on the polymers with small alkyl chain (shorter than dodecyl) in thiophene groups.

4.8.4 Regarding Photovoltaic Performance

PBTT-based cells gave a power-conversion efficiency of 2.68% under AM1.5 simulated solar illumination of 1000 W/m^2, with a short-circuit current I_{SC} of 8.53 mA/cm^2, an open-circuit voltage V_{OC} of 0.67 V and a fill factor FF of 0.46. Under the same condition, P3HT-based cells presented an efficiency of 3.18% under one sun illumination, with a short-circuit current I_{SC} of 8.82 mA/cm^2, an open-circuit voltage V_{OC} of 0.58 V and a fill factor FF of 0.62 (Figure 17).

The main efficiency difference between these two systems lies in the aspect of fill factor FF (Table 3). Compared to V_{OC} and I_{SC}, fill factor FF is more sensitive to the bulk-material properties, blend morphology, thickness of the active layer, degradation and the morphology of the cathode-polymer interface.[28] The relatively low FF in the PBTT cells might indicate a good but not yet optimized blend morphology, still leaving a room for further efficiency improvement.

Table 3. Photovoltaic performances of the P3HT-based cells and PBTT-based BHJ cells

Donor	Isc (mA/cm^2)	Voc (V)	FF	Efficiency (%)
PBTT	8.53	0.67	0.46	2.68
P3HT	8.82	0.58	0.62	3.18

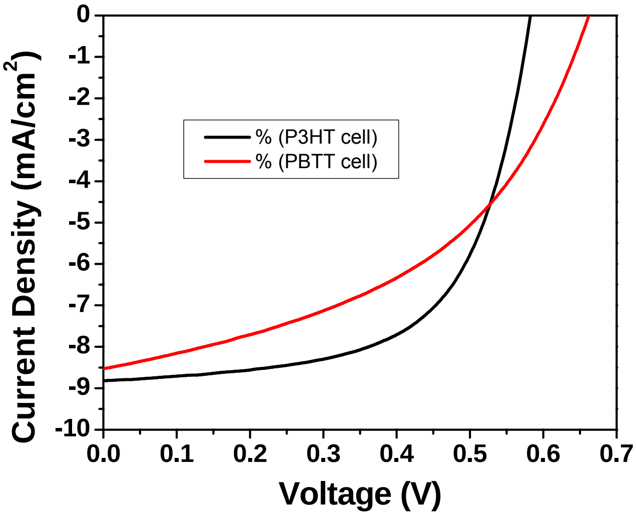

Figure 17. I-V curves of P3HT-based cells and PBTT-based cells.

When we look back the history of the prototypical P3HT/PCBM bulk-heterojunction solar cells which could achieve efficiencies of 4-5% nowadays, we notice that it is a long journey.[9a] In 2002, the dramatic effect of a mild thermal treatment at 55 °C on P3HT: fullerene active layers, a 3-fold increase in both short-circuit current from 0.86 to 2.52 mA/cm^2 and power conversion efficiency from 0.82 to 2.50%, triggered the wide interest in P3HT.[29,30] During the following five years, annealing temperatures ranging between 75 and 230°C have been reported for the thermal treatment of P3HT/PCBM active layers.[31-35,11a,11b,16a] Through the optimization of annealing temperature and time, power conversion efficiencies up to 5% have been demonstrated by annealing the cells at 150°C for 30 min.[11b] It should be noted that efficiencies varying from 3% to 5% could be achieved in the system of P3HT/PCBM in different laboratories. This indicates that the differences in polymer sample, spin-coating conditions and polymer-fullerene ratio influence the initial morphology after the spin-coating as well as the consequences of thermal annealing.[16b]

The progress made in the system of P3HT/PCBM tells us that the exploration of a new material and its optimal application in solar cells needs a comprehensive understanding of its intrinsic characteristics and the process conditions, which might take years.

Besides a more detailed investigation of the studied polymer, the new structure design based on the comprehension of existing molecular structure might be another further step into higher power conversion efficiencies.

4.9 Thought of Utilizing More Ribbon Structures

4.9.1 D-A Copolymer SCS312 with More Ribbon Structure

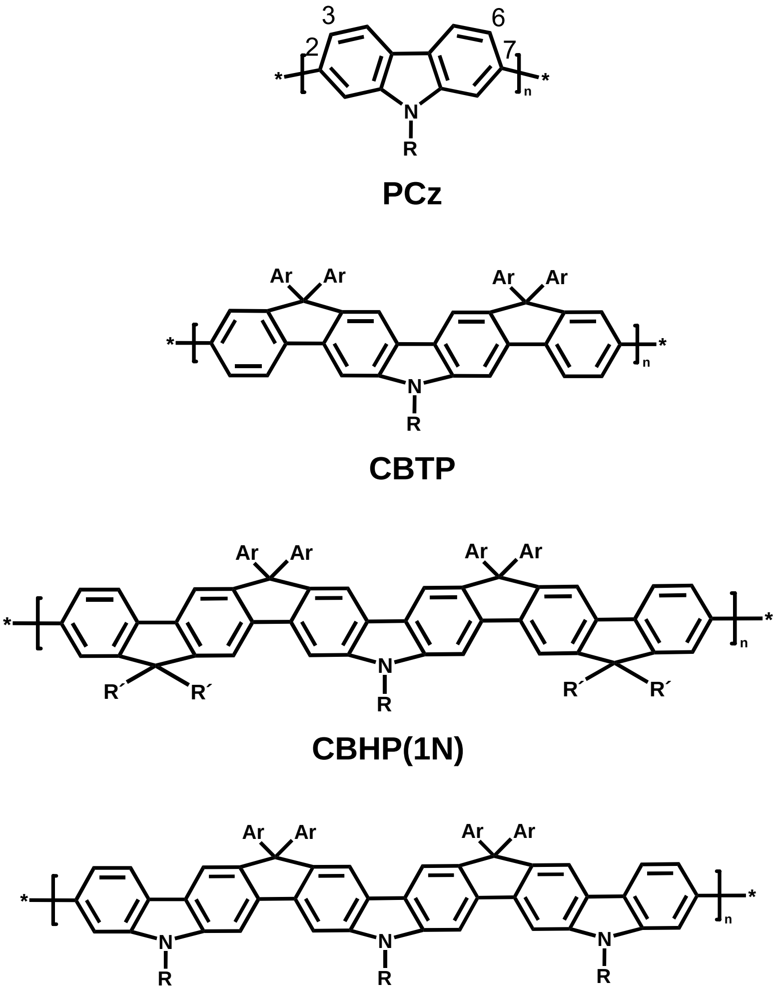

PCz

CBTP

CBHP(1N)

CBHP(3N)

Figure 18. Structure of polycarbazoles

Based on the 2.7% overall conversion efficiency obtained from polymer PBTT, the existence of another polymer with more ribbon structure is required since more ribbon structure could indicate a larger π system for better intermolecular interaction.

Previously, the strategy of using more ribbon structure to red-shift the absorption was already carried out for exploring new donor materials in our group (Figure 18). The PCz has an absorption maximum at 394 nm, while the absorption spectra of the three ladder-typed polycarbazoles CBTP, CBHP (1N) and CBHP (3N) exhibit a red-shift of 40 nm, 50 nm and 60 nm, respectively. When perylenediimide was used as acceptor, CBHP (3N)-based cells showed the best conversion efficiency of 1.4%, among these four poly(2,7-carbazole)s.

This D-A copolymer **SCS312** (Figure 19), with a molecular weight of Mn = 24,600 g/mol and Mw = 39,200 g/mol, was synthesized by Sascha Simon. Here the D-A concept is used to further red-shift the absorption, with more ribbon structure included into the backbone of the polymer (to achieve stronger packing of the polymer chains) compared with that of PBTT.

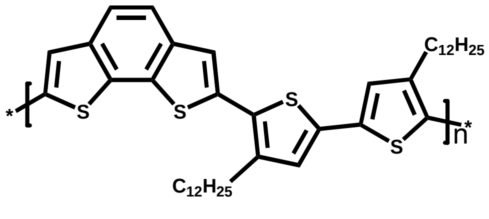

PBTT

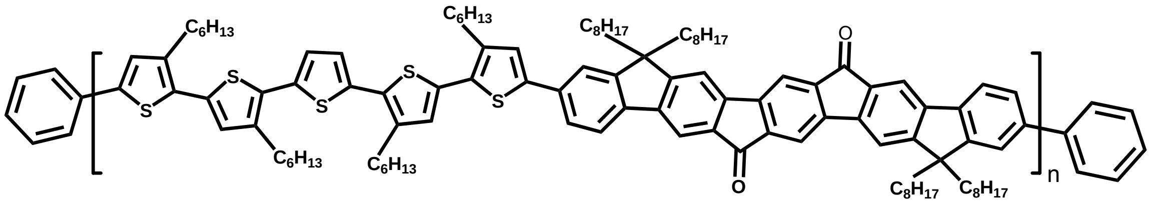

SCS312

Figure 19. Structure of PBTT and **SCS312**

4.9.2 Optical and Electrochemical Properties of SCS312

It is somewhat disappointing when we have a look at the absorption property of **SCS312**. Figure 20 presents the normalized absorption spectra of **SCS312** in $CHCl_3$, THF and toluene. An absorption maximum (λ_{max}) is observed at 431nm, 429 nm or 427 nm in the visible range of solar spectrum for **SCS312** in $CHCl_3$, THF and toluene, respectively. And as shown in the shoulder of Figure 20, the UV-vis spectra of **SCS312** exhibit a broad band that is strongly red-shifted with increasing solvent polarity in the trend of toluene, THF and $CHCl_3$. This suggests the formation of a charge transfer between the donor and acceptor unit inside the copolymer, since the effect of solvent polarity on the chemical shifts could be used to demonstrate the occurrence of the charge transfer process.[36] However, this charge transfer band is very weak, which indicates that the push-pull effect in this copolymer is not strong enough.

As it is known that the introduction of donor-acceptor push-pull effects can facilitate the electron delocalization and the formation of quinoid mesomeric structures ($D\text{-}A \rightarrow D^+{=}A^-$) over the conjugated main chain, which will reduce the polymer bandgap.[37] Here, the weak push-pull effect displayed by the flat charge-transfer band is consistent with the narrow absorption range and the large bandgap of the polymer **SCS312**.

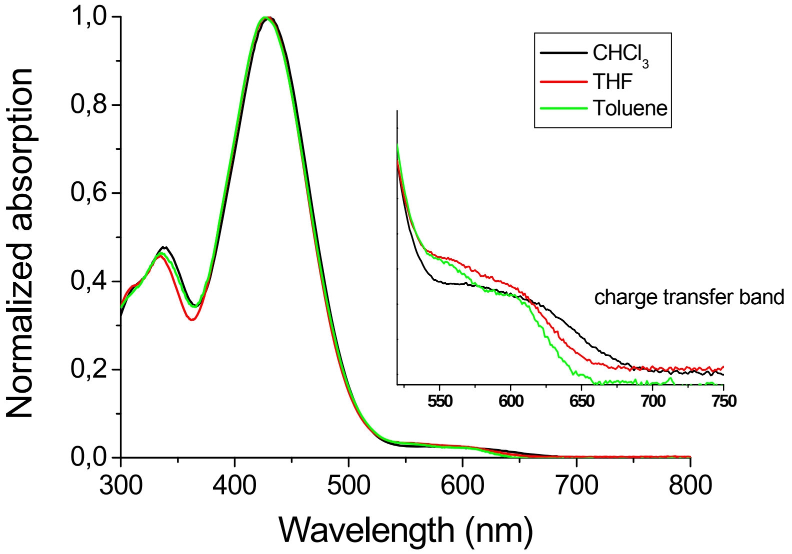

Figure 20. Normalized absorption spectra of **SCS312** in different solvents

The molecular energy levels were determined by cyclic voltammetry (CV). A highest occupied molecular orbital (HOMO) level of -5.7 eV was calculated from the onset of the oxidation peak, and the lowest unoccupied molecular orbital (LUMO) level was estimated to be -3.9 eV from the onset of the reduction peak. Regarding the matched energy level, PCBM, with a LUMO level of -4.1 eV and a HOMO level of -6.1 eV, was chosen as acceptor for polymer **SCS312**.

4.9.3 Photovoltaic Performance and Further Possible Optimizations

The photovoltaic devices were fabricated from the chlorobenzene solution of **SCS312** and PCBM with a weight ratio of 1:3. The cell gave a low efficiency of 0.41%, with a photocurrent I_{SC} of 1.71 mA/cm^2, an open-circuit voltage V_{OC} of 0.68 V and a fill factor FF of 0.26.

The low cell efficiency is believed to stem from the structure defects: the lack of C_6H_{13} in the middle thiophene unit in the copolymer backbone might reduce the regioregularity of the compound; too many thiophene units with shorter alkyl chain might result in the backbone twisting; the substituent of alkyl chain might be too weak for the push-pull effect. Correspondingly, the possibilities to modify the structure defects might be: adding alkyl chain in the middle thiophene unit in the copolymer backbone to remain the regioregularity of the compound; introducing less thiophene units but with longer alkyl chain attached to reduce the risk of twisting in the structure; or change alkyl chain to alkoxy chain to enforce the push-pull effect along the D-A backbone (Figure 21).

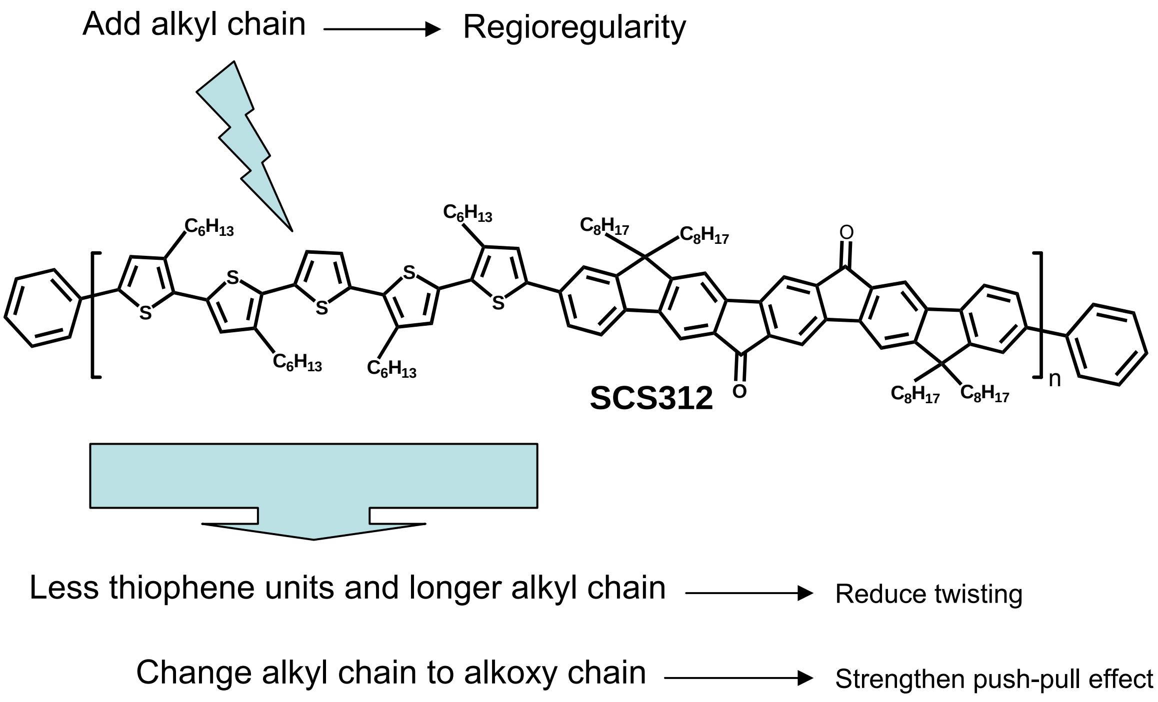

Figure 21. Possible optimization in the structure

Although this trial to use more ribbon structure (based on PBTT) to red-shift the absorption failed, more experience about molecular design can be accumulated through the unsuccessful case, which will be helpful for the future study.

4.10 Conclusion

In this chapter, we have demonstrated the characterization of an unsubstituted benzodithiophene-based conjugated polymer, PBTT, with regard to its photovoltaic performance and some related thoughts. The significant effect of thermal annealing on film aggregation has been utilized as a way to optimize the heterojunction solar-cell morphology favoring exciton dissociation and charge transport, which has been proved by the film X-ray and AFM investigation. It should be noted that the bulk-heterojunction solar cells based on PBTT as donor and [70]PCBM as acceptor showed a twofold efficiency after only two minutes' annealing. Further stepwise post-deposition annealing gave an optimal power-conversion efficiency of 2.7% under AM1.5 simulated solar illumination of 1000 W/m^2, with a short-circuit current I_{SC} of 8.53 mA/cm^2, an open-circuit voltage V_{OC} of 0.67 V and a fill factor FF of 0.46. The overall efficiency decreased by only 5% over a period of 32 days, which presents the photovoltaic device based on PBTT as a potential source of renewable energy. This promising photovoltaic system of PBTT and [70]PCBM suggests that the use of self-organizable materials is an efficient approach for high-performance photovoltaic applications.

The trial of using more ribbon structures failed to achieve higher efficiency in the case of **SCS312**, however, the experience obtained from the failure is as precious as that concluded in a successful system, for the future work.

4.11 References

[1] G. Yu, J. Gao, J. C. Hummelen, F. Wudl, A. J. Heeger, *Science* **1995**, *270*, 1789.

[2] (a) Y. Liang, Y. Wu, D. Feng, S.-T. Tsai, S.-J. Son, G. Li, L. Yu, *J. Am. Chem. Soc.* **2009**, *131*, 56; (b) H.-Y. Chen, J. Hou, S. Zhang, Y. Liang, G. Yang, Y. Yang, L. Yu, Y. Wu, G. Li, *Nature Photonics*, **2009**, *3*, 649; (c)Y. Liang, Z. Xu, J. Xia, S.-T. Tsai, Y. Wu, G. Li, C. Ray, L.Yu, *Adv. Mater.* **2010**, published online; (d) Y. Liang, D. Feng, Y. Wu, S.-T. Tsai, G. Li, C. Ray, L. Yu, *J. Am. Chem. Soc.* **2009**, *131*, 7792; (e) S.-H. Park, A. Roy, S. Beaupre, S. Cho, N. Coates, J-S. Moon, D. Moses, M. Leclerc, K. Lee, A. J. Heeger, *Nature Photonics*, **2009**, *3*, 297.

[3] http://www.solarmer.com/newsevents.php

[4] http://www.futurepundit.com/archives/003211.html

[5] J. Luo, L.-M. Peng, Z. Q. Xue, J. L. Wu, *J. Chem. Phys.* **2004**, *120*, 7998.

[6] N. Hundt, K. Palaniappan, J. Servello, D. K. Dei, M. C. Stefan, M. C. Biewer, *Org. Lett.* **2009**, *11*, 4422.

[7] H. Pan, Y. Li, Y. Wu, P. Liu, B. S. Ong, S. Zhu, G. Xu, *Chem. Mater.* **2006**, *18*, 3237.

[8] (a) B. S. Ong, Y. L. Wu, Y. N. Li, P. Liu, H. L. Pan, *Chem. Eur. J.* **2008**, *14*, 4766; (b) R. Rieger, D. Beckmann, W. Pisula, W. Steffen, M. Kastler, K. Müllen, *Adv. Mater.* **2010**, *22*, 83.

[9] (a) R. Po, M. Maggini, N. Camaioni, *J. Phys. Chem. C.* **2010**, *114*, 695; (b) T. Taima, K. Hara, K. Saito, Photovoltaic Energy Conversion, the 2006 IEEE 4th World Conference.

[10] J. Y. Kim, K. Lee, N. E. Coates, D. Moses, T.-Q. Nguyen, M. Dante, A. J. Heeger, *Science*, **2007**, *317*, 222.

[11] (a) X. Yang, J. Loos, S. C. Veenstra, W. J. H. Verhees, M. M. Wienk, J. M. Kroon, M. A. J. Michels, R. A. J. Janssen, *Nano Lett.* **2005**, 5, 579; (b) W. Ma, C. Yang, X. Gong, K. Lee, A. J. Heeger, *Adv. Funct. Mater.* **2005**, 1*5*, 1617; (c) H. Hoppe, N. S. Sariciftci, *J. Mater. Chem.* **2006**, *16*, 45; (d) A. R.

Campbell, J. M. Hodgkiss, S. Westenhoff, I. A. Howard, R. A. Marh, C. R. McNeil, R. H. Friend, N. C. Greenham, *Nano Lett.* **2008**, *8*, 3942.

[12] B. C. Thompson, J. M. Frechet, *Angew. Chem. Int. Ed.* **2008**, *47*, 58.

[13] J. K. Lee, W. Ma, C. J. Brabec, J. Yuen, J. S. Moon, J. Y. Kim, K. Lee, G. C. Bazan, A. J. Heeger, *J. Am. Soc. Chem.* **2008**, *130*, 3619.

[14] A. C. Mayer, M. F. Toney, S. R. Scully, J. Rivnay, C. J. Brabec, M. Koppe, M. Heeney, I. McCulloch, M. D. McGehee, *Adv. Funct. Mater.* **2009**, *19*, 1173.

[15] F. Padinger, R. S. Rittberger, N. S. Sariciftci, *Adv. Funct. Mater.* **2003**, *13*, 85.

[16] (a) Y. Kim, S. A. Choulis, J. Nelson, D. D. C. Bradley, S. Cook, J. R. Durrant, *Appl. Phys. Lett.* **2005**, *86*, 063502; (b) B. C. Thompson, J. M. J. Frechet, *Angew. Chem. Int. Ed.* **2007**, *46*, 2.

[17] S. S. Pandey, S. Sakaguchi, Y. Yamaguchi, S. Hayase, *Organic Electronics*, **2009**, in press.

[18] M. C. Scharber, D. Mühlbacher, M. Koppe, P. Denk, C. Waldauf, A. J. Heeger, C. J. Brabec, *Adv. Mater*. **2006**, *18*, 789.

[19] D. Muhlbacher, M. Scharber, M. Morana, Z. G. Zhu, D. Waller, R. Gaudiana and C. Brabec, *Adv. Mater.* **2006**, *18*, 2884.

[20] M. M. Wienk, J. M. Kroon, W. J. H. Verhees, J. Knol, J. C. Hummelen, P. A. Van Hal, R. A. J. Janssen, *Angew. Chem. Int. Ed.* **2003**, *42*, 3371.

[21] (a) J. Li, M. Kastler, W. Pisula, J. W. F. Fobertson, D. Wasserfallen, A. C. Grimsdale, J. Wu, K. Müllen, *Adv. Funct. Mater.* **2007**, *17*, 2528; (b) X. Feng, M. Liu, W. Pisula, M.Takase, J. Li, K. Müllen, *Adv. Mater.* **2008**, *20,* 2684; (c) L. Schmidt-Mende, A. Fechtenkötter, K. Müllen, E. Moons, R. H. Friend, J. D. MacKenzie, *Science,* **2001**, *293*, 1119.

[22] (a) G. li, V. Shrotriya, J. Huang, Y. Yao, T. Moriarty, K. Emery, Y. Yang, *Nat. Mater.* **2005**, *4*, 864; (b) Y. Kim, S. Cook, S. A. Choulis, J. Nelson, J. R. Durrant, D. D. C. Bradley, *Synth. Met.* **2005**, *152*, 105.

[23] http://en.wikipedia.org/wiki/Solar_cell

[24] (a) http://cp.literature.agilent.com/litweb/pdf/5990-4428EN.pdf; (b) D. K. Schroder, *Semiconductor Material and Device Characterization (Third Version)*, John Wiley & Sons, Inc. **2006**.

[25] S.M. Sze, *Physics of Semiconductor Devices*, John Wiley & Sons, Inc. **1981**.

[26] (a) J. Li, F.Dierschke, J. Wu, A. C. Grimsdale, K. Müllen, *J. Mater. Chem.* **2006**, *16*, 96; (b) Q. Qiao, Y. Xie, J. T. Mcleskey, *J. Phys. Chem. C*, **2008**, *112*, 9912.

[27] (a) T. J. Prosa, M. J. Winokur, *Macromolecules*, **1992**, *25*, 4364; (b) S. Hugger, R. Thomann, T. Heinzel, T. Thurn-Albrecht, *Colloid Polym Sci.* **2004**, *282*, 932; (c) T. J. Prosa, M. J. Winokur, *Macromolecules*, **1996**, *29*, 3654.

[28] D. Gupta, S. Mukhopadhyay, K. S. Narayan, *Sol. Energy Mater. Sol. Cells*, **2008**, doi : 10.1016/j.solmat.2008.06.001.

[29] N. Camaioni, L. Garlaschelli, A. Geri, M. Maggini, G. Possamai, G. Ridolfi, *J. Mater. Chem.* **2002**, *12*, 2065.

[30] N. Camaioni, G. Ridolfi, G. Casalbore-Miceli, G. Possamai, M. Maggini, *Adv. Mater.* **2002**, *14*, 1735.

[31] F. Padinger, R. S. Rittberger, N. S. Sariciftci, *Adv. Funct. Mater.* **2003**, *13*, 85.

[32] G. Li, V. Shrotriya, Y. Yao, Y. Yang, *J. Appl. Phys.* **2005**, *98*, 043704.

[33] T. Erb, U. Zhokhavets, G. Gobsch, S. Raleva, B. Stuhn, P. Schilinsky, C. Waldauf, C. J. Brabec, *Adv. Funct. Mater.* **2005**, *15*, 1193.

[34] V. D. Mihailetchi, H. Xie, B. de Boer, L. J. A. Koster, P. W. M. Blom, Adv. Funct. Mater. **2006**, *16*, 699.

[35] M. Campoy-Quiles, T. Ferenczi, T. Agostinelli, P. G. Etchegoin, Y. Kim, T. D. Anthopoulos, P. N. Stavrinou, D. D. C. Bradley, J. Nelson, *Nat. Mater.* **2008**, *7*, 158.

[36] Y. Matsubara, H. Tada, S. Nagase and Z. Yoshida, *J. Org. Chem.* **1995**, *60*, 5372.

[37] Y.-J. Cheng, S.-H. Yang, C.-S. Hsu, *Chem. Rev.* **2009**, *109*, 5868.

Chapter 5 Novel Organic Sensitizers for Solid-state Dye-sensitized Solar Cells

Organic dyes are now the key components in solid-state dye-sensitized solar cells due to their various synthetic pathways, easily tunable optical and electronic properties, environment benignity and low cost. The goal of this chapter is to introduce two novel organic sensitizers for solid-state dye-sensitized solar cells, based on the considerations that: 1) the typical thickness of TiO_2 films used in solid-state DSSCs is around 2 μm, which limits the device performance of ruthenium-sensitized solid-state cells because of the relatively low absorption coefficients of ruthenium dyes.[1] One strategy to improve the photovoltaic performance of dye-sensitized solar cells is to enhance the molar absorptivities of sensitizers in view of the tradeoff of light-harvesting and series resistance.[2] Hence, organic dyes with higher absorption coefficients and broader absorption spectra are needed; 2) most organic sensitizers are small molecules and contain UV-unstable cyanoacrylic acid group with donor-bridge-acceptor structures. Therefore, the exploration of new dyes with improved stabilities is also of great importance; 3) the exploration of two sensitizers with an absorption complementarity is the basis for fabricating a molecular cocktail solar cell.[3]

In this chapter, one perylene dye **ID176** and one isophorone sensitizer **Ind-1** were investigated in solid-state DSSCs in the sense that 1) they possess either good thermal stability or high absorption coefficient: the investigated perylene monoimide exhibits an absorption maximum of 566nm on the dye-grafted TiO_2 film, with an outstanding thermo-, photo-, and chemical stability; the λ_{max} of the isophorone dye **Ind-1** on semiconductor surface is located at 447 nm. The power conversion efficiency of **ID176** and

Ind-1 based solid-state solar cells was 2.2 and 1.9%, respectively; 2) the absorptions of these two sensitizers complement each other which makes it possible to build a molecular cocktail solar cell which can cover the whole region of visible light spectrum.

5.1 A Stable Perylene Dye for Solid-state Dye-sensitized Solar Cells

5.1.1 Introduction

In the colorant family, perylene dyes are the most stable compounds and are easy to be functionalized for various purposes. They are widely used in many fields, such as paints and lacquers (particularly in the car industry), fluorescent solar collectors[4a], optical switches[4b], and dye lasers[4c].

With their high molar absorption coefficients and their extraordinary thermal, photochemical and photophysical stability, perylene dyes have emerged for application in dye-sensitized solar cells for years. The first perylene sensitizer (PPDCA) was applied in the liquid cell by Gregg et al., exhibiting an overall efficiency of 0.9% under one sun light illumination.[5] Later on, with UV-treatment of devices, a higher efficiency of 1.9% was reached by using 9-dioctylaminoperylene-3,4-dicarboxylic acid anhydride (**P1**) as sensitizer.[6] The primary effect of the UV treatment is believed to be a positive shift in the conduction band of the nanocrystalline titanium dioxide, which promotes electron injection from the dye and results in a dramatically increased photocurrent in the cells.[7] An overall conversion efficiency of 2.6% was achieved when perylene derivative *i*Pr-PMI was applied in the liquid state cells.[8] However, all these above mentioned sensitizers (Figure 1) showed low efficiency, even in the liquid state cells.

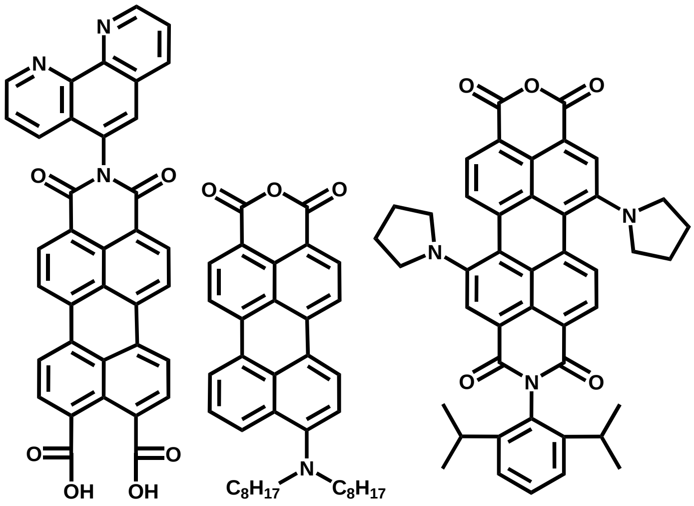

Efficiency 0.9 % 1.9 % 2.6 %

PPDCA **P1** ***i*Pr-PMI**

Figure 1. Structures of some perylene sensitizers

A successful approach was introduced by using alkyl-substituted diphenylamine as an electron-donating group instead of dialkylamine previously reported, leading to perylene dyes with a stronger push-pull effect, higher intramolecular charge-transfer (ICT) character and better stability. One of these perylenes, 9-bis(*p*-*tert*-octylphenyl)amino-perylene-3,4-dicarboxlic acid monoanhydride (coded as **ID28**), exhibited a remarkable power conversion efficiency of up to 4% in dye-sensitized solar cells using a liquid electrolyte under global standard AM 1.5 sun light irradiation.[9] However, only an efficiency of 0.1% was demonstrated by **ID28**-grafted solid-state cells. The device efficiency variation of **ID28** in liquid-state and solid-state cells is not that surprising, since solid-state DSSCs normally show lower conversion efficiencies compared to their liquid counterparts.[10]

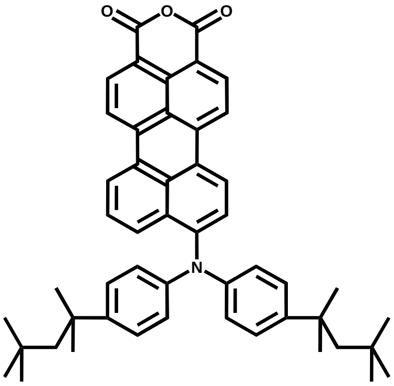

ID28

Figure 2. Structure of perylene sensitizer **ID28**.

One disadvantage of these previously published perylenes is that a significant spectral blue shift of their absorption spectra upon the attachment to TiO_2 due to the ring opening of an anhydride group. Herein, a new perylene sensitizer **ID176** (Figure 3), derived from its precursor **ID28,** possesses a carboxylic acid anchor instead of an anhydride anchor attached to the perylene monoimide. The change of anchor was successful for obtaining a red absorbing dye when attached to TiO_2, because only a slight blue shift in the absorption maximum of **ID176** was observed upon adsorption to TiO_2 (Figure 4). And **ID176** absorbs strongly from 400 to above 700 nm, which can cover a large range of the solar spectrum. Furthermore, **ID176** has a higher molar absorption coefficient than that of **ID28**, enabling its application in the solid-state cells with thinner films.

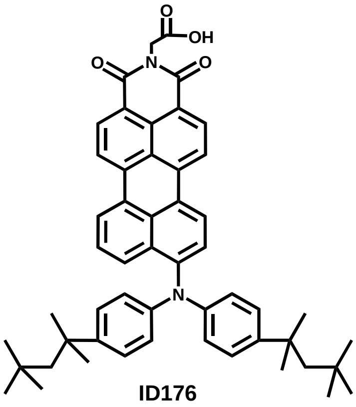

ID176

Figure 3. Structure of perylene derivative **ID176**

This novel perylene sensitizer **ID176** [N-carboxymethyl-9-bis(*p-tert*-octylphenyl)amino-perylene-3,4-dicarboximide] was provided by Dr. Chen Li. It was synthesized by imidization of **ID28** with amino acetic acid (i.e. glycine) and characterized by ^{1}H-NMR, ^{13}C-NMR, IR, UV-vis absorptionspectroscopy, elemental analysis and cyclic voltammetry.

5.1.2 Optical Properties

The UV-vis-IR absorption characteristics of **ID176** and its precursor **ID28** in dichloromethane were investigated (Figure 4a). Under the same condition, the molar absorption coefficient (ε) of **ID28** was 12197 $M^{-1}cm^{-1}$ at 606 nm, while that of **ID176** was 20942 $M^{-1}cm^{-1}$ at 582 nm. The higher the molar absorption coefficient of the dye has, the more light is absorbed with a certain quantity of dye material. [1] Compared with **ID28**, the high molar absorption coefficient of **ID176** allows for absorbing still enough amount of light in case of thinner film in solid state devices compared with wet cells, and also an easier tradeoff of light-harvesting and series resistance.[1]

ID176 absorbs strongly from 400 to above 700 nm, covering a large range of the solar spectrum. And it has an absorption peak at 580 nm in dichloromethane, which is attributed to an intramolecular charge transfer (ICT) band. It is noteworthy that the ε of **ID176** (20942 $M^{-1}cm^{-1}$) is higher than that of standard **N3** dye [chemical name: cis-bis(isothiocyanato)-bis(2,2’-bipyridyl-4,4’ dicarboxylato)ruthenium(II)] (14200 $M^{-1}cm^{-1}$ at 532 nm)[11].

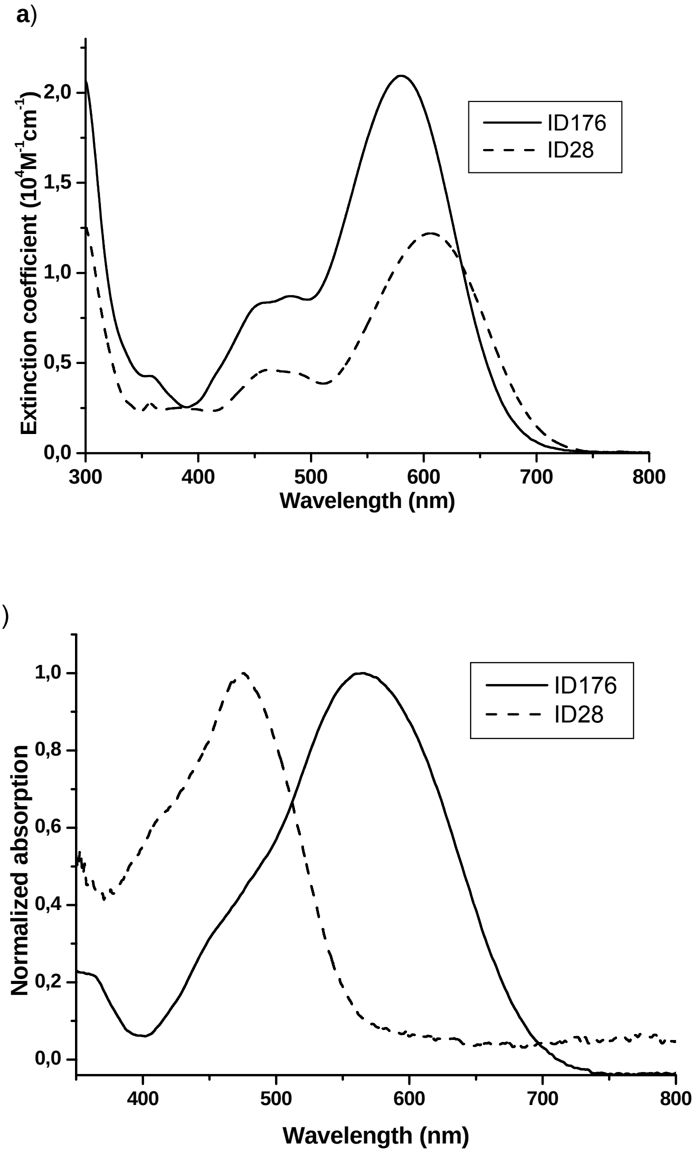

Figure 4. a) UV-vis-IR absorption spectra of **ID176** (solid line) and **ID28** (dashed line) in dichloromethane; b) UV-vis absorption spectra of **ID176** (solid line) and **ID28** (dashed line) adsorbed on a transparent 2 μm mesoporous TiO_2 film.

From the absorption spectra of dye-modified TiO_2 films (Figure 4b), it is observed that, compared with its absorption spectra in dichloromethane, **ID176** showed a slightly blue-shifted absorption when loaded onto TiO_2 with the imide structure remained throughout the dye-uptaking process, and presented a broad absorption range from 350 nm to 750 nm. This observation of slightly blue-shifted absorption overcomes the shortcoming of anhydride anchors used in previously reported perylene sensitizers,[8,9,12] in which the ring opening of an anhydride group resulted in a large spectral blue shift of their absorption spectra upon the loading of TiO_2.

For comparison, ID28 presented a significant blue-shifted absorption from 606nm to 476 nm when loaded onto TiO_2 due to the ring opening of the anhydride group on perylene to form two carboxylates and demonstrated narrower absorption spectra from 350 nm to 600 nm.[9] Hence, for **ID176**, both a 90 nm bathochromic shifted absorption compared to **ID28** (difference between 566 nm and 476 nm) and the broader absorption spectra provided the cells sensitized by **ID176** with a more efficient light-harvesting.

5.1.3 Electrochemical Properties

The potential applicability of **ID176** as a sensitizer in DSSCs was confirmed by the cyclic voltammetry (CV) measurements (Figure 5). The LUMO of **ID176** (-0.68 V versus NHE, normal hydrogen electrode) is more negative than the conduction band edge of TiO_2 (-0.5 V versus NHE),[13a] suggesting a thermodynamically favorable electron injection from the oxidized dye to conduction band of TiO_2, although the driving force is not large. On the other hand, the HOMO of **ID176** (1.1 V versus NHE) is more positive than the valence band edge of spiro-MeOTAD (~ 0.8 V versus NHE),[13b,16a] which will ensure an effective dye regeneration, avoiding the geminate charge recombination between oxidized dye molecules and photoinjected electrons in the nanocrystalline titania film.

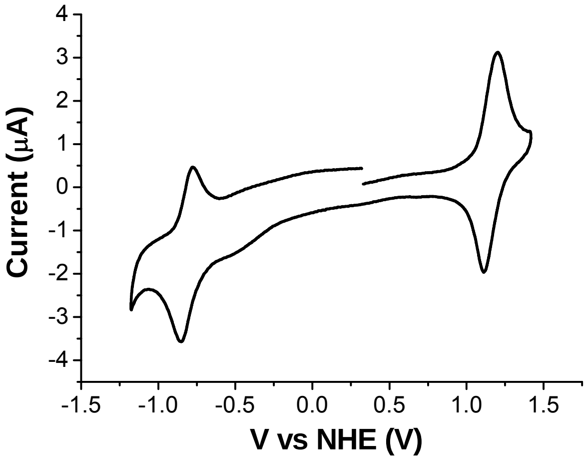

Figure 5. Cyclic voltammetry of **ID176**

To gain further insight into the redox stability of **ID176**, mutli-cyclic voltammetry was performed (Figure 7).

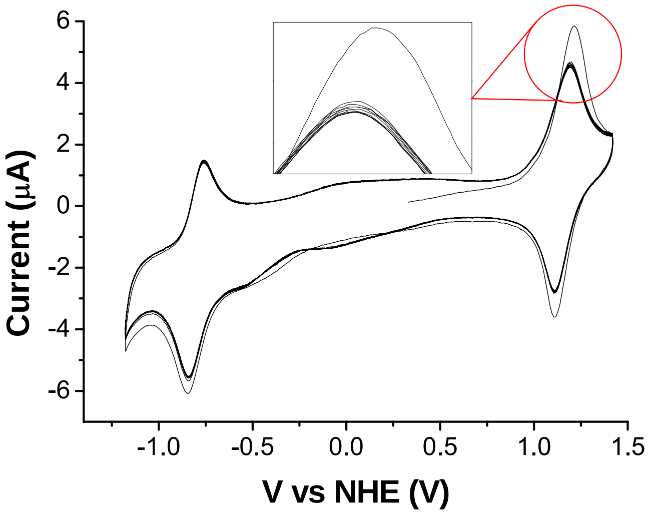

Figure 6. Multi-cyclic voltammetry of **ID176**

As shown in Figure 6, **ID176** exhibits the perfect redox stability of and the potential for durable DSSCs. Although the high molar absorption coefficients of some organic sensitizers make them ideal absorbers for solid-state dye-sensitized solar cells, the poor photochemical stability of these sensitizers influences the realization of stable devices.[1] Both the high molar absorption coefficients and good photochemical stability of ID176 makes it a good candidate for stable and efficient DSSCs.

5.1.4 Device Fabrication

ID176 was investigated as sensitizer in the device employing 2,2′,7,7′-tetrakis(N,N-di-*p*-methoxyphenylamine)-9,9′-spirobifluorene (spiro-OMeTAD) as the hole-transport material. The solid-state dye-sensitized solar cells were fabricated in the following steps: SnO_2: F glass (FTO, purchased from Solaronix SA) was ultrasonicated with acetone, ethanol, Helmanex, H_2O and ethanol successively, then finally cleaned by an oxygen plasma for 10 mins. The TiO_2 barrier layer was prepared from a sol-gel solution on FTO glass. A nanostructured TiO_2 layer was fabricated via doctor-blading the TiO_2 paste (Ti-Nanoxide T, Solaronix), followed by calcination at 450 °C. **ID176** was absorbed to the TiO_2 film by immersion overnight in a $3X10^{-4}$ mol/L solution in o-xylene (or other solvents) and subsequently rinsed by o-xylene (or other corresponding solvents). The hole conductor matrix was applied by spin coating of a solution of spiro-MeOTAD (0.15 M) in chlorobenzene, containing $Li(CF_3SO_2)_2N$ (30 mM), 4-*tert*-butylpyridine (0.11 M) and $N(PhBr)_3SbCl_6$ (0.4 mM). Finally a gold contact of 40 nm was deposited by evaporation.

5.1.5 Solvent Effects-Solvatochromic Solar Cells

Scientists have put many efforts to explore new dye molecules with broad spectral sensitization to optimize the energy conversion efficiency.[11,14]

Herein, the observed solvent effect, so called solvatochromic phenomenon, provides another approach to adjust the spectral sensitization. In other words, solvents for preparing the dye uptake solution can be used to tune the spectral response and efficiency of dye-sensitized solar cells. It appears that the efficiency and spectral response of these solar cells can be tuned by using different solvents for the dye uptake.

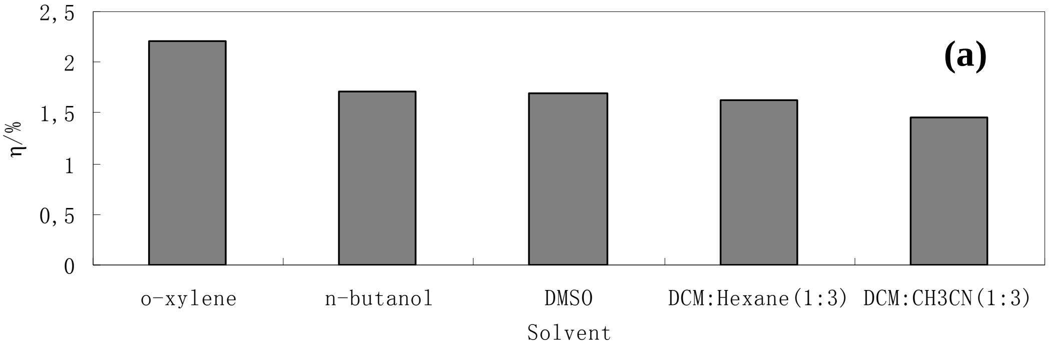

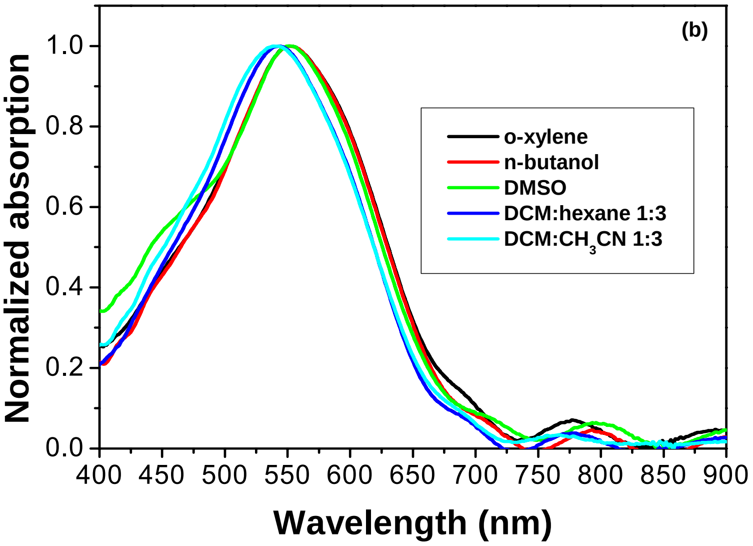

Figure 7. a) Efficiencies of devices sensitized by **ID176** dissolved in o-xylene, n-butanol, DMSO, dichloromethane (DCM): Hexane (1:3) and DCM: CH_3CN (1:3), respectively; b) Normalized absorption spectra of dye-grafted TiO_2 film (2 μm) with sensitization from ID176 solutions dissolved in different solvents.

A different photovoltaic behavior was observed in devices sensitized by **ID176** dissolved in different solvents. **ID176** was dissolved in five solvents, o-xylene, n-butanol, DMSO, dichloromethane(DCM) : hexane(1:3) and DCM : CH_3CN(1:3), respectively. The device immersed in the o-xylene solution of **ID176** presented the highest efficiency of 2.2%, while the cells with a dye-uptake from the other four solvents exhibited lower efficiencies (Figure 7a).

To investigate the reason for these results, the absorption properties of dye-grafted TiO_2 films with sensitization from **ID176** solutions dissolved in these five solvents were tested under same conditions (TiO_2 film thickness: 2 μm, dye-loading time: 12 h). The TiO_2 film immersed in **ID176**'s o-xylene solution shows a red-shifted absorption relative to that of the other four solutions (Figure 7b), which is in agreement with the best photovoltaic performance of devices sensitized with dyes dissolved in o-xylene.

A negative solvatochromism, that is, a blue shift of the charge-transfer band in more polar solvents, is observed (Figure 7b). This could be attributed to the deprotonation of the carboxylic acid which reduces the pulling ability of the electron acceptor.[15] This type of negative solvatochromism is claimed to be common for dipolar metal-free dyes.[15a]

5.1.6 Device Performance

The solid-state devices sensitized by **ID176** exhibit an overall conversion efficiency of 2.2% under AM 1.5 (100 mW/cm^2) simulated sunlight illumination. The photocurrent action spectrum of the device with **ID176** as sensitizer is shown in Figure 8a. The incident photon-to-current conversion efficiency (IPCE) demonstrates a broad spectral range from 400 nm to 850 nm, with a spectral response into the near IR region, reaching its maximum of 18% at 570 nm. The short-circuit photocurrent density (J_{SC}), open circuit potential (V_{OC}), and fill factor (ff) of the device sensitized by **ID176** are 5.1 mA/cm^2, 0.81 V, and 0.56, respectively, yielding an overall conversion efficiency of 2.2%. Although **ID176** has a broad spectral coverage with the solar irradiation spectrum, the small driving force for electron injection, derived from the offset between the LUMO of **ID176** (-0.68 V vs NHE) and the conduction band edge of TiO_2 (-0.5 V vs NHE), is thought to be the main limiting factor for the device efficiency.

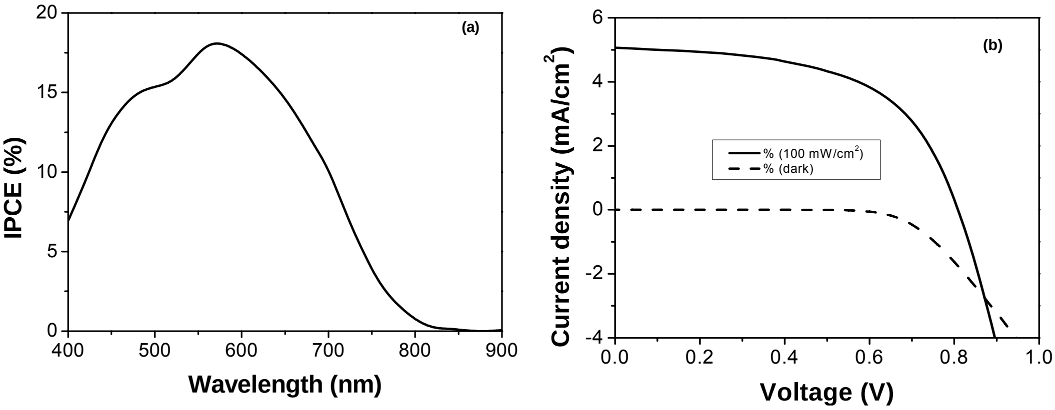

Figure 8. a) Photocurrent action spectrum of solid-state device sensitized by **ID176**. b) Current density-voltage characteristics of devices measured under AM 1.5 (100 mW/cm^2) simulated sunlight illumination (solid line) and in the dark (dashed line), respectively.

For comparison, we measured the photovoltaic performance of **ID176**, **ID28** and standard **N3** dye ([Ru(2,2'-bipyridyle-4,4'-dicarboxylate)$_4$(NCS)$_2$]H$_4$) were measured under the same conditions, as shown in Table 1. A much lower overall efficiency of only 0.1% was observed for **ID28**-sensitized solid-state cells, while **N3**-sensitized solid cells demonstrated an overall efficiency of 2.5%. It appears that the new perylene sensitizer exhibits an overall efficiency comparable to that of the ruthenium sensitizer **N3** in solid-state dye-sensitized solar cells.

Table 1. Comparison of photovoltaic performance between solid-state devices sensitized by **ID176**, **N3** and **ID28** under AM 1.5 full sunlight illumination.

Sensitizer	J_{sc} (mA/cm^2)	V_{oc} (mV)	FF	η^a (%)
ID176	5.1	810	0.56	2.2
N3	6.81	760	0.48	2.55
ID28	0.27	720	0.56	0.1

[a] Hole-transport material: spiro-MeOTAD (0.15M) in chlorobenzene, containing $Li(CF_3SO_2)_2N$ (30mM), 4-*tert*-butylpyridine (0.11M) and $N(PhBr)_3SbCl_6$ (0.4mM).

In a DSSC cell, it seems to be a critical issue to achieve a high value of V_{oc}. In a solid-state DSSC, the maximum value of V_{oc} is determined by the difference between the quasi Fermi level in TiO_2 under illumination and the oxidation potential of the hole transporting material.[16a,16b] The theoretical value of V_{oc} is limited to be about 1.2~1.3 V because of the energy offset between the TiO_2 conduction band edge (-0.5/-0.4 V vs NHE) and the HOMO level of Spiro-MeOTAD (0.8 V vs NHE). [16a] Normally, a DSSC results in a V_{oc} with the value of around 0.7 V which is much lower than the band gap (~1.5-2.5 eV) of the light absorber, due to the necessity of simultaneously ensuing a high driving force for both electron injection into conduction band of TiO_2 and rapid regeneration of the oxidized dye [16a] and the voltage loss from the interfacial charge recombination.

It is shown in Table 1 that, the high power conversion efficiency of the **ID176**-sensitized solar cell is mainly due to its high open-circuit voltage. The dipole moment of the adsorbed molecules has strong effects on the chemical potential shift at organic-inorganic interface and consequently on the photovoltage.[16a] This effect is likely to induce a shift in the position of the semiconductor conduction band, which yields the high open-circuit voltage in dyes via offsetting the energy level between the n-type TiO_2 and the p-type HTM. Thus, under the same solar irradiation, the V_{oc} difference of these three compounds (**ID176**, **N3**, **ID28**)-sensitized solar cells could imply the various TiO_2 conduction band edge values in the devices, since the value of V_{oc} in solid-state DSSCs is related to the energy offset between the TiO_2 conduction band edge and the HOMO level of Spiro-MeOTAD. The V_{oc} of the device based on the **ID176** is around 50 mV higher than that of the device employing the **N3** dye, indicating that the higher V_{oc} is related to an upward shift of the TiO_2 conduction band edge toward more negative potentials vs NHE. This result also indicates that the dyes can indirectly respond to the V_{oc} of the devices.

Compared to **N3**-based cells**,** the lower power efficiency of **ID176**-sensitzed devices is mainly caused by the low photocurrent. The small difference between the LUMO of **ID176** (-0.68 V vs NHE) and the conduction band edge of TiO_2 (-0.5 V vs NHE) indicates that the driving force for electron injection is not large. Whereas, the LUMO of **N3** is located at -0.86 V vs NHE,[16c] with a larger distance from the conduction band edge of TiO_2. It implies that further improvement of device performance should be addressed by either the tuning of the LUMO level of the dye to a more negative position or the Fermi level of TiO_2: 1) The adjustment of LUMO level can be realized by the functional groups in the *peri* and *bay* positions of perylene core. The introduction of a weaker acceptor than imide group, for example, a lactame imide moiety, in the *peri* position or a donor group in the *bay* position is expected to be an efficient method to uplift the LUMO level of perylene sensitizers. 2) The Fermi level of TiO_2 can be modified via the additives such as lithium salts.[16d]

Additionally, the observation that **ID28** showed only an efficiency of 0.1% demonstrates that, dyes, which have been successfully applied in electrolyte DSSCs (for example **ID28**, 4% in liquid cell), may not be good candidates for solid-state DSSCs, because different mechanisms of electrons injection and dyes regeneration exist in two systems.

5.1.7 Device Stability

Since photostability is a vital parameter for sustained cell operation, the cell performance changes under the illumination of white light have been studied.

Many stability tests reported up to now were, however, carried out by using a UV cut-off filter which could not imitate realistic conditions. For example, the sealed cells based on **N3** did give good long-term stability under continuous irradiation with the application of a 4 mm polycarbonate 395 nm cutoff filter to exclude UV light.[17a] Organic dyes, a merocyanine dye[17b] and a coumarin dye[17c], also showed good stability in sealed cells under continuous AM1.5 irradiation with a UV (< 420 nm) cutoff filter. However, stability testing result for these devices without a UV cutoff filter was not mentioned. Interestingly, a conjugated organic dye (coded as **NKX-2569**) demonstrated totally different photostabilty behavior when the device was tested with or without a UV (< 420 nm) cutoff filter:[17d] no degradation of the solar cell performance of a DSSC based on **NKX-2569** was observed under white light irradiation with a UV filter; whereas under AM1.5 irradiation without a UV cutoff filter, the color of the dye changed and consequently the solar cell performance decreased remarkably. This is believed to be a consequence of the structural modification of dye molecules attacked by the high-energy holes in titania, if the UV photons are not filtered.[17e]

The unsealed **ID176**-sensitized device showed a rather stable photovoltaic performance upon successive testing at full sun light illumination without a UV filter (Figure 9). After 1220 h of light soaking under ambient atmosphere, the overall efficiency decreased slightly from 2.2% to 2.0% with unsealed cells. The photovoltage remained nearly the same (from 810 to 800 mV) during the light-soaking testing. Although there was a decrease in the photocurrent from 5.1 to 3.9 mA/cm^2, this loss was compensated by an increase in the fill factor from 0.56 to 0.6, still leading to a stable overall efficiency.

To check the cell stability over a longer period, the **ID176**-based cell was set under daylight in the air for six months. No noticeable photodegradation of **ID176** was observed, since no significant change was seen in the cell efficiency. It must be concluded that, this perylene sensitizer shows both high efficiencies and high photostability in DSSCs.

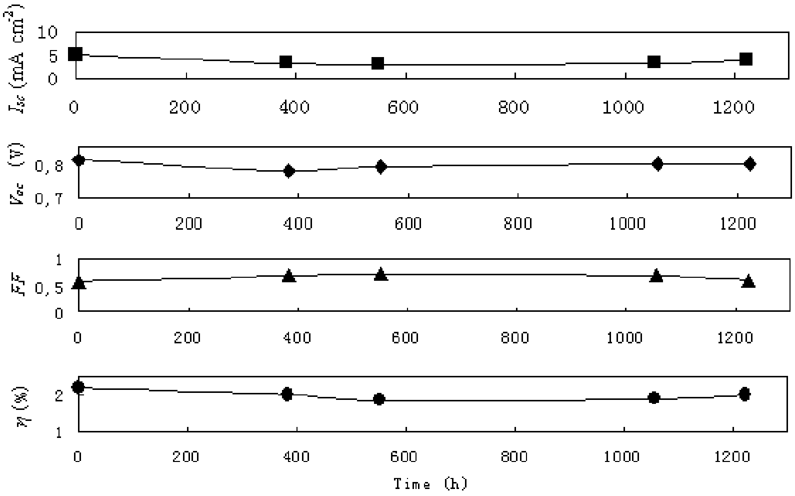

Figure 9. Detailed photovoltaic parameters (Jsc, Voc, FF, and η) for **ID176**-sensitized solid state devices during continuous visible-light soaking

5.1.8 Conclusion

In this part, a new perylene sensitizer, with high molar absorption coefficient and good photochemical stability, has been utilized as an efficient sensitizer in the solid state dye-sensitized solar cells. An overall conversion efficiency of up to 2.2% under standard global AM 1.5 sunlight illumination has been reached, which is a relatively high efficiency reported for perylene sensitizers in solid-state dye-sensitized solar cells. Additionally, the novel perylene sensitizer shows a comparable performance with **N3** sensitizer under the same conditions. It is noteworthy that devices sensitized with this metal-free organic dye present excellent performance stabilities under light soaking without a UV filter for 1220 h. It should also be noted that, the solvatochromic phenomenon observed functioned to adjust the spectral sensitization efficiently.

In a word, this perylene sensitizer is a successful trial for exploring new organic dyes with high molar absorption coefficient and photo-electrochemical stability.

5.2 An Isophorone Dye for Solid-state Dye-sensitized Solar Cells

The absorption of **ID176** in the visible region could allow its use in combination with an appropriate dye to achieve panchromatic sensitization of the mesoporous photoelectrode and increase the device efficiency.

The use of several dyes as co-sensitizers, so called molecular cocktail, has been explored to extend the spectral region of the sensitizing layer. In the case of organic dyes, this approach may also overcome the typically narrow absorption bands observed for these dyes. It is believed that a co-sensitization approach can lead to enhanced spectral coverage and better enable the use of organic dyes, which typically display high extinction coefficients.[18]

Based on this consideration and the experience with the above investigated perylene sensitizer **ID176**, we looked for another organic sensitizer with a complementary absorption property with that of **ID176**. An isophorone dye (coded as **Ind-1),** with a relatively blue-shifted absorptivity (compared to that of **ID176**) and a high absorption coefficient, came to our mind. This isophorone dye itself demonstrated a good efficiency of 1.9% in the solid-state cells.

5.2.1 The Isophorone Dye Ind-1

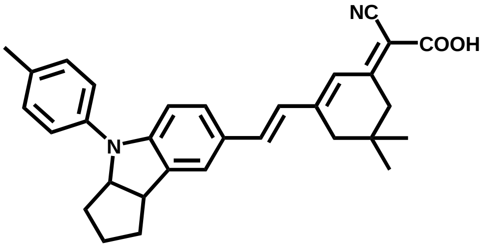

Figure 10. The chemical structure of **Ind-1**

The isophorone dye **Ind-1** (provided by the group of Prof. He Tian) (Figure 10), was designed with the consideration of applying steric linker groups for the conjugation expansion and molar absorption coefficient increase. The commercially available isophorone unit in **Ind-1** functions as the bridge to provide conjugation between the donor (indoline unit) and the anchoring groups in this typical donor-linker-acceptor (D-π-A) system.

Most efficient metal-free organic sensitizers consist of donor, π-conjugation linker and acceptor moieties (D–π–A),[19] in which the donor moiety functions to affect absorption spectra and adjust the energy levels of sensitizers.[20,21] The π-conjugated ring unit between donor and acceptor moiety can expand the conjugation system for a broader spectral response as well as increase the molar absorption coefficients of the dyes. However, large π-conjugated systems simultaneously result in stronger intermolecular π–π interaction, which leads to unfavorable π-stacked dye aggregation on TiO_2[14] and consequently inefficient electron injection due to the formation of excited triplet states.[22] Among the strategies to suppress the dye aggregation tendency, structural modification with steric groups is considered to be an effective method[23].

5.2.2 Optical Properties

Figure 11a shows the absorption spectra of **Ind-1** and **N3** in ethanol. Absorption peaks (λ_{max}) were observed at 493 and 536 nm in the visible region for **Ind-1** and **N3**, respectively. The molar absorption coefficient of **Ind-1** is determined to be 2.80×10^4 $M^{-1} \cdot cm^{-1}$ at 493 nm, which is nearly 2 times as high as that of **N3** (1.42×10^4 $M^{-1} \cdot cm^{-1}$ at 536 nm). Apparently, the higher ε value of **Ind-1** could be utilized to get a better light-harvesting effect with thinner TiO_2 film. In solid-state dye-sensitized solar cells, a high absorption coefficient is preferred to get better light-harvesting effect with thinner TiO_2 film because of mass transport and insufficient pore filling.[24] Compared with λ_{max} in solvent, both dyes have hypsochromic shifts while adsorbed on TiO_2 (Figure 11b). Furthermore, after anchoring on TiO_2, the absorption threshold of **Ind-1** was red shifted by approximately 50 nm from 650 nm to 700 nm due to the interaction between the carboxylate group and TiO_2,[11] which is advantageous for solar light harvesting.

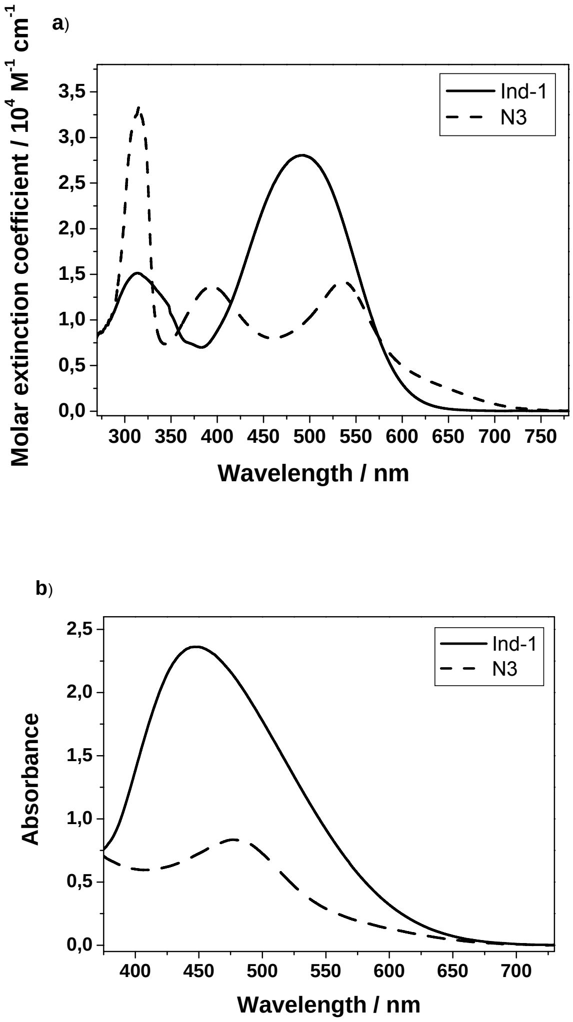

Figure 11. Absorption spectra of **Ind-1** and **N3** in ethanol (a) and on TiO_2 film (b).

5.2.3 Electrochemical Properties

Generally, the LUMO level of sensitizers must be more negative than the conduction band of the TiO_2 electrode to inject electrons, and the HOMO level must be more positive than the HOMO level of HTM to accept electrons and regenerate from the oxidized state.[1] Thus, the electrochemical properties of **Ind-1** were studied to clarify its HOMO and LUMO levels.

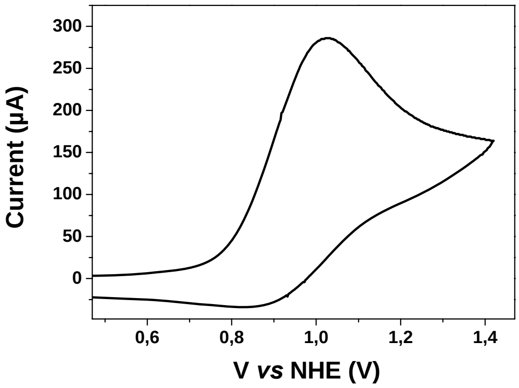

Figure 12. Cyclic voltammetry of **Ind-1** attached to nanocrystalline TiO_2 film.

The bandgap energy of **Ind-1** is estimated from the onset of the absorption spectra of dyes adsorbed on TiO_2, which is determined to be 1.77 V. The oxidation potential corresponding to the HOMO level of **Ind-1** is determined to be 0.92 V, which is more positive than the HOMO level of spiro-OMeTAD (~ 0.8 V vs NHE)[13b] suggesting that the oxidized dye could be regenerated by accepting electrons from spiro-OMeTAD. So the LUMO level of **Ind-1** is calculated to be -0.85 V vs NHE, which is more negative than the conduction band of TiO_2 (~ -0.5 V vs NHE)[13a], providing sufficient thermodynamic driving force for electron injection from the excited dyes to titania.

5.2.4 Photovoltaic Performance

Ind-1 is expected to be a good candidate as a sensitizer in solid-state cells where thinner TiO_2 film is required. Figure 13 shows the photovoltaic performance of **Ind-1** in solid-state dye-sensitized solar cells.

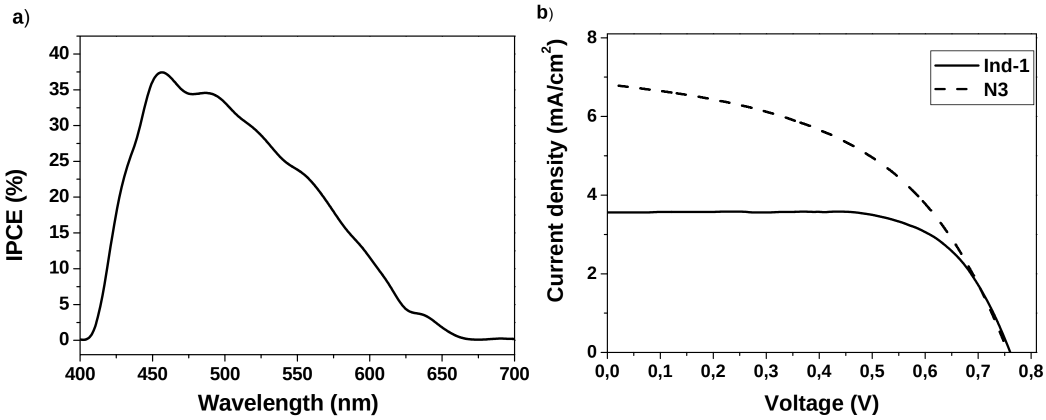

Figure 13. IPCE spectrum (a) and I-V curves (b) of solid-state DSSCs sensitized by **Ind-1** and **N3**.

Due to high light harvesting efficiency of **Ind-1**, the IPCE value exceeded 20% in broad range of 426 ~ 566 nm and reached a maximum of close to 40% at 456 nm, which perfectly matched the absorbance spectrum of dye-loaded TiO_2 film. Figure 14b presents the I-V curves of **Ind-1** and **N3** sensitized solid-state cells. **Ind-1** sensitized cells demonstrated a V_{oc} of 760 mV, a J_{sc} of 3.4 mA/cm^2 and a FF of 0.71, leading to an overall efficiency η of 1.92%, while **N3** produced an efficiency of 2.55% under the same conditions.

Table 2. Photovoltaic performance of solid-state cells sensitized by **Ind-1** and **N3** under one sun light illumination.

Sensitizer	**J_{sc} (mA/cm^2)**	**V_{oc} (mV)**	**FF**	**η (%)**
Ind-1	3.40	760	0.71	1.92
N3	6.81	760	0.48	2.55

As shown in Table 2, it is obvious that the low current is the only reason which cause the lower power efficiency of **Ind-1** based solar cells than that of **N3**-sensitized devices. However, **Ind-1** has broader absorption band and higher absorption coefficient than those of **N3** in the visible region. To further improve the performance of **Ind-1**-sensitized solar cells, one should focus on the improvement of the TiO_2/dye/spiro-MeOTAD interface. It can be realized by using some coadsorbers, which can minimize the charge recombination between TiO_2 and spiro-MeOTAD.[25]

5.2.5 Possibility of Building Molecular Cocktail DSSCs

The efficient combination of two dyes with complementary spectra can achieve higher efficiencies than with each separate dye. In this chapter, two sensitizers were respectively investigated in solid-state dye-sensitized solar cells: **ID176** (dye A) has a maximal absorption at 582 nm, giving an overall conversion efficiency of 2.2%; **Ind-1** (dye B) has a maximal absorption at 493 nm, presenting a solar cell efficiency of 1.9%. Molecular cocktail 'full-spectrum' solar cells can be fabricated from these two dyes to extend the spectral sensitization. (Figure 14)

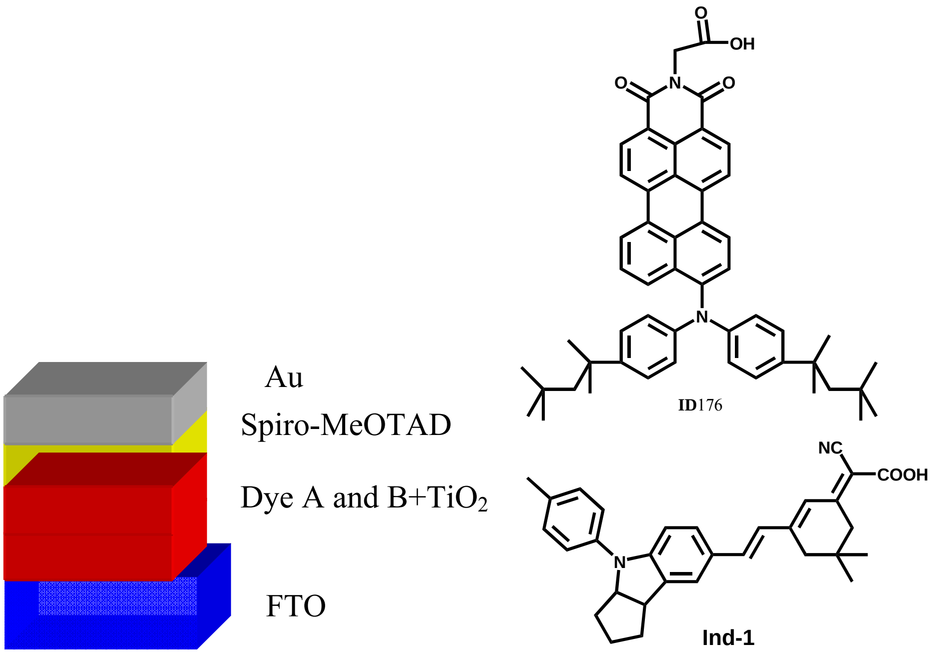

Figure 14. Device layout of molecular cocktail solar cells (left); structure of **ID176** and **Ind-1**

The fabrication of molecular cocktails should be carried out in a systematic way to find out an optimal ratio of A-to-B due to their complementary photoresponse. An optimal molar ratio between dye A and dye B can not only result in a most advantageous absorption intensity and breadth, but also bring out a cooperative effect in two aspects: firstly, the co-adsorption of two dyes may result in a denser coverage on the TiO_2 surface, which inhibits the dark current; secondly, the aggregation behavior of the individual dyes may be varied in co-adsorption conditions, which brings positive effects to their injection efficiencies.[26]

Due to the time limitation, a systematic study on such a molecular cocktail DSSC could not be carried out.

5.2.6 Conclusion

An isophorone dye **Ind-1,** with a high absorption coefficient and a complementary absorption to that of **ID176,** was investigated in solid-state dye-sensitized solar cells. A relatively high efficiency η of 1.92% under one sun light illumination were achieved, with a J_{sc} of 3.4 mA/cm^2, a V_{oc} of 760 mV and a *FF* of 0.71, while **N3** produced an overall conversion efficiency of 2.55% under the same conditions.

The efficient combination of two dyes in a molecular cocktail DSSC should be based on the thorough study of each dye. So, the comprehension on the separate cell is considered to be necessary and helpful for the later fabrication of a ‘full-spectrum’ solar cell.

5.3 References

[1] J.-H. Yum, P. Chen, M. Grätzel, M. K. Nazeeruddin, *ChemSusChem*, **2008**, *1*, 699.

[2] (a) L. Schmidt-Mende, U. Bach, R. Humphry-Baker, T. Horiuchi, H. Miura, S. Ito, S. Uchida, M. Grätzel, *Adv. Mater.* **2005**, *17*, 813; (b) S. Ito, S. M. Zakeeruddin, R. Humphry-Baker, P. Liska, R. Charvet, P. Comte, M. K. Nazeeruddin, P. Pechy, M. Takata, H. Miura, S. Uchida, M. Grätzel, *Adv. Mater.* **2006**, *18*, 1202.

[3] J.-J. Cid, J.-H. Yum, S.-R. Jang, M. K. Nazeeruddin, E. Martinez-Ferrero, E. Palomares, J. Ko, M. Grätzel, T. Torres, *Angew. Chem.* **2007**, *119*, 8510.

[4] (a) H. Langhals, *Nachr. Chem., Tech. Lab.* **1980**, *28*, 716; (b) M. P. O'Neil, M. P. Niemczyk, W. A. Svec, D. Gosztola, G. L. I. Gaines, M. R. Wasielewski, *Science,* **1992**, *257*, 63; (c) M. Sadrai, L. Hadel, R. R. Sauers, S. Husain, K. Krogh-Jespersen, J. D.Westbrook, G. R. Bird, *J. Phys. Chem.* **1992**, *96*, 7988.

[5] S. Ferrere, A. Zaban, B. A. Gregg, *J. Phys. Chem. B,* **1997**, *101*, 4490.

[6] S. Ferrere, B. A. Gregg, *New J. Chem.* **2002**, *26*, 1155.

[7] S. Ferrere, B. A. Gregg, *J. Phys. Chem. B*, **2001**, *105*, 7602.

[8] Y. Shibano, T. Umeyama, Y. Matano, H. Imahori, *Org. lett.* **2007**, *9*, 1971.

[9] T. Edvinsson, C. Li, N. Pschirer, J. Schoeneboom, F. Eickemeyer, R. Sens, G. Boschloo, A. Herrmann, K. Müllen, A. Hagfeldt, *J. Phys. Chem. C,* **2007**, *111*, 15137.

[10] (a) H. Han, U. Bach, Y.-B. Cheng, R. A. Caruso, C. MacRae, *Appl. Phys. Lett.* **2009**, *94*, 103102-1; (b) L. Schmidt-Mende, S. M. Zakeeruddin, M. Grätzel, *Appl. Phys. Lett.* **2005**, *86*, 013504; (c) G. Kron, T. Egerter, J. H. Werner, and U. Rau, *J. Phys. Chem. B*, **2003**, *107*, 3556; (d) B. Li, L. D. Wang, B. N. Kang, P. Wang, and Y. Qiu, *Sol. Energy Mater. Sol. Cells*, **2006**, *90*, 549.

[11] M. K. Nazeeruddin, A. Kay, I. Rodicio, R. Humphry-Baker, E. Mueller, P. Liska, N. Vlachopoulos, M. Grätzel, *J. Am. Chem. Soc.* **1993**, *115*, 6382.

[12] (a) T. Dentani, K. Funabiki, J.-Y. Jin, T. Yoshida, H. Minoura, M. Matsui, *Dyes & Pigments* **2007**, *72*, 303; (b) C. Zafer, M. Kus, G. Turkmen, H. Dincalp, S. Demic, B. Kuban, Y. Teoman, S. Icli, *Sol. Energy Mater. Sol. Cells,* **2007**, *91*, 427.

[13] (a) A. Hagfeldt, M. Grätzel, *Chem. Rev.* **1995**, *95*, 49; (b) U. B. Cappel, E. A. Gibson, A. Hagfeldt, G. Boschloo, *J. Phys. Chem. C.* **2009**, *113*, 6275.

[14] M. K. Nazeeruddin, P. Pechy, T. Renouard, S. M. Zakeeruddin, R. Humphry-Baker, P. Comte, P. Liska, L. Cevey, E. Costa, V. Shklover, L. Spiccia, G. B. Deacon, A. Kay, C. A. Bignozzi, M. Grätzel, *J. Am. Chem. Soc.* **2001**, *123*, 1613.

[15] (a) K. R. J. Thomas, Y.- C. Hsu, J. T. Lin, K.- M. Lee, K.- C. Ho, C.- H. Lai, Y.- M. Cheng, P.- T. Chou, *Chem. Mater.* **2008**, *20*, 1830; (b) Q. Li, L. Lu, C. Zhong, J. Huang, Q. Huang, J. Shi, X. Jin, T. Peng, J. Qin, Z. Li, *Chem. Eur. J.* **2009**, *15*, 9664; (c) D. P. Hapberg, T. Edvinsson, T. Marinado, G. Boschloo, A. Hagfeldt, L. Sun, *Chem. Commun.* **2006**, 2245.

[16] (a) P. Chen, J. H. Yum, F. D. Angelis, E. Mosconi, S. Fantacci, S.-J.Moon, R. H. Baker, J Ko, M. K. Nazeeruddin, M. Grätzel, *Nano Lett*. **2009**, *9*, 2487; (b) M. Grätzel, *Accounts of Chemical Research*, **2009**, *42*, 1788; (c) A. Furube, M. Murai, S. Watanabe, K. Hara, R. Katoh, M. Tachiya, *J. Photochem. Photobiol. A Chem.* **2006**, *182*, 273; (d) J. Krüger, Ph.D Thesis, EPFL (Switzerland), **2003.**

[17] (a) O. Kohle, M. Grätzel, A. E. Meyer, T. B. Meyer, *Adv. Mater.* **1997**, *9*, 904; (b) K. Sayama, S. Tsukagoshi, K. Hara, Y. Ohga, A. Shinpou, Y. Abe, S. Suga, H. Arakawa, *J. Phys. Chem. B,* **2002**, *106,* 1363; (c) K. Hara, Y. Tachibana, Y. Ohga, A. Shinpo, S. Suga, K. Sayama, H. Sugihara, H. Arakawa, *Sol. Energy Mater. Sol. Cells*, **2003**, *77*, 89; (d) K. Hara, T. Sato, R. Katoh, A. Furube, T. Yoshihara, M. Murai, M. Kurashige, S. Ito, A. Shinpo, S. Suga, H. Arakawa, *Adv. Funct. Mater.* **2005**, *15*, 246; (e) Q. Yu, S. Liu, M. Zhang, N. Cai, Y. Wang, P. Wang, J. Phys. Chem. C, 2009, 113, 14559.

[18] Y. Chen, Z. Zeng, C. Li, W. Wang, X. Wang, B. Zhang, *New J. Chem.* **2005**, 29, 773.

[19] B. Liu, W. Zhu, Q. Zhang, W. Wu, M. Xu, Z. Ning, Y. Xie, H. Tian, *Chem. Commun.* **2009**, 1766.

[20] P. Leriche, P. Frère, A. Cravino, O. Alévêque and J. Roncali, *J. Org. Chem.* **2007**, *72*, 8332.

[21] S. Roquet, A. Cravino, P. Leriche, O. Alévêque, P. Frère and J. Roncali, *J. Am. Chem. Soc.* **2006**, *128*, 3459.

[22] D. P. Hagberg, T. Marinado, K. M. Karlsson, K. Nonomura, P. Qin, G. Boschloo, T. Brinck, A. Hagfeldt, L.-C. Sun, *J. Org. Chem.* **2007**, *72*, 9550.

[23] (a) K. Hara, T. Sato, R. Katoh, A. Furube, Y. Ohga, A. Shinpo, S. Suga, K. Sayama, H. Sugihara, H. Arakawa, *J. Phys. Chem. B*, **2003**, *107*, 597; (b) Z.-S. Wang, N. Koumura, Y. Cui, M. Takahashi, H. Sekiguchi, A. Mori, T. Kubo, A. Furube, K. Hara, *Chem. Mater.* **2008**, *20*, 3993; (c) Z.-J. Ning, Q. Zhang, W.-J. Wu, H.-C. Pei, B. Liu, H. Tian, *J. Org. Chem.* **2008**, *73*, 3791.

[24] E. M. Barea, R. Caballero, F. Fabregat-Santiago, P. D. L. Cruz, F. Langa, J. Bisquert, *ChemPhysChem*, **2010**, *11*, 245.

[25] J. Jasieniak, M. Johnston, E. R. Waclawik, *J. Phys. Chem. B,* **2004**, *108*, 12962.

[26] W. Wu, F. Meng, J. Li, X. Teng, J. Hua, *Synth. Met.* **2009**, *159*, 1028.

Chapter 6 Experimental Part

The techniques utilized in this thesis and their relevant theoretical background are described in this chapter. The performance of solar cells was tested by photovoltaic techniques, including current-voltage characteristics and incident-light-to-current conversion efficiency (IPCE). Optical and spectroscopic methods were also used to investigate the materials' characteristics for solar cells.

6.1 Device Preparation

6.1.1 Organic Bulk-heterojunction Solar Cells

The fabrication of organic bulk-heterojunction solar cell consists of the following steps:

-- Etching of the ITO glass,
-- Cleaning of the substrate,
-- Spin-coating and heating of the PEDOT-PSS layer,
-- Spin-coating of the organic active layer,
--Evaporation of the top electrode.

Etching of the ITO glass. Indium tin oxide (ITO, or tin-doped indium oxide) is a mixture of indium oxide In_2O_3 and tin oxide SnO_2, typically 90% In_2O_3 and 10% SnO_2 by weight. It is transparent in thin layers and highly conductive, with an area resistance value below 20Ω/sq at a thickness of 100 nm. The combination of transparency and conductivity makes ITO the most widely used electrode in photovoltaics.

To prevent direct contact between the two electrodes and also to define the working area of a solar cell device, part of the conducting area is needed to be chemically etched by using Scotch tape to mask certain area. The normal way to pattern ITO is to etch off the oxide using hydrochloric acid in the following procedures:

1. Ultrasonicate the partly protected ITO glass in a water bath with zinc powder (Aldrich, CAS 7440-66-6, 99.998%) for ~5-10 min.
2. Pour the water out, add HCl (2M), and ultrasonicate in a bath for 2 min.
3. Wash with water to dissolve the salts produced.

Cleaning of the substrate was done by successive washing twice with acetone, and then with isopropanol in an ultrasonic bath for 10 min each. The substrate was further cleaned in oxygen plasma for 10 min just before the spin-coating procedure.

Spin-coating and heating of the PEDOT-PSS layer. A conducting layer of PEDOT:PSS (Clevios P) was spin-cast (5000 rpm) with thickness of about 40 nm from aqueous solution. The substrates were dried at 150 °C for 10min in air, and then moved into a glove-box for spin-casting of the photoactive layer.

Spin coating of the organic layer was done in a glove box to protect the organic material from all kinds of oxidation or degradation upon contact with water or oxygen. The solutions were prepared at a concentration of 5-20 mg/ml in chloroform, toluene, or chlorobenzene according to the solubility of the material and the thickness required. To prevent any dust or impurities, the solutions were filtered through a 0.45 μm hydrophobic filter (Fisher, Millex 4 mm, PTFE) before spin-coating.

Evaporation of the top electrode was accomplished by evaporating silver or aluminium on top of the organic layer through a mask. The effective area of the device was approximately 6 mm^2 defined by overlap of etched ITO and the top electrode, which was accurately measured by an optical microscope for subsequent calculations of cell efficiency. The evaporation was performed in an Edwards FL400 electron-beam evaporator (Boc. Edwards, Sussex, UK) at an evaporation rate of 5 nm/s.

Device fabrication of triangle-shaped discotics 3-based BHJ cells. The photovoltaic devices consisted of indium tin oxide (ITO)/(**3**+PDI)/Ag. The chloroform solution of **3**/PDI (15mg/mL, ratios of 2:8, 4:6, 5:5, and 6:4) was spin-coated onto ITO substrates which were pre-treated with acetone and isopropyl alcohol in an ultrasonic bath. A 100 nm thick Ag layer was then evaporated as the top electrode. Before the measurement, the samples were annealed at 120 °C for 1h under a nitrogen atmosphere in order to self-organize the thin films.

Device fabrication of PBTT-based BHJ cells. The patterned ITO substrates were first cleaned with acetone and isopropyl alcohol in an ultrasonic bath, followed by a cleaning treatment for 10 min with oxygen plasma. Subsequently, a conducting layer of PEDOT:PSS (Clevios P) was spin-cast (5000 rpm) with a thickness of about 40 nm from aqueous solution. The substrates were dried at 150 °C for 10min in air, and then moved into a glove-box for spin-casting of the photoactive layer. The active layers were fabricated from the dichlorobenzene solutions of PBTT and [70]PCBM blend in different weight ratios of 1:1, 1:2 and 1:3, with or without 1,8-octanedithiol (24 mg/mL) as the processing additive. In the case that the D/A ratio is 1:2, the dichlorobenzene solution comprising PBTT (8 mg/mL) and [70]PCBM (16 mg/mL), with 1,8-octanedithiol (24 mg/mL) as the processing additive. The blend solution was then spin-cast at 700 rpm on top of the PEDOT:PSS layer. A silver layer (ca. 100 nm) was subsequently evaporated through a mask onto the surface to form the cathode. The post-deposition annealing process was carried out on the same sample every two minutes in a stepwise fashion ending up with a total thermal treatment period of 14 minutes.

6.1.2 Solid-state Dye-sensitized Solar Cells

The fabrication of solid-state dye-sensitized solar cells comprises of the following steps:

-- Etching of the FTO glass,
-- Cleaning of the substrate,
-- Compact TiO_2 layer,
-- Nanocrystalline TiO_2 layer,
-- Dye adsorption,
-- Deposition of spiro-MeOTAD,
-- Evaporation of the top electrode.

Etching of the FTO glass. In this study, a 1.1 mm thick aluminoboro-silicate glass coated on one side with a fluorine doped tin oxide (SnO_2:F) layer ("FTO" glass, Solaronix) was utilized in the solid-state dye-sensitized solar cells. The sheet resistance of the FTO layer is ~10 ohm/square and its transmission is > 80% from 500 to 800 nm. The chemical etching is carried out in the same way as that for ITO glass.

Cleaning of the substrate. The structured FTO glass was cleaned subsequently in various solvents (1 x acetone, 2 x ethanol, 1 x Hellmanex (2% in H_2O), 3 x H_2O, 2 x ethanol) in an ultrasonic bath for 10 min each. Cleaned substrates were stored in pure ethanol. The substrate was further cleaned in oxygen plasma for 10 min just before the spin-coating procedure.

Compact TiO_2 layer. The sol-gel precursor was prepared in the following procedures: a volume of 250 μl of Mili-Q water was added to 10 ml of ethanol; the resulting solution was acidified to a PH between 1 and 2 with concentrated HNO_3 after which 750 μl of titanium isopropoxide (Aldrich, 97%) was added at room temperature in a glove box under inert atmosphere conditions; the precursor solution was typically left to stir for 3 days.

Then, the sol-gel precursor solution was deposited by spin-coating onto the FTO glass, followed by the processes of air drying for 0.5 hour and calcination at 200 °C for 1 hour.

Nanocrystalline TiO_2 layer was done by doctor-blading the nanocrystalline titanium dioxide paste " Ti-Nanoxide T " (Solaronix) on top of compact TiO_2 layer. The paste contains about 11% wt. nanocrystalline titanium dioxide (anatase particles: 13 nm) in ethanol, water and organic binders.

In a doctor-blade machine, a few drops of TiO_2 paste were uniformly placed on the substrate plate, and then the blade was slidden over the plate to spread and distribute the material. Films of different thickness can be fabricated by adjusting the distance between the doctor-blade and the substrate surface. The optimal film thickness in the corresponding device has to be decided by the photovoltaic performance of a specific sensitizer.

After the coating step the films were allowed to dry in air for about 30 min at room temperature in a dust free container. The layers were then calcinated to remove organic additives and to sinter particle to a mechanically adhering and electrically conducting film.

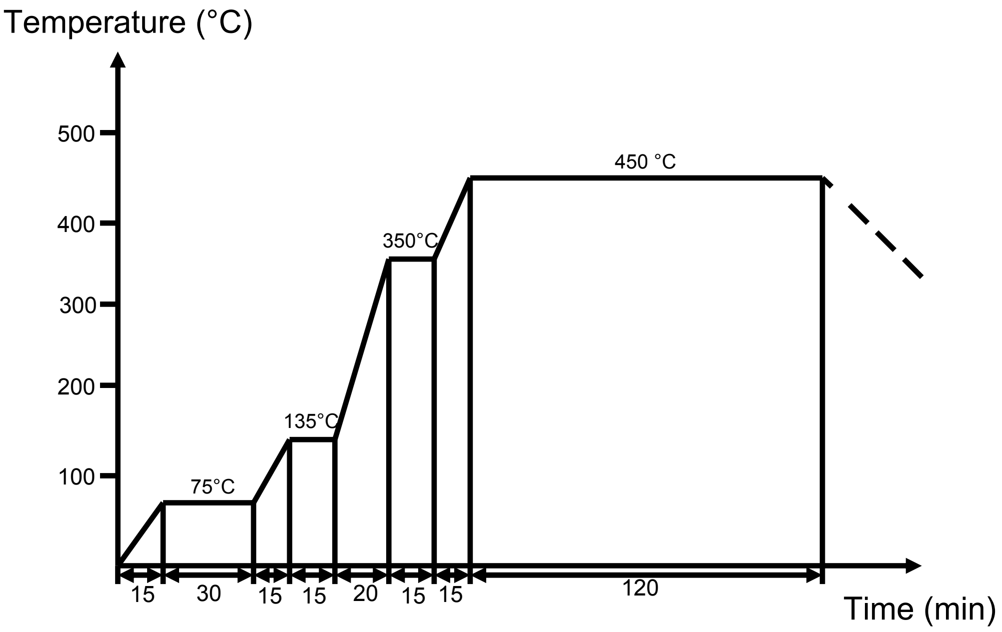

Figure 1. Sintering program for doctor-bladed nanocrystalline TiO_2 films

To obtain reproducible grain growth and phase transformation during the sintering, a special sintering program was carried out with few alterations based on the literature.[1] The program (Figure 1) consists of heat ramps and isotherms to separate the combustion of the additives and the sintering in time. The upper sintering temperature is 450 °C, which is determined by the physical properties of the substrate. It was reported that the firing atmosphere affects the doping of the TiO_2 and the best results for the TiO_2 colloids can be obtained by sintering in dry air.[2] The films after sintering appears to be highly transparent.

Dye adsorption. The nanocrystalline TiO_2 film was immersed in the corresponding dye solution for certain hours to achieve the equilibrium between dye adsorption and desorption.

Deposition of spiro-MeOTAD. After the immersion for certain hours, the substrates were taken out of the dye solution. Then the substrates were washed with the same solvents used for the dye solution, and dried under a nitrogen flow.

The hole conductor matrix was a solution of spiro-MeOTAD (0.15M) in chlorobenzene, containing $Li(CF_3SO_2)_2N$ (30mM), 4-*tert*-butylpyridine (0.11M) and $N(PhBr)_3SbCl_6$ (0.4mM). Then the hole conductor matrix was spin-coated onto the dye-adsorbed substrates.

Evaporation of the top electrode. A gold layer of 100 nm was deposited as top electrode. A metal mask was used to define the active area of the device.

Device fabrication of ID176-based solid-state DSSCs. The solid-state dye-sensitized solar cells were fabricated in the following steps: SnO_2: F glass (FTO, purchased from Solaronix SA) was ultrasonicated with acetone, ethanol, Helmanex, H_2O and ethanol successively, then finally cleaned by an oxygen plasma for 10 mins. The TiO_2 barrier layer was prepared from a sol-gel solution on FTO glass. A nanostructured TiO_2 layer was fabricated via doctor-blading the TiO_2 paste (Ti-Nanoxide T, Solaronix), followed by the calcination at 450 °C. **ID176** was absorbed to the TiO_2 film by immersion overnight in a $3X10^{-4}$ mol/L solution in o-xylene or n-butanol, DMSO, dichloromethane (DCM): Hexane (1:3) and DCM: CH_3CN (1:3), respectively. The substrate immerged in the o-xylene solution was then rinsed by o-xylene, and the one in n-butanol was cleaned by n-butanol. The rest may be deduced by analogy. The hole conductor matrix was applied by spin coating of a solution of spiro-MeOTAD (0.15 M) in chlorobenzene, containing $Li(CF_3SO_2)_2N$ (30 mM), 4-*tert*-butylpyridine (0.11 M) and $N(PhBr)_3SbCl_6$ (0.4 mM). Finally a gold contact of 40 nm was deposited by evaporation.

Device fabrication of Ind-1-based solid-state DSSCs The SnO_2: F glass (FTO) was ultrasonicated with acetone, ethanol, Helmanex in sequence, then finally cleaned by an oxygen plasma for 10mins. Then the sol-gel solution was spin coated in ambient conditions on FTO glass to make a TiO_2 barrier layer. A nanostructured TiO2 layer was fabricated via doctor-blading the TiO_2 paste, followed by the calcination at 450°C. Dyes were adsorbed to the TiO_2 film by immersion overnight in a 3X10-4 mol/L solution in acetonitrile and subsequently rinsed by ethanol. The hole conductor matrix was applied by spin coating of a solution of spiro-MeOTAD in chlorobenzene, containing $Li(CF_3SO_2)_2N$, tBP and $N(PhBr)_3SbCl_6$. Finally a gold contact of 40 nm was deposited by evaporation.

6.2 Device Testing Setup

The devices were tested in an ambient atmosphere of nitrogen. Two incident light sources were used in the testing, one is a halogen lamp source (A lampenhaus of model LSH-T100 housing a halogen lamp of 12 V, 100 W) with monochromator (Jobin Yvon GmbH, Triax 180) wavelength varying from 300 nm to 800 nm with maximum light intensity of 6 W/m^2 at ca. 600 nm; and the other was a simulated solar light (Lichttechnik, Germany) using a 575 W metal halide lamp, in combination with an ODF filter, to produce a spectral distribution close to the global radiation AM 1.5G. The light intensity of the simulated solar light was set to 1000 W/m^2.

Incident light was focused on the effective area of each device through a lens. Current-wavelength (I-λ) curves and current-voltage (I-V) curves are recorded with a Keithley 236 Source-Measure Unit (Keithley Instruments Inc., USA). Two standard silicon diodes with known current-light intensity relationship were used to calibrate the incident light intensity: one for the calibration of the monochromatic light within the spectrum range from 300 nm to 800 nm; the other for the calibration of the simulated solar light with measuring range of 50~1000 W/m^2. The testing system is shown in Figure 2.

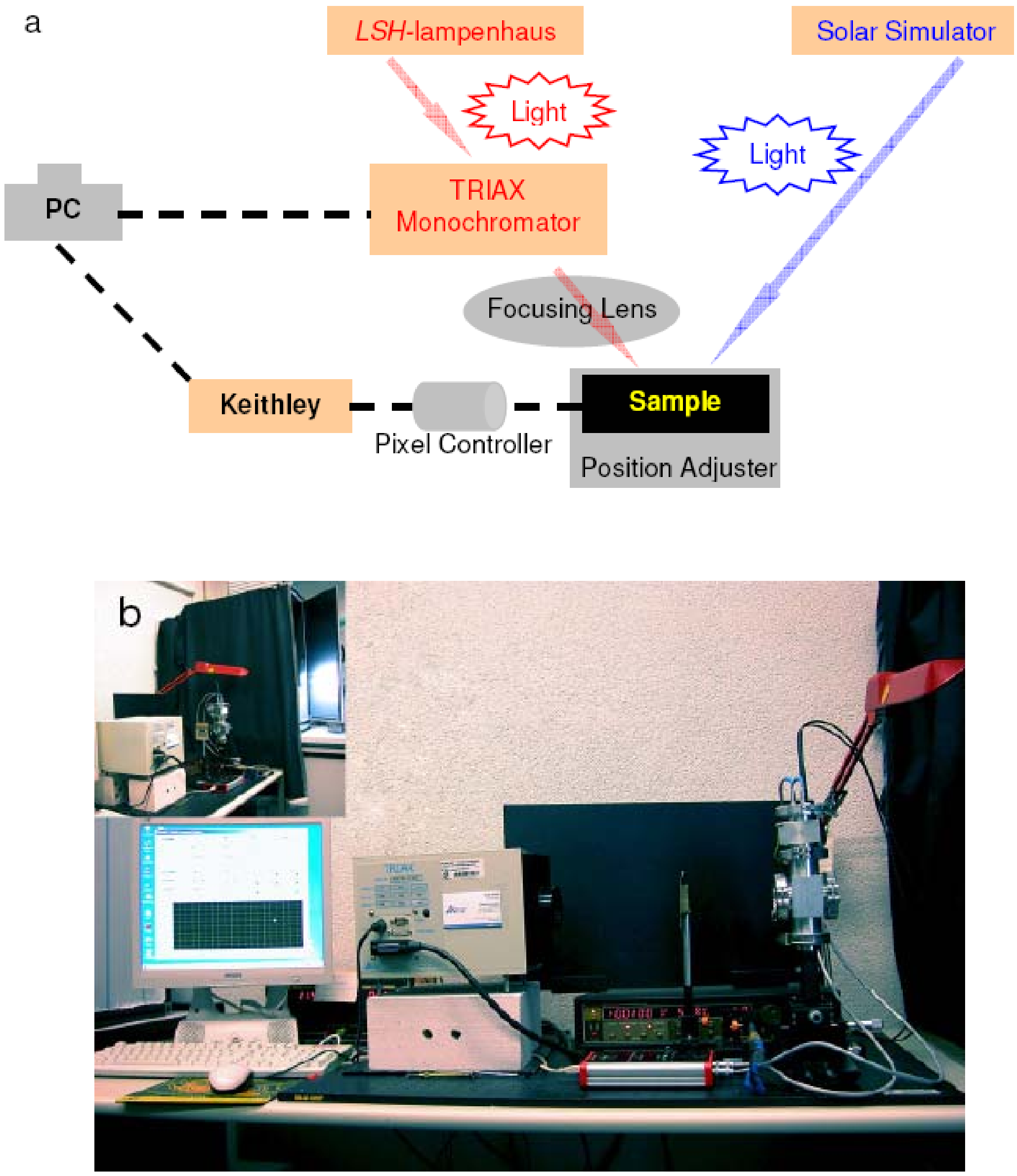

Figure 2. Scheme (a) and a photograph (b) of the testing system utilized in the thesis.

6.3 Absorption Spectroscopy

The ultraviolet-visible absorption spectroscopy is used for the detection and quantitative measurement of chromophores that undergo electronic transitions between different vibrational levels of the ground and excited states. The UV/vis spectrophotometer measures the intensity of light passing through a sample (I), and compares it to the intensity of light before it passes through the sample (I_o). The absorbance is expressed by using the Beer-Lambert law:

$$A = -\log_{10}(I / I_0) = \varepsilon c L$$

where A is the measured absorbance, I_0 is the intensity of the incident light at a given wavelength, I is the transmitted intensity, L is the path length through the sample, and c *is* the concentration of the absorbing species. For each species and wavelength, ε is a constant known as the molar absorptivity, which is a fundamental molecular property in units of $\mathrm{Lmol^{-1}cm^{-1}}$.

An ultraviolet-visible spectrum is a graph of light absorbance versus wavelength in a range of ultraviolet or visible regions. The UV/vis spectrophotometer used here is a Perkin Elmer, Lambda 900 spectrometer.

6.4 Cyclic Voltammetry (CV)

Cyclic voltammetry (CV) is used to characterize how easily a compound is able to lose or accept an electron (i.e. undergo oxidation or reduction). Cyclic voltammetry measures the current (rate of electron flow) versus a varying applied potential (voltage or energy of electrons). The applied potential is the difference in energy of the working and reference electrodes, measured in volts (V) or millivolts (mV).

Electrochemical processes usually take place at the electrode-solution interface. A three electrode cell (working, reference, counter) is commonly used in controlled-potential experiments like CV. The reaction under study occurs at the working electrode. Another inert conducting material (e.g. platinum) is normally counter electrode to close the electric circuit. The reference electrode (e.g. Ag/AgCl) provides a stable potential to refer the potential of the working electrode. Electrochemical measurements are carried out in a solvent containing the analyte and a supporting electrolyte.

The choice of the solvent depends on the solubility and the redox activity of the analyte. Commonly used non aqueous solvents for organic materials are acetonitrile, dichloromethane and tetrahydrofurane. Inert supporting electrolytes are necessary to decrease the resistance of the solution, to eliminate electromigration effects and to ensure a constant ionic strength.

The HOMO and LUMO levels of organic thin films can be calculated from the onset values of the oxidation peak in the positive scan and the reduction peak in the negative scan. The energy offset between the HOMO and LUMO levels E_g is the bandgap of polymers.

$$\mathrm{HOMO} = (E_{\mathrm{FOC}} - E_{\mathrm{ons}}^{\mathrm{ox}} + E_{\mathrm{FOC}}^{measure})\ \mathrm{eV} = -(E_{\mathrm{ons}}^{\mathrm{ox}} + 4.8)\ \mathrm{eV}$$
$$\mathrm{LUMO} = (E_{\mathrm{FOC}} - E_{\mathrm{ons}}^{\mathrm{red}} + E_{\mathrm{FOC}}^{measure})\ \mathrm{eV} = -(E_{\mathrm{ons}}^{\mathrm{red}} + 4.8)\ \mathrm{eV}$$
$$E_g = |\mathrm{HOMO} - \mathrm{LUMO}|\ \mathrm{eV}$$

Here, E_{FOC} is the standard potential energy level of ferrocene/ferrocenium (FOC), Fc/Fc^+ redox couple, with a value of -4.8 eV with respect to the vacuum level, which has been defined as zero. $E_{\mathrm{ons}}^{\mathrm{ox}}$ and $E_{\mathrm{ons}}^{\mathrm{red}}$ are the onset values extracted from the CV data as shown in Figure 3. $E_{\mathrm{FOC}}^{measure}$ is the potential value measured under the same conditions, as the calibration standard for the system.

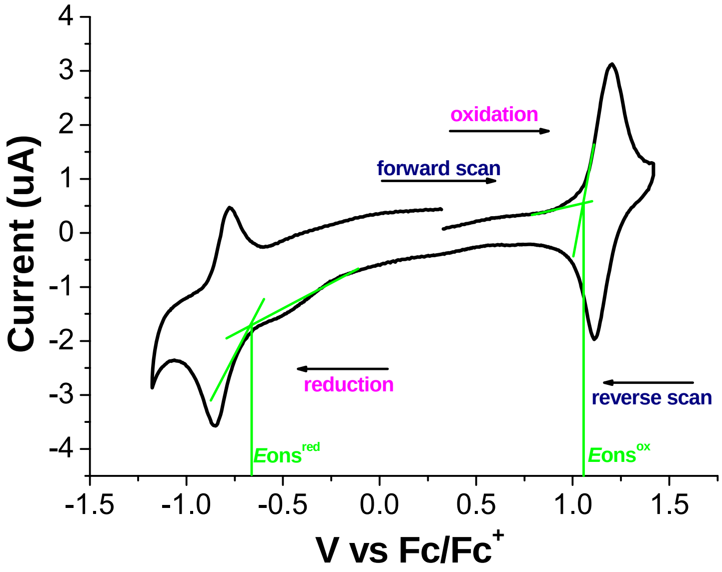

Figure 3. CV curve of oxidation and reduction process

The measurements were performed on a voltametric analyzer (AutoLab PGSTAT-30, Potentiostat/Galvanostat) in a three-electrode cell with a working electrode of ITO glass (sheet resistance of 20Ω/square), a silver quasi-reference electrode (AgQRE, calibrated with the Fc/Fc^+ redox couple E° = -4.8 eV) and a Pt counter electrode. All potentials are referenced against FOC as internal standard. Films were spin-coated on the pre-treated ITO glass. Tetrabutylammonium perchlorate ($TBAClO_4$, 0.1 M), and acetonitrile were used as the electrolyte and solvent, respectively.

6.5 Microscopic Techniques

6.5.1 Atomic Force Microscopy

Atomic force microscope (AFM), also known as scanning force microscopy (SFM), is a very high-resolution type of scanning probe microscopy, with demonstrated resolution of fractions of a nanometer. It operates by measuring the attractive or repulsive forces between a tip and the sample surface.

In AFM, the tip is mounted on a reflective cantilever (the cantilever and tip together are known as the probe). Tip and cantilever are microfabricated and made of silicon nitride, silicon oxide or pure silicon with standard techniques used in semiconductor industry. The deflection of the tip is measured by a laser, reflected off the cantilever onto a split photodiode (Figure 4). This allows vertical and horizontal measurements of the cantilever bending. The vertical deflection data tells us about the interaction between the tip and the sample.[3]

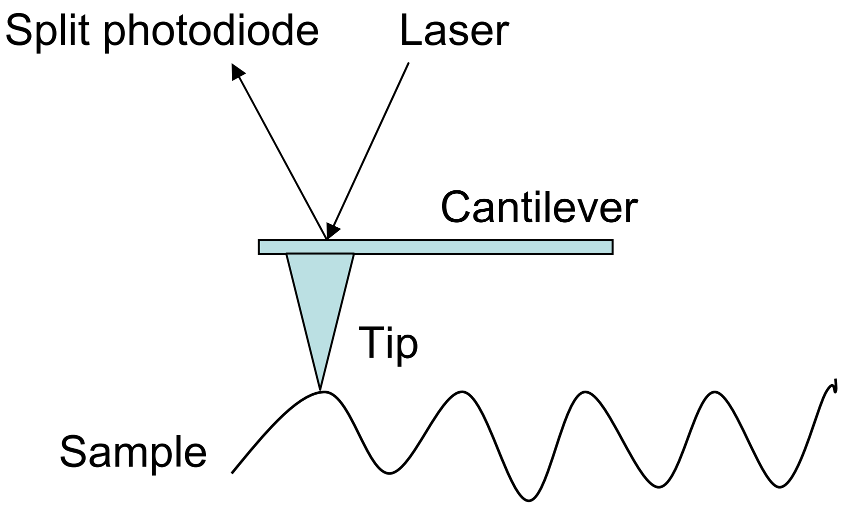

Figure 4. Principle of atomic force microscope.

Based on the sample surface-tip interaction, there are three operation modes: contact mode, non-contact mode and tapping mode. In contact mode, the tip constantly contacts the sample surface and scans across the surface. The contact mode microscopy can give an accurate image with high resolution, but both the sample and tip may be damaged due to the direct contact. Such damage can be avoided by using non-contact mode; however, the resolution level is decreased. Hence, the tapping mode, a combination of contact and non-contact mode, appears to be a solution to this problem. In tapping mode, the tip is alternatively placed in contact with the surface to provide high resolution and then lifting the tip off the surface to avoid dragging the tip across the surface.[4] The cantilever oscillates close to or at the resonant frequency with an amplitude between 20 nm and 100 nm.

In this work, tapping mode AFM (Multimode and Dimension 3100, Veeco) was used. The Dimension 3100 microscope combines AFM and scanning tunneling microscopy (STM), which differs from AFM in that it measures the tunneling current between the tip and the surface. In the microscopes of Dimension (trademark) series, the samples remain stationary while the probe scans back and forth above them. Without limitation of the piezoelectric support, the dimensions of the sample can vary from millimeters to centimeters. The tapping mode cantilever is produced by Olympus, with type number OMCLAC 160 TS-W2 silicon. The observed samples were spin-coated on silica or ITO glass.

6.5.2 Scanning Electron Microscopy (SEM)

In SEM, a beam of electrons is produced at the top of the microscope by heating of a metallic filament. The electron beam follows a vertical path through electromagnetic lenses which focus and direct the beam down towards the sample. Once the beam hits the sample, other electrons (backscattered or secondary) are ejected from the sample and collected by detectors for the conversion to an image with great depth of field and an almost three-dimensional appearance (Figure 5).[5]

In this study, SEM (LEO 1530 Gemini) was performed to observe both the surface and the internal morphology of thin films. The films were spin-coated onto silica wafers.

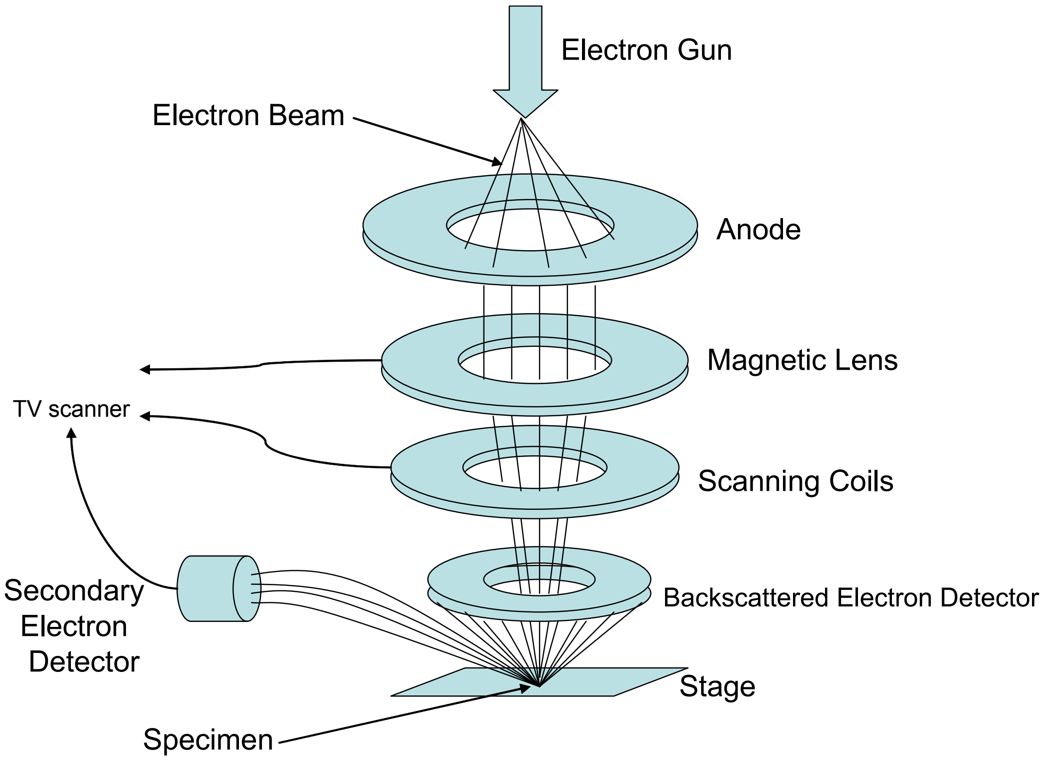

Figure 5. Operating principle of scanning electron microscopy.

6.6 X-ray

6.6.1 2D-WAXS measurements

X-rays are generated in cathode-ray tubes when high-energy electrons impinge on metal targets. When X-rays are focused on a polymer sample (in pellet or cylinder form), two types of scattering occur. If a sample is crystalline, the X-rays are scattered coherently, that is, there is no change in wavelength or phase between the incident and scattered rays. If the sample has a nonhomogeneous morphology, the scattering is incoherent and there is a change in both wavelength and phase. Coherent scattering is determined by wide-angle measurements (WAXS) and incoherent scattering by small-angle measurements (SAXS).

The WAXS is usually applied to investigate the self-organization of organic materials. This diffraction pattern consists of a series of concentric cones arising from scattering by the crystal planes; it is recorded as concentric rings on the X-ray plate superimposed on a diffuse background of incoherent scatter. As the degree of crystallinity increases, the rings become more sharply defined, and if the crystallites are oriented (e.g. by drawing), the circles give way to a pattern of arcs and spots more nearly resembling diffraction patterns of low-molecular-weight crystalline compounds. Information on crystal dimensions, degree of crystallinity, and so on, can be gained from the diffraction patterns.

2D-WAXS measurements of oriented fibers were conducted using a rotating anode (Rigaku, 18kw) X-ray beam (Cu Kα, pinhole collimation, double graphite monochromator) with the beam perpendicular to the fiber axis and a CCD camera.[6]

6.6.2 X-ray Diffraction

X-ray diffraction (XRD) is a versatile, non-destructive technique that reveals detailed information about the chemical composition and crystallographic structure of natural and manufactured materials.[7]

A polymer can be considered partly crystalline and partly amorphous. The crystallinity parts give sharp narrow diffraction peaks and the amorphous component gives a very broad peak. The ratio between these intensities can be used to calculate the amount of crystallinity in the material. Based on the principle of X-ray diffraction, a wealth of structural, physical and chemical information about the material investigated can be obtained.

A crystal lattice is a regular three-dimensional distribution (cubic, rhombic, etc.) of atoms in space. These are arranged so that they form a series of parallel planes separated from one another by a distance *d*, which varies according to the nature of the material. For any crystal, planes exist in a number of different orientations - each with its own specific d-spacing.

When a monochromatic X-ray beam with wavelength λ is projected onto a crystalline material at an angle theta, diffraction occurs only when the distance traveled by the rays reflected from successive planes differs by a complete number n of wavelengths.

By varying the angle theta, the Bragg's Law conditions are satisfied by different *d*-spacings in polycrystalline materials. Plotting the angular positions and intensities of the resultant diffracted peaks of radiation produces a pattern, which is characteristic of the sample.

Through X-ray diffraction (XRD) measurements, the related lattice constant *d* can be calculated using Bragg’s law as shown below:

$$2d \sin\theta = n\lambda$$

where λ is the wavelength of incident beam, *n* is the interference order, 2θ is the angle between incident and scattered X-ray wave vectors, and *d* is the spacing between the planes in the atomic lattice.

Bragg's Law, derived by William Lawrence Bragg, is the result of experiments into the diffraction of X-rays or neutrons off crystal surfaces at certain angles.[8] It is supposed that a single monochromatic wave (of any type) is incident on aligned planes of lattice points, with separation *d*, at angle θ, as shown below in Figure 6.

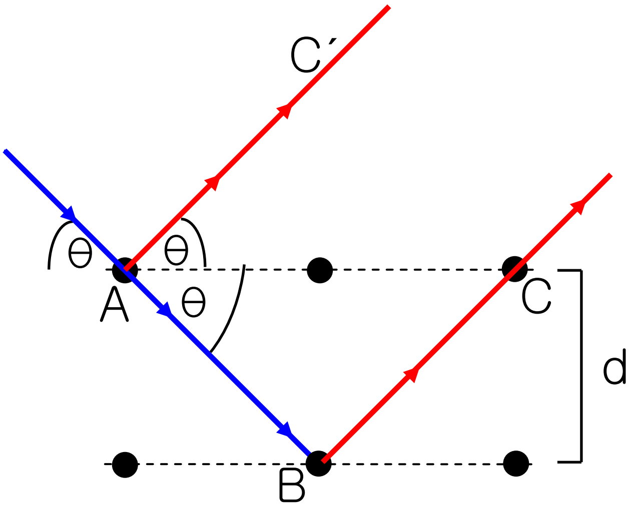

Figure 6. Monochromatic wave incident on aligned planes of lattice points

There will be a path difference between the ray that gets reflected along **AC´** and the ray that gets transmitted, then reflected, along **AB** and **BC** respectively. The path difference is

$$(AB + BC) - (AC')$$.

The two separate waves will arrive at a point with the same phase, and hence undergo constructive interference, if and only if this path difference is equal to any integer value of the wavelength, i.e.

$$(AB + BC) - (AC') = n\lambda.$$

Obviously,

$$AB = BC = d/\sin\theta, \quad AC = 2d/\tan\theta,$$

and

$$AC' = \mathrm{AC} \cdot \cos\theta = (2d/\tan\theta) \cdot \cos\theta = (2d \cdot \cos^2\theta)/\sin\theta$$

So, $n\lambda = (d/\sin\theta + d/\sin\theta) - (2d \cdot \cos^2\theta)/\sin\theta$

Then it is the Bragg's law,

$$n\lambda = 2d/\sin\theta - (2d \cdot \cos^2\theta)/\sin\theta = 2d \cdot (1 - \cos^2\theta)/\sin\theta = 2d \cdot \sin\theta$$

X-ray diffraction experiments were performed using a Siemens D 500K Kristalloflex with a graphite-monochromized Cu Kα X-ray beam, emitted from a rotating Rigaku RV-300 anode.

6.7 Differential Scanning Calorimetry (DSC)

Differential scanning calorimetry is used for quantitative studies of thermal transitions in polymers, in which a polymer sample and an inert reference are heated, usually in a nitrogen atmosphere, and thermal transitions in the sample are detected and measured.[6] The sample holder most commonly used is a very small aluminum cup (gold or graphite is used for analysis above 800 °C), and the reference is either an empty cup or a cup containing an inert material, such as anhydrous alumina. Sample sizes vary from 0.5 to about 10 mg.

The powder sample was measured by Mettler DSC 30 with heating rate 10 K/min in the range from -150 °C to 300 °C. This method combined with polarized optical microscopy (POM, Zeiss Axiophot optical microscope with a nitrogen flushed Linkam THM 600 hot stage) and X-ray is used to determine the phase changes within the material.

6.8 References

[1] J. Krüger, Ph.D thesis, EPFL, **2003**.

[2] A. Kay, Ph.D thesis, EPFL, **1994**.

[3] http://afmhelp.com

[4] S. Ramakrishna, *et al.*, *An Introduction to Electrospinning and Nanofibers,* World Scientific Publishing Co. Pte. Ltd., Singapore, **2005**.

[5] http://mse.iastate.edu/microscopy/path2.html

[6] J. Li, Ph.D thesis, MPIP (Germany) **2006**.

[7] http://www.panalytical.com

[8] http://en.wikipedia.org/wiki/Bragg’s law

Chapter 7 Conclusion and Outlook

7.1 Conclusion

In this thesis, new materials have been investigated in the corresponding device architectures, bulk-heterojunction solar cells and solid-state dye-sensitized solar cells. By applying the self-organizable materials, discotic graphene molecules and a conjugated polymer, in combination with suitable acceptors in the bulk-heterojunction solar cells, it has been found that the enhanced molecular order upon thermal annealing is favorable for good photovoltaic performance. In the solid-state DSSCs, two novel organic sensitizers were investigated respectively and the devices performed efficiently due to their intrinsic characteristics. The complementary absorptivity of these two dyes also enables the fabrication of ‘full-spectrum’ solar cells.

In bulk-heterojunction solar cells, besides many important parameters (such as the broad spectral overlap with solar irradiation spectrum, good processabilty, and matched energy level), the morphology control by the application of self-organizable material is considered to be an effective method to realize high efficiencies. Hence, two series of materials, triangle-shaped discotic graphene molecules with swallow-tailed alkyl substituents and a self-organizable conjugated polymer containing unsubstituted benzodithiophene moiety, have been studied.

1) For the BHJ cells based on triangle-shaped discotic graphene molecules with swallow-tailed alkyl substituents (benzo[o]bistriphenyleno[2,1,12,11-efghi:2´,1´,12´, 11´-uvabc] ovalene, **3**), the factor of self-organization ability has a profound influence on the supramolecular organization and consequently the photovoltaic performance.

After the thermal treatment, the supramolecular order in the molecule **3b** with longer branched side chains was improved, while the molecule **3a** with shorter substituents showed no annealing effect, which resulted in the corresponding higher EQE of 19% at 490 nm for the longer branched molecule **3b**. Hence, the higher device efficiency of graphene molecule **3b** with longer alkyl chains is attributed to the improved intracolumnar packing in the molecule upon annealing favoring the charge-carrier transport. This differs from the previous observation that the device efficiency decreased with increasing length of the alkyl substituents in the HBCs,[1] which again emphasizes the vital impact of molecules' self-organization ability on the local order and photovoltaic performance.

2) Extending this attention into the conjugated polymers for BHJs, for the first time, a substituent-free benzodithiophene based copolymer was used as p-type semiconductor for solar cell applications. The free volume for the two side chains (dodecyl) on the thiophene units is the advantage of using unsubstituted benzodithiophene moiety, which strengthens the π-π stacking between polymer backbones and results in high order in the molecule. The strong self-organization ability of this PBTT polymer was used to optimize the heterojunction solar-cell morphology, since there was a significant effect of thermal annealing on film aggregation. Upon stepwise post-annealing process, the BHJ cells fabricated from PBTT/[70]PCBM gave a promising power-conversion efficiency of 2.7%. The comparison of PBTT with P3HT in aspects of molecule structure and photovoltaic performance showed that an efficient solar cell depends on many factors, each of which should be considered thoroughly during the molecule design, synthesis and device fabrication. Further modification of using more ribbon structure in a D-A copolymer **SCS312** did not lead to higher efficiency. It has to be noted that, for the future work, the experience obtained from the failure is as precious as that concluded in a successful system.

For solid-state DSSCs, metal-free sensitizers with high molar absorption coefficients and good photochemical stability are desirable. Besides the possession of these merits, the two investigated sensitizers, a perylene sensitizer **ID176** and an isophorone dye **Ind-1,** have a complementary absorption, which makes it possible to build a molecular cocktail solar cell which can cover the whole region of visible light spectrum.

The perylene sensitizer **ID176,** with an absorption maximum of 566nm on the dye-grafted TiO_2 film, exhibited an efficiency of 2.2% as comparable as that of **N3**-sensitized cells under the same condition. The spectral sensitization of the cells could be adjusted by using different solvents, which is considered to be an efficient approach for broadening the spectral response of certain sensitizer. The noticeable device stability of **ID176**-based cells for 1220 h provides a step into reliable solar cells.

The isophorone dye **Ind-1,** with λ_{max} of 447 nm on the semiconductor surface, exhibited a relatively high efficiency of 1.9% in solid-state DSSCs.

The comprehension of the intrinsic characteristics of separate dyes and their behaviours in the devices will be helpful for the fabrication of the ‘full-spectrum’ solar cells.

7.2 Outlook

Ideally, a comprehensive understanding of all factors influencing cell efficiency will lead to the achievement of highly efficient solar cells. To explore highly efficient organic thin-film photovoltaics, the research should be carried out in several aspects: design of new materials, comprehension of operation mechanism in different systems, and cell architecture adjustment.

The pursuing of new promising materials still plays a key role in realizing high power conversion efficiencies. With the experience obtained from this study, during the design of new polymer materials for BHJ cells, all the requirements of ideal donors must be considered and special attention should be paid to the aspect of self-organization ability. For metal-free sensitizers in solid-state DSSCs, the direction of extending light absorption, enhancing molar absorptivity and photochemical stability will be considered to be a right way for high conversion efficiency.

Besides the searching for new promising materials, the modification of cell architecture is also considered to be of high priority.

Based on the gained experience from the materials investigated in this study and the understanding of operation mechanism in the corresponding system, the following modification on the cell layout can be done.

7.2.1 Hybrid Tandem Solar Cell

Based on the knowledge of solid-state DSSCs and BHJs, a hybrid tandem solar cell, the combination of an organic sensitizer with absorption in the range of relatively shorter wavelength and a low bandgap polymer with broader absorption, is believed to be capable of harvesting more light (Figure 1). It should be noted that such kind of hybrid tandem cells has not been reported in literature.

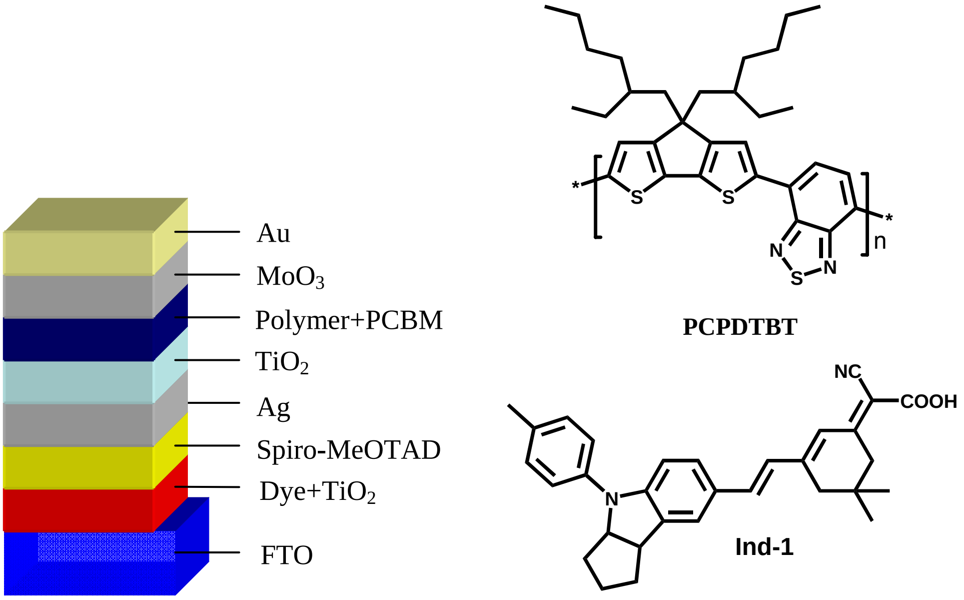

Figure 1. Hybrid tandem solar cells construction (left); structure of polymer PCPDTBT (middle); structure of dye **Ind-1** (right).

The organic sensitizer **Ind-1** (Chapter 5) possesses an absorption spectrum mainly in the blue region of the visible light. And the initial testing on the solid-state dye-sensitized solar cell device exhibited over 1.9% of power conversion efficiency. It is thus worthy to try the tandem cells with another material whose absorption is in the red region or the near infrared region.

Thus, a low bandgap polymer, for instance, PCPDTBT (Chapter 2) which has very strong absorption in the near infrared region, can be applied in this tandem cell architecture.

7.3 References

[1] J. Li, M. Kastler, W. Pisula, J. W. F. Fobertson, D. Wasserfallen, A. C. Grimsdale, J. Wu, K. Müllen, *Adv. Funct. Mater.* **2007**, *17*, 2528.

List of Publications

[1] **M. Liu**, R. Rieger, C. Li, H. Menges, M. Kastler, M. Baumgarten, K. Müllen, *ChemSusChem*, **2010**, *3*, 106.

[2] X. Feng, **M. Liu**, W. Pisula, M.Takase, J. Li, K. Müllen, *Adv. Mater.* **2008**, *20,* 2684.

[3] M. Yin, Y. Cheng, **M. Liu**, J. S. Gutmann, K. Müllen, *Angew. Chem. Int. Ed.* 2**008**, *47*, 8400.

[4] C. Li, **M. Liu**, N. G. Pschirer, M. Baumgarten, K. Müllen, *Chem. Rev.* accepted.

[5] Q. Wang, D. Qu, J. Ren, L. Xu, **M. Liu**, H. Tian, *Dyes and Pigments*, **2003**, *59*, 163.